

100-13000-1  
FEB 13 1980  
NAS126/3238

NASA Contractor Report 3238

COMPLETED  
ORIGINAL

# Application of Numerical Optimization to the Design of Wings With Specified Pressure Distributions

H. P. Haney and R. R. Johnson

CONTRACT NAS2-9653  
FEBRUARY 1980

NASA

101

NASA Contractor Report 3238

# Application of Numerical Optimization to the Design of Wings With Specified Pressure Distributions

H. P. Haney and R. R. Johnson  
*Vought Corporation*  
*Dallas, Texas*

Prepared for  
Ames Research Center  
under Contract NAS2-9653



**Scientific and Technical  
Information Office**

1980

APPLICATION OF NUMERICAL OPTIMIZATION TO THE  
DESIGN OF WINGS WITH SPECIFIED PRESSURE DISTRIBUTIONS

H. P. Haney and R. R. Johnson  
Vought Corporation

SUMMARY

A practical procedure for the optimum design of transonic wings is demonstrated. The procedure uses an optimization program based on the method of feasible directions coupled with an aerodynamic analysis program which solves the three-dimensional potential equation for subsonic through transonic flow. Two new wings for the A-7 aircraft were designed by using the optimization procedure to achieve specified surface pressure distributions. The new wings, along with the existing A-7 wing, were tested in the Ames 11-ft. transonic wind tunnel. The experimental data show that all of the performance goals were met. However, comparisons of the wind tunnel results with the theoretical predictions indicate some differences at conditions for which strong shock waves occur.

INTRODUCTION

The aerodynamic design of wings for transonic flight has in the past been accomplished by increasing wing sweep and decreasing maximum thickness which often compromises subsonic performance. Dr. Whitcomb at NASA Langley Research Center demonstrated that wing surface contours can be tailored to improve transonic and subsonic performance. These designs were accomplished by experimental methods which are extremely costly and time consuming. Reliable analysis methods for predicting transonic flow fields have recently been developed. Mr. R. M. Hicks at NASA Ames Research Center combined transonic flow analyses

with an optimization procedure to design efficient airfoils (reference 1) and isolated, three-dimensional wings (reference 2). The present study extends the three-dimensional procedure to the design of wings with optimum pressure distributions. This report describes an application of this transonic wing design procedure to two wing designs and the wind tunnel test of the optimized wings.

#### ANALYTICAL DESIGN METHOD

##### Airfoil Optimization

Prior to the availability of a finite wing optimization code, transonic airfoil sections were optimized and evaluated for use as wing sections in the three-dimensional wing. That procedure and the results are summarized here in order to demonstrate an application of numerical optimization to a simpler two-dimensional problem and to describe the geometric shape functions and design variables which were subsequently used for the three-dimensional wing optimization. In addition, the procedure shows the results of adding a passive boundary layer displacement thickness to the airfoil coordinates - an approximation which was also used in the finite wing design study.

A schematic flow chart of the numerical optimization design program is shown in figure 1. An iterative solution of the full potential equation for two-dimensional transonic flow (reference 3) was used for the aerodynamic analysis program. A baseline airfoil is required to start each design problem. The airfoil shape is represented in the program by the following equation:

$$Y = Y_{\text{basic}} + \sum_i a_i F_i$$

where  $Y_{\text{basic}}$  is the set of ordinates of the baseline airfoil and  $F_i$  are the shape functions. The shape functions are added linearly to the baseline profile by the optimization program (reference 4) to achieve the desired design improvement. The contribution of each function is determined by the value of the coefficient,  $a_i$ , associated with that function. The  $a_i$  coefficients are therefore the design variables. Other inputs to the program include Mach number, angle of attack, and any constraints to be imposed on the design.

The hypothetical design problem represented by the flow chart is drag minimization at one Mach number,  $M_1$ , with drag constrained to some specified value at another Mach number,  $M_2$ . The optimization program changes the design variables, one by one, and returns to the aerodynamics program for evaluation of the drag coefficient at both Mach numbers  $M_1$  and  $M_2$  after each change. The partial derivatives of drag with respect to each design variable form the gradient of drag,  $\nabla C_d$ . The initial direction in which the design variables are changed to reduce the drag coefficient at  $M_1$  is  $-\nabla C_d$  (the steepest descent direction) if the drag constraint at  $M_2$  is not active. The optimization program then increments the design variables in this direction until the drag starts to increase or the drag constraint at Mach number  $M_2$  is encountered. If either of these possibilities occurs, new gradients are calculated and a new direction is found that will decrease drag without violating the constraint. When a minimum value of drag for Mach number  $M_1$  is attained with a satisfied drag constraint at  $M_2$ , the required optimized airfoil has been achieved.

Supercritical airfoil design by numerical optimization is facilitated by using a set of geometric shape functions, each of which affects a different limited region of the profile. General classes of such functions which have been used successfully to optimize supercritical airfoils are described in reference 1. The shape functions that were used in the present study were selected from those general functions and were applied to the airfoil upper surface only. The exponential decay function and the sine functions are presented in figure 2. The exponential decay function,  $F_1$ , provided variations in curvature near the airfoil leading edge. In the sine functions, the exponents on the chordwise coordinate,  $x$ , were assigned so that the maximum perturbations of  $F_2$ ,  $F_3$ ,  $F_4$  and  $F_5$  were at 20, 40, 60, and 80 percent of the chord respectively. The width of the region affected by each sine function was controlled by the localization exponent, 3. Previous studies (ref. 1 and 2) have found that these shape functions provide a broad range of smooth airfoil contour modifications during the optimization process.

The value of considering off-design performance of an airfoil during the design process will be illustrated by comparing the results of a single design point optimization with a double design-point optimization. The first involves recontouring the upper surface of an existing supercritical airfoil to reduce the wave drag at a single design Mach number. The second consists

of recontouring the upper surface of the same airfoil to reduce the wave drag at the design Mach number subject to a drag constraint at a lower Mach number.

The calculated wave drag for Mach numbers near drag divergence for the starting airfoil and the two optimized airfoils is presented in figure 3. All these data are for 0.40  $C_L$ , the design lift coefficient of the starting airfoil. Mach number 0.78 was arbitrarily selected as the primary design point, i.e., the Mach number at which the drag would be minimized. Results of the single design point optimization are indicated as 412M1. The drag at Mach number 0.78 is significantly less than that of the starting airfoil, and as a result, the drag rise occurs at a higher Mach number. However, the drag at lower Mach numbers, 0.76 and 0.77, is greater than that of the starting airfoil. This local region of drag-creep could limit the usefulness of the improved drag rise Mach number of the optimized airfoil.

In order to avoid the drag-creep problem, the airfoil was optimized a second time with an upper bound of 0.0005 imposed on the drag coefficient at Mach number 0.77. Results of this double design-point optimization are indicated in figure 3 as 412M2. The drag rise for this airfoil occurs at a slightly lower Mach number than it does for 412M1, but there is no drag-creep over the range of Mach numbers for which the airfoils were analyzed. Therefore, airfoil 412M2 is the more desirable design. The geometric modification is shown in figure 4. The change is primarily a reduction in surface curvature from 5 percent to 40 percent of the chord.

The aerodynamics code that was used in the optimization program is an inviscid, potential flow analysis method. In order to account for first order viscous effects in the flow field solution, a boundary layer displacement thickness was added to the starting profile before the optimization process. The displacement thickness was calculated for the pressure distribution of the starting airfoil at a Mach number near its design condition, 0.78. It remained unchanged throughout the optimization process, and each of the optimized airfoils included this same passive displacement thickness. Therefore, the analytical characteristics of the airfoils did not reflect potential changes in boundary layer behavior due to changes in the chordwise pressure distributions.

Another aerodynamic analysis code (ref. 5) was used to evaluate the active boundary layer characteristics of the starting airfoil and optimized airfoil

412M2. That computer program is also based on an iterative solution of the full potential equation for transonic flow, and it includes a momentum-integral calculation of the turbulent boundary layer parameters. During the solution, the airfoil geometry is regularly updated by adding a boundary layer displacement thickness. The results of the viscous analyses with that code for Mach numbers between 0.76 and 0.81 indicated that the differences in boundary layer characteristics would be small. The calculated wave drag for the starting airfoil and airfoil 412M2 is presented in figure 5. The relative increase in the drag rise Mach number is in good agreement with the results of the inviscid code (figure 3). It was concluded that the inviscid code, supplemented by a passive displacement thickness, is adequate for airfoil optimization.

Models of the starting airfoil and airfoil 412M2 were tested in the NASA Ames Two-by-Two-Foot Wind Tunnel. The experimental data from that test agree very well with the analytical predictions.

#### Wing Optimization Procedure

The Jameson potential flow analysis code as described in reference 6 was selected as the aerodynamics program for the wing design procedure. It solves the three-dimensional potential equation for subsonic through transonic flow with exact boundary conditions. Therefore, it is capable of treating thick wings with blunt leading edges - the type of wings which were required to meet the performance goals of this study.

In the wing design procedure, the Jameson 3-D code, FL022, was used for the aerodynamic analysis program within the optimization design code as described in reference 2. It is based on an iterative solution of the full potential equation for three-dimensional transonic flow. Viscous effects are not modeled in the program. A two-dimensional boundary layer displacement thickness was added to the sections which were used to define the starting wing geometry. It was calculated for a representative pressure distribution of the starting wing and remained unchanged throughout the optimization process. The displacement thickness was subtracted from the final wing geometry.

Twist, trailing edge camber, and twenty-two surface shape functions at each of five semispan stations were used as the design variables. The trailing edge camber variable was represented as a nonlinear meanline displacement function for control of the aft loading. It was of the form  $\Delta y/c = (x/c)^8$ . The surface shape functions were of the same form as those used for the 2-D airfoil optimization and were applied to the upper surface and lower surface at each defining station. The exponents on  $(x/c)$  in the sine function expressions were assigned so that the maximum perturbations were at 5, 10, 20, 30, 40, 50, 60, 70, 80 and 90 percent of the chord. Two exponential decay functions provided variations in curvature near the leading edge. These particular shape functions were selected because of previous success in optimizing two-dimensional sections with functions of the same type.

During a preliminary series of wing optimization runs, drag coefficient was selected as the parameter to be minimized. The runs were effective in reducing drag, but adverse pressure gradients which existed in the velocity distributions on the starting wing still remained after the optimization runs. The gradients were quite large and would have caused premature boundary layer separation. To achieve wing geometries with pressure gradients weak enough to avoid separation, desired pressure distributions were specified over the entire chord and substituted for drag coefficient as the design goal. Specifically, the square of the difference between the existing pressure distribution and a desired pressure distribution was integrated over the entire chord and specified as the parameter to be minimized, figure 6.

## WING DESIGN APPLICATIONS

### Design Goals

Rigorous problems were selected to exercise the wing optimization code. Two new wings were designed for the A-7 which demonstrate how transonic computational design methods can improve overall aircraft performance. The design goal for the first wing was to increase the A-7 wing thickness by 71 percent while maintaining the same drag divergence Mach number. The design goal for the second wing was to reduce the induced drag by 25 percent and to increase the wing thickness by 28 percent while maintaining the same drag divergence Mach number. Preliminary analytical studies with the Jameson 3-D program indicated that if section properties could be optimized successfully, design goals for the first wing, wing No. 1, could be achieved with the same planform as the existing A-7 wing: aspect ratio 4, 35° quarter-chord sweep. The starting streamwise sections were defined by a 12 percent thick, supercritical airfoil which, when adjusted for planform effects with simple sweep theory, had a design lift coefficient consistent with the performance objectives of the first wing. That 12-percent thick airfoil was the same as the starting airfoil which was evaluated during the airfoil optimization study.

An aspect ratio of five was selected for wing No. 2 based on aircraft performance studies. The Jameson program indicated that an optimized wing which was 28 percent thicker than the A-7 wing could have as little as 20 degrees of quarter-chord sweep without changing the drag divergence Mach number. The starting streamwise sections were defined by a 9 percent thick supercritical airfoil which had a design lift coefficient consistent with the performance objectives of the second wing. A sketch of the planforms of the existing A-7 wing, supercritical wing No. 1, and supercritical wing No. 2 is presented in figure 7.

### Application of Procedure

The shapes of the desired pressure distributions were patterned after two-dimensional, supercritical airfoil distributions which are known to avoid premature boundary layer separation over a wide range of flight conditions.

The pressure levels at each defining section were tailored to the thickness-to-chord ratio and design lift coefficient of each wing. An upper surface maximum local Mach number of 1.17 was specified to be the same at all defining stations except for the centerline station, where the maximum Mach number was reduced a small increment to alleviate the expected adverse wing-body interference effects. Thus, straight isobars over most of the upper surface were a design objective. The lower surface levels were varied at each defining station to force the spanwise loading distribution to be elliptical, and thereby to achieve minimum induced drag. Overall, the optimization objective for these transonic wings was to restore the efficient, supercritical airfoil pressure distributions which had been changed by the three-dimensional effects.

Since optimization of the entire wing in one computer run would have been impractical because of the large number of design variables, wing sections at each of the defining stations were optimized sequentially from root to tip, first on the upper surface, then on the lower surface. For the first wing, a single pass across the wing produced chordwise and spanwise loading distributions which were sufficiently close to the desired loadings to achieve the aerodynamic performance goals. The relatively high sweep of the wing, 35 degrees at the quarter-chord, prevented velocity distribution changes at the outboard sections from disturbing the previously optimized inboard section velocity distributions. For the second wing, which has only 20 degrees sweep at the quarter-chord, optimizations at the outboard sections did affect the previously optimized inboard sections. As a result, a second optimization pass across that wing was necessary. For both wings, it was found that when all the design variables at a given section were active, the optimization progressed slowly. Computer runs with only twist and trailing edge camber as the active variables produced good results. In addition, selection of a limited number of surface shape functions based on a comparison of desired versus starting pressures effectively expedited the optimization and reduced costs. A comparison of typical starting, desired, and optimized chordwise pressure distributions is presented in figure 8.

#### Design Results

The starting and final wing geometry and pressures for wing No. 2 are presented in figure 9. At the wing centerline, figure 9(a), the optimization

code has produced a section with its maximum thickness at 20 percent of the chord. The maximum thickness of the starting section was at 38 percent. The aft camber has been removed and the section has been twisted significantly. The resulting chordwise pressure distribution has most of the desirable features of an efficient supercritical airfoil: (1) supersonic flow begins near the leading edge on the upper surface, providing a significant lift contribution from the forward portion of the wing; (2) moderate supersonic flow is maintained to approximately the midchord, where it is decelerated through a weak shock; and (3) lift is generated by aft camber, but without excessively adverse pressure gradients. It is interesting to note that the analytically optimized geometry is similar to root section designs produced by extensive transonic wind tunnel testing. As expected, less optimization was required at midspan stations where the flow is more nearly two-dimensional, figure 9(b). Although the pressure distribution at the tip was significantly improved through contouring and washout, further improvement is needed, figure 9(c). The optimization changes to wing No. 1 were similar to those for wing No. 2.

Predicted drag characteristics of the two optimized wings are compared with the isolated A-7 wing in figure 10. These data indicated that the drag divergence Mach number of the optimized wings would be nearly the same as that of the A-7 wing. And, since drag divergence for the A-7 is dominantly wing-induced, it was anticipated that a wind tunnel test of the A-7 wing-fuselage configuration would confirm these analytical drag divergence predictions. The unrealistically high drag level for wing No. 1 may be related to (1) the unconservative finite difference algorithm in the computer code and (2) to the high velocity potential residual resulting from the limited number of iterations allowed by the computer budget. Fortunately, however, the optimization procedure developed for the present study relies only on pressure distribution predictions which are known to converge well before convergence of the drag coefficient. Furthermore, the wing designer should always be cautious when using drag as an objective function in an optimization problem.

#### WIND TUNNEL TEST

Models of the two optimized wings were tested in the NASA Ames 11-foot transonic wind tunnel during July, 1978. The existing A-7 wing was also tested to provide baseline data for comparison. The primary purpose of the test was

to determine the transonic longitudinal characteristics of the baseline wing and the two optimized wings.

#### Model Description

The DTNSRDC 0.1 scale A-7 flow-through model was modified to accept models of the two optimized wings. Three 48-port scanivalves were placed in the fuselage nose, and a wing root bending moment gage was added to the existing A-7 force wing model. Both optimized wing models have 120 static pressure taps distributed along four spanwise stations of the left wing and wing root bending moment strain gages. No leading or trailing edge devices were built into the two pressure wings.

The optimized wing model contours were machined to closely simulate the mathematical representation used in the aerodynamic analysis code. Linear surface elements connect the optimized airfoil sections along lines of constant  $x/c$ . The theoretical wing center section is actually submerged within the fuselage. This deviation of the wind tunnel model from the optimized isolated wing was most noticeable on wing No. 2, which had a significant twist change near the centerline. Photographs of the wing-fuselage configurations are presented in figure 11.

#### Test Procedure

Pitch polars were run with each of the three wing models on the A-7 fuselage at Mach numbers of 0.4, 0.6, 0.7, 0.8, 0.85, 0.88 and 0.9 for  $6 \times 10^6$  Reynolds number and Mach numbers of 0.7, 0.8, 0.85, 0.88, and 0.9 for  $8 \times 10^6$  Reynolds number. Additional data points were taken near 0.4 and 0.6  $C_L$  at Mach numbers of 0.75, 0.82, 0.84, 0.86, 0.87 and 0.89 for  $8 \times 10^6$  Reynolds number to accurately define drag divergence Mach number. Oil flow studies were made of the two optimized wings. Photographs of the upper and lower surfaces of the left wing were taken at Mach numbers of 0.6, 0.8, 0.85 and 0.88 at ten angles-of-attack.

Six component balance data and wing root bending moment buffet data were taken for each wing at all data points. Pitching moment was referenced to 30 percent of the A-7 mean geometric chord. Pressure data were also taken for the two optimized wings except during oil flow studies. Grounding between

the balance sting and model at high  $C_L$ 's and dynamic pressures limited the test angle-of-attack.

### Forces and Moments

Aerodynamic forces and moments for the A-7 wing configuration are compared with those for wing No. 1 in figure 12. At Mach 0.4, figure 12(a), wing No. 1 shows a greater maximum lift coefficient than the A-7 wing, 1.06 as compared to 1.01. The drag coefficients for wing No. 1 are significantly less than those for the A-7 wing at lift coefficients above 0.4. The drag reduction is more than 700 counts at  $C_L = 0.9$ . These improvements in low speed characteristics are the result of better pressure distributions which exist on the optimized wing. Two reasons for the better pressure distributions are traceable to the geometric features of the wing. First, the nose radius is larger than that of the A-7 wing. This results in lower velocities near the leading edge and a smaller recovery pressure rise. Thus, the boundary layer remains attached at the higher lift coefficients. Secondly, wing No. 1 has some camber aft of the midchord, the A-7 wing does not. Consequently, significant lift is produced by the aft portion of the wing, thereby reducing the contributions required from regions near the leading edge. As a result, leading edge vortex formation and stall occur at higher lift coefficients. The differences in pitching moment over the entire range of lift coefficients are also caused by the aft loading on the optimized wing.

Wing No. 1 also has lower drag coefficients at Mach 0.6, 0.7, 0.8 and 0.85, figures 12(b), 12(c), 12(d) and 12(e) respectively. At Mach numbers greater than 0.85, the drag of both wing configurations begins to increase sharply. At Mach numbers above the drag divergence, figures 12(f) and 12(g), drag coefficients for wing No. 1 equal or exceed those of the A-7 wing for much of the drag polar. A crossplot of the drag coefficients at constant lift coefficients of 0.4 and 0.6 is presented in figure 14. These data indicate that the drag divergence Mach number of wing No. 1 is the same as the drag divergence Mach number of the A-7 wing configuration. Therefore, the primary design goal for wing No. 1 has been achieved.

Figures 12(a), (b) and (d) indicate that the secondary design goals have also been met or exceeded. Those goals are that the drag of the new wings

shall be no greater than the drag of the existing A-7 wing at conditions of loiter (Mach = 0.3,  $C_L = .47$ ), maneuver (Mach = 0.6,  $C_L = .70$ ), and cruise (Mach = 0.8,  $C_L = .40$ ).

Aerodynamic forces and moments for the A-7 wing configuration are compared with those for wing No. 2 in figure 13. At Mach 0.4, figure 13(a), wing No. 2 has considerably less drag at lift coefficients up to 0.90. The drag improvement at low speed is the result of several geometric features of the new wing. First, the larger leading edge radius and the aft camber provide pressure distribution improvements similar to those which improved the aerodynamic characteristics of wing No. 1. Second, the greater aspect ratio of wing No. 2, AR = 5 as compared to AR = 4 for the A-7 wing, directly reduces the lift-induced drag. Third, the lower sweep of wing No. 2,  $20^\circ$  at the quarter-chord as compared to  $35^\circ$  for the A-7 wing, inhibits the formation of a leading edge vortex and the drag increase associated with it. The aft camber of this wing is also responsible for the more negative (nose down) pitching moment.

The maximum lift coefficient of wing No. 2 at Mach 0.4 is approximately 0.93. This is somewhat less than had been expected. Inspection of the leading edge of the wing has indicated a significant deviation of the actual geometry from the theoretical design contour. The deviation is such that a local region of high curvature exists on the upper surface near the leading edge for much of the span of both sides of the wing. This geometric deviation is probably responsible for the premature stall.

The drag improvements for wing No. 2 at higher Mach numbers are similar to those at Mach 0.4. Aerodynamic parameters for Mach 0.6, 0.7, 0.8 and 0.85 are presented in figures 13(b), 13(c), 13(d) and 13(e) respectively. At Mach numbers greater than 0.85, the drag of both wing configurations begins to increase rapidly. At Mach numbers above drag divergence, figures 13(f) and 13(g), the drag coefficients for wing No. 2 equal or exceed those for the A-7 wing except at lift coefficients above 0.7. A crossplot of the drag at constant lift coefficients of 0.4 and 0.6 for this wing is also presented in figure 14. These data show that the drag divergence Mach number of wing No. 2 is approximately the same as that of the A-7 wing. Therefore, the primary design goal for wing No. 2 has been achieved. Figures 13(a), (b) and (d) indicate that the secondary design goals have been met or exceeded.

Lift-to-drag ratios for the three wing configurations are presented in

figure 15. At Mach numbers less than drag divergence, 0.4, 0.6, 0.7, and 0.8, both of the optimized wings have substantially higher L/D than the A-7 wing, except for wing No. 2 at lift coefficients above 0.9. At Mach 0.85, values of L/D for the optimized wings are greater than those for the A-7 wing, but the amount of improvement is somewhat less than at the lower Mach numbers. At Mach numbers above drag divergence, 0.88 and 0.90, the aerodynamic efficiency of the new wings is less than that of the A-7 for much of the  $C_L$  range. That characteristic is typical of thicker wings, since they are more sensitive to shock-induced separation at Mach numbers above drag rise.

#### Wing Pressure Distributions and Oil Flow Patterns

Upper surface pressure distributions for wing No. 1 at Mach 0.60 are presented in figure 16. The data indicate that the boundary layer remains attached at lift coefficients as high as 0.67, figure 16(c). The reason for such good boundary layer behavior at moderately high angles of attack is the relatively low maximum velocity near the leading edge -- a direct result of the blunt leading edge and the aft camber of this wing. At a higher angle of attack, figure 16(d), the negative pressure coefficients near the trailing edge indicate that much of the wing is stalled. And, near maximum lift, the flow is separated over most of the wing, figure 16(e). These observations are consistent with the results of oil flow studies which were conducted on this wing.

Upper surface pressure distributions for wing No. 1 at Mach 0.85 are presented in figure 17. These data show that at low and moderately high angles of attack, figures 17(a), (b) and (c), the shock strength remains weak and the boundary layer remains attached, even though the lift is being generated by large regions of locally supersonic flow on the upper surface. It is this desirable feature that distinguishes this optimized transonic wing from conventional high speed wings. At higher angles of attack, figures 17(d) and (e), the shock strength increases and moves forward -- an indication of trailing edge stall and the consequent loss of circulation. At the highest angle of attack at which this wing was tested, figure 17(h), most of the wing upper surface is stalled. Photographs of oil flow patterns on the upper surface of wing No. 1 are presented in figure 18. The Mach number and angles of attack are approximately the same as for the pressure data in figure 17. At low and

moderate angles of attack, figures 18(a), (b) and (c), the oil patterns show the location of the shock wave, and they indicate that the flow is attached over the entire upper surface. At a higher angle of attack, figure 18(d), the first indication of shock-induced separation is observed. Figures 18(e) through 18(g) show the formation of large regions of separated flow, which correspond with the behavior of the pressure distributions at these angles of attack, figure 17(e) through 17(g).

Upper surface pressure distributions for wing No. 2 at Mach numbers 0.60 are presented in figure 19. At low and moderate angles of attack, figures 18(a), (b) and (c), the data indicate that low maximum velocities near the leading edge and the consequent mild pressure gradients have allowed the boundary layer to remain attached. However, at a higher angle of attack, figure 19(d), a significant decrease in velocities near the leading edge occurs at semispan stations outboard of 0.13 ETA. This premature loss of suction indicates a large region of separated flow on the upper surface, and it is followed by an unexpectedly low maximum lift coefficient. This leading edge separation is probably caused by the model geometry errors near the leading edge discussed earlier.

Upper surface pressure distributions for wing No. 2 at Mach 0.85 are presented in figure 20. At low and moderate angles of attack, these data show the same desirable supercritical features as were observed in the pressure distributions of wing No. 1. Therefore, it appears that the geometric error near the leading edge has not significantly affected the locally supersonic flow field at the moderate angles of attack. However, the effects of the geometric error at higher angles of attack are not easy to identify. Further investigation of this problem has been planned. Photographs of oil flow patterns on the upper surface of wing No. 2 are presented in figure 21. The Mach number and angles of attack are approximately the same as for the pressure data in figure 20. At low and moderate angles of attack, figures 21(a) and (b), the oil flow patterns indicate that the boundary layer is attached over the entire upper surface. At higher angles of attack, figure 21(c) through 21(f), shock induced separation and the development of large stall cells are observed.

## COMPARISON OF THEORY AND EXPERIMENT

Theoretical pressure distributions are compared with experimental data at Mach 0.599 for wing No. 1 in figure 22 and for wing No. 2 in figure 23. The angles of attack for the theoretical calculations are the same as the wing angles of attack at which wind tunnel data were obtained. The comparisons are generally good with the exception of regions on the upper surface near the trailing edge. The deviations are the greatest at the inboard stations, figures 22(a) and 23(a). This trend suggests that the deviations are the result of flow field interference from the fuselage -- an effect which is not modeled by the theoretical code.

Theory and experiment are compared at Mach 0.85 for wing No. 1 in figure 24 and for wing No. 2 in figure 25. The angles of attack for the theoretical calculations are the same as the wing angles of attack at which wind tunnel data were obtained. The comparisons are unexpectedly poor. In addition to the apparent fuselage interference effects on the pressures at the inboard stations, the strength and location of the upper surface shock is clearly not predicted well by the theory. Generally, the experimental shock waves were stronger than predicted by the theory. However, since a conservative maximum Mach number (1.17) had been specified during the optimization process, the experimental shocks were not strong enough to affect the performance of the wings. Three possible reasons for this poor comparison are as follows: (1) the effective free stream Mach number in the wind tunnel is higher than that obtained by tunnel empty calibrations, (2) the absence of a fuselage in the theoretical code is affecting the local Mach numbers along the entire span, and (3) the nonconservative modeling of the shock structure which is used in the theory is not adequately capturing the shock wave. A study to investigate all the factors which might contribute to these discrepancies is being planned.

An example of the incremental Mach number which is required to get better agreement is shown in figure 26. The experimental data for Mach 0.799 is compared to theory for Mach 0.851. Except for apparent fuselage interference on the inboard stations, the agreement is very good. Therefore, an effective Mach number delta of approximately 0.05 is necessary to neutralize the combination of errors which are causing the differences between theory and experiment.

## CONCLUSIONS

A numerical optimization procedure for transonic wing design has been demonstrated. Two new wings for the A-7 aircraft were designed by using the optimization procedure to achieve specified surface pressure distributions. Wind tunnel test data showed that all of the design goals were met or exceeded. The following conclusions are emphasized:

1. An aerodynamic design procedure consisting of Jameson's three-dimensional transonic flow analysis code and a numerical optimization algorithm is a powerful tool for transonic wing design.
2. Comparisons of theoretical pressure distributions with the experimental data show good agreement except at conditions for which strong shock waves occur. Possible reasons for the poor comparisons are (1) the nonconservative shock modeling which is used in the theory, (2) the absence of a fuselage in the theory, and (3) wind tunnel calibration anomalies.
3. The technique of designing to specified pressure distributions is an effective way to control the shock wave strength and location, and to avoid premature boundary layer separation. This method is particularly important when the aerodynamic analysis code does not simulate viscous effects. Furthermore, it proved to be a successful approach, even though some of the inviscid flow field was not accurately predicted.

## REFERENCES

1. Hicks, R. M., Vanderplaats, G. N.: "Application of Numerical Optimization to the Design of Supercritical Airfoils without Drag-Creep," SAE Paper 770440, 1977.
2. Hicks, R. M., and Henne, P. A., "Wing Design by Numerical Optimization," AIAA Paper No. 77-1247, 1977.
3. Jameson, A.: "Iterative Solution of Transonic Flows over Airfoils and Wings Including Flows at Mach 1," Comm. Pure Appl. Math, Vol. 27, pp. 283-309, 1974.
4. Vanderplaats, G. N.: "CONMIN-A Fortran Program for Constrained Function Minimization, User's Manual," NASA TMX-62,282, August 1973.
5. Bauer, F., Garabedian, P., Korn, D., Jameson, A.: "Supercritical Wing Sections II. Lecture Notes in Economics and Mathematical Systems," Vol. 108, Springer-Verlag, 1975.
6. Jameson, A., Caughey, D. A., Newman, P. A., and Davis, R. M., "A Brief Description of the Jameson-Caughey NYU Transonic Swept-Wing Computer Program--FL022," NASA TMX-73,996, December 1976.

DRAG MINIMIZATION AT  $M_1$  WITH DRAG CONSTRAINT AT  $M_2$

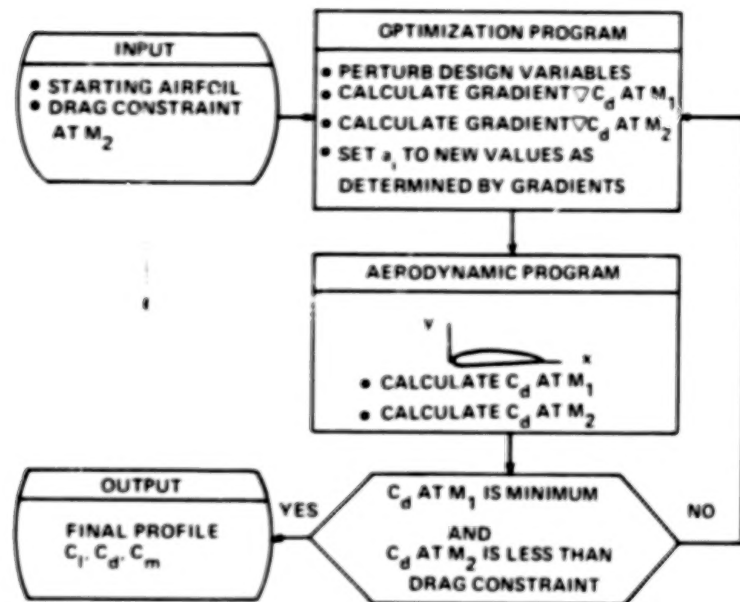


**FIGURE 1. FLOW CHART OF NUMERICAL OPTIMIZATION DESIGN PROGRAM**

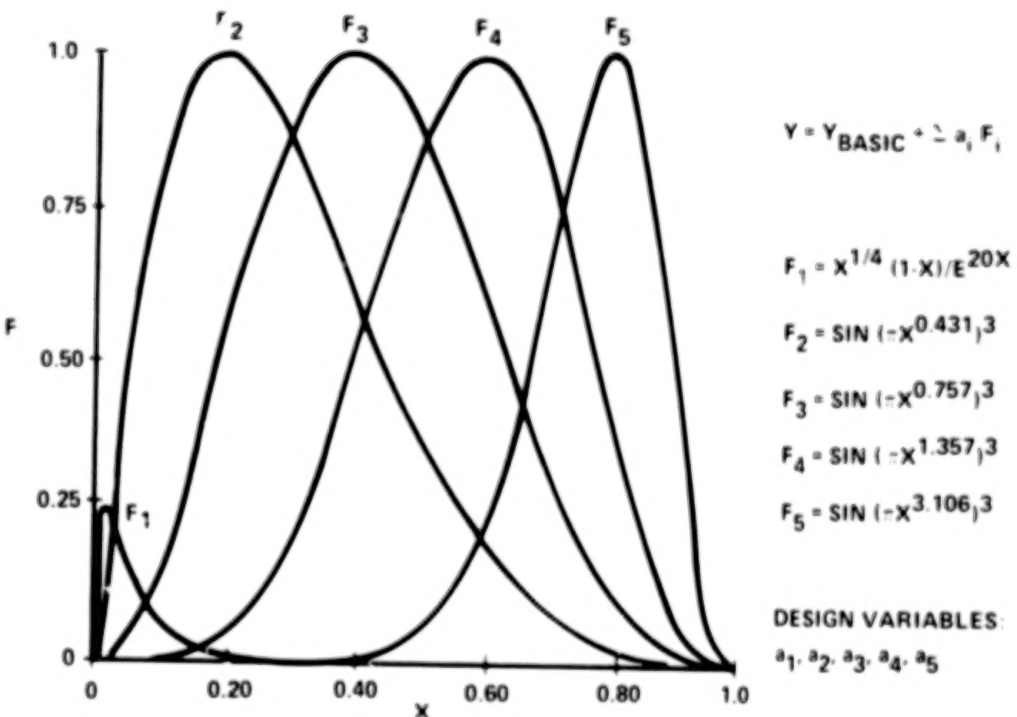


**FIGURE 2. AIRFOIL SHAPE FUNCTIONS**

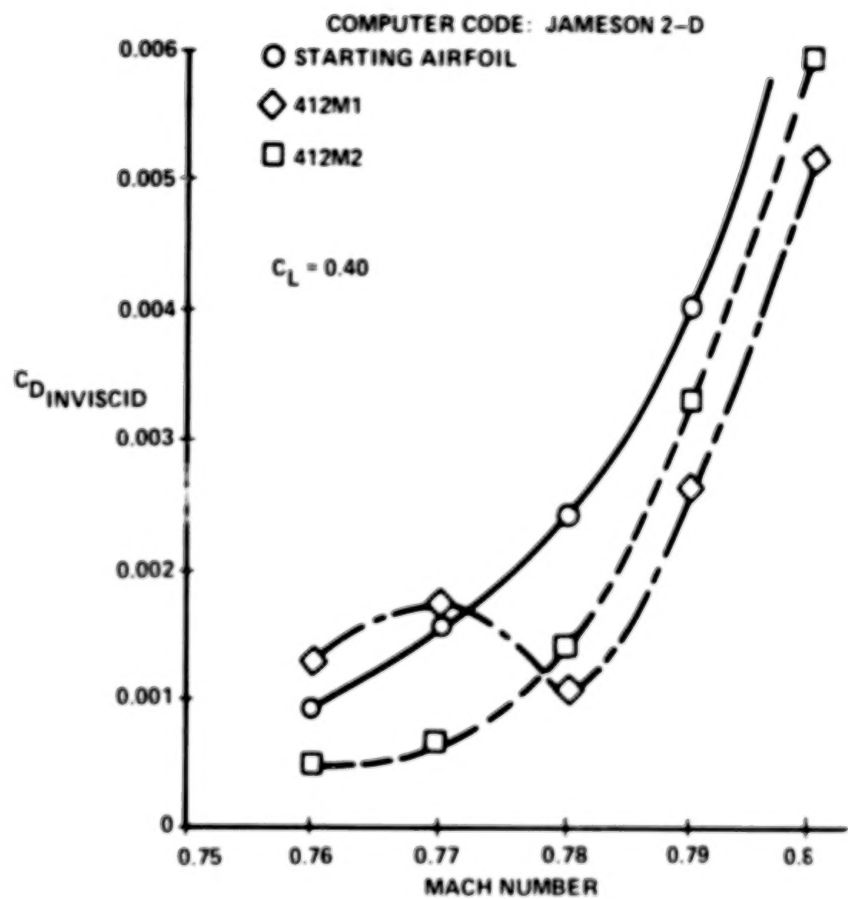


FIGURE 3. AIRFOIL SECTION OPTIMIZATION

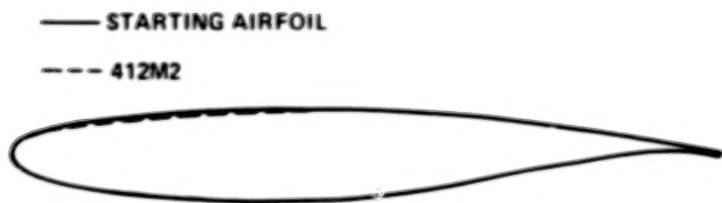


FIGURE 4. AIRFOIL GEOMETRY COMPARISON

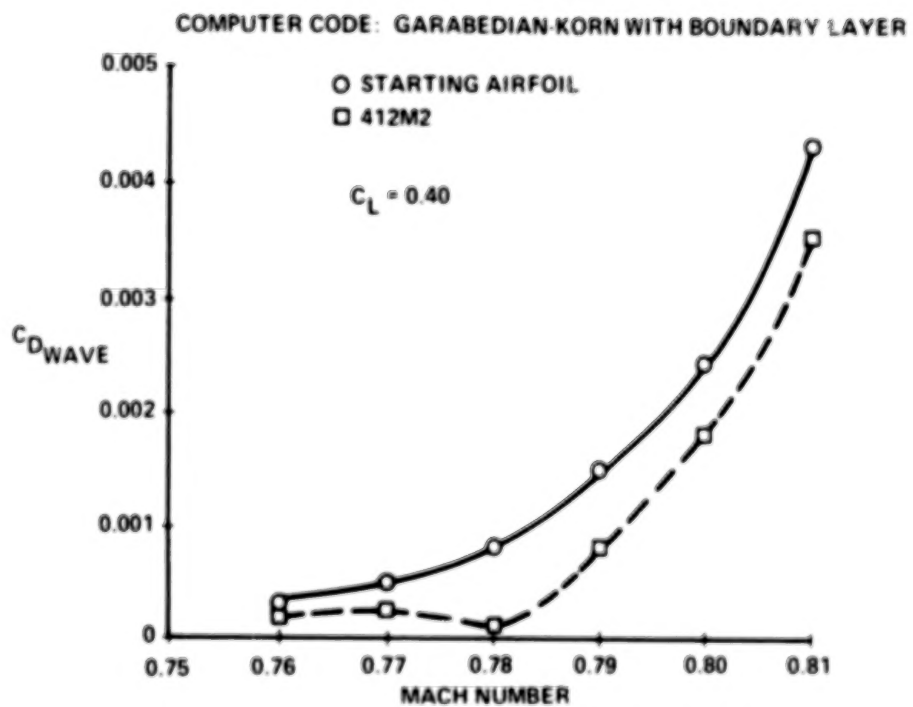


FIGURE 5. COMPARISON OF WAVE DRAG CHARACTERISTICS FOR THE STARTING AIRFOIL AND OPTIMIZED AIRFOIL 412M2

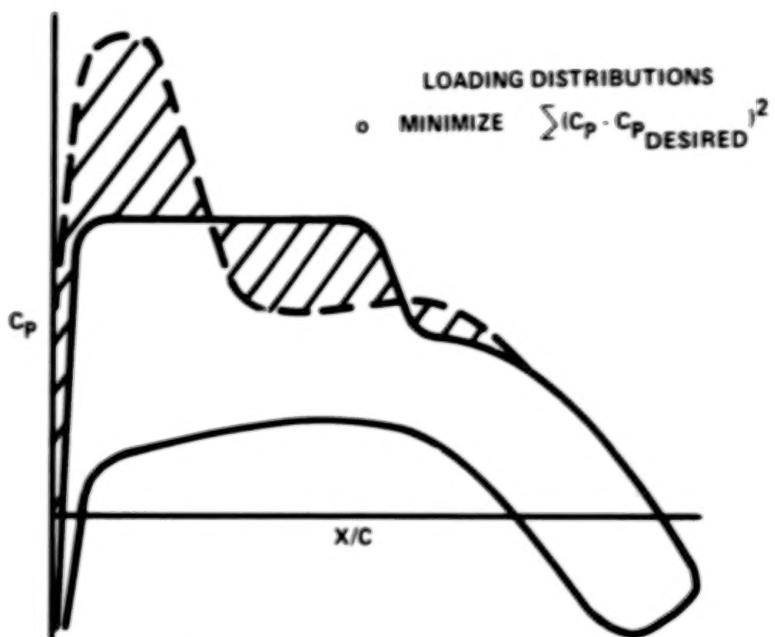
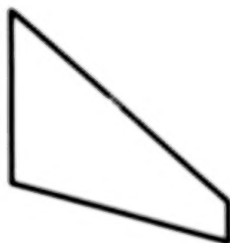


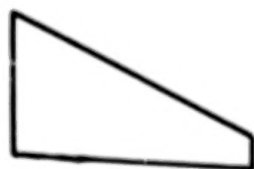
FIGURE 6. USE OF OPTIMIZATION CODE FOR WING DESIGN



A-7 WING  
AR = 4  
SWEEP =  $35^{\circ}$   
T/C = .07



WING NO. 1  
AR = 4  
SWEEP =  $35^{\circ}$   
T/C = .12



WING NO. 2  
AR = 5  
SWEEP =  $20^{\circ}$   
T/C = .09

FIGURE 7. PLANVIEWS OF THE EXISTING A-7 WING AND THE TWO OPTIMIZED WINGS

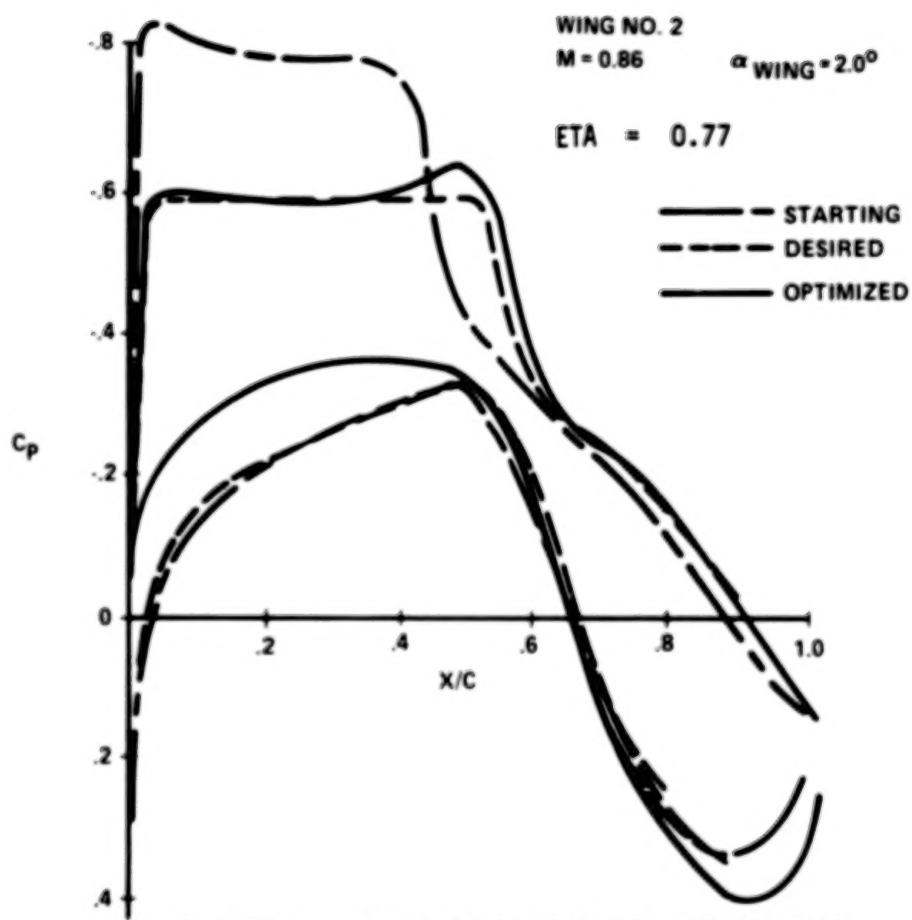
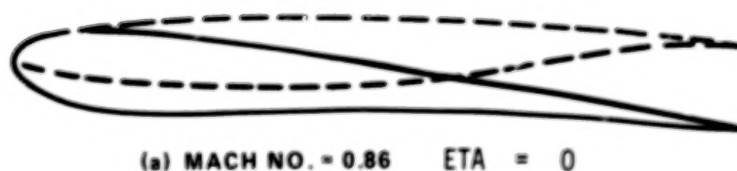
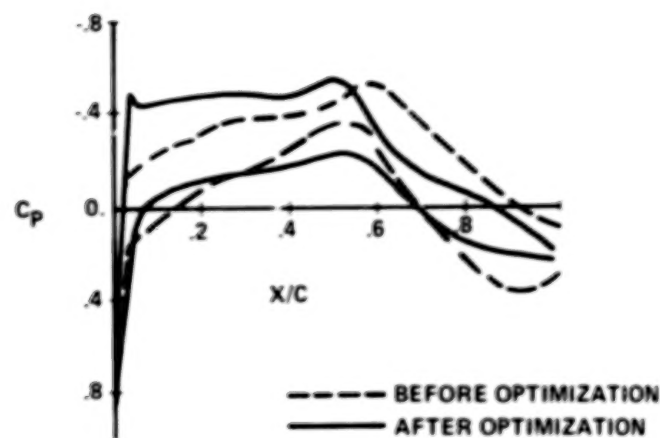
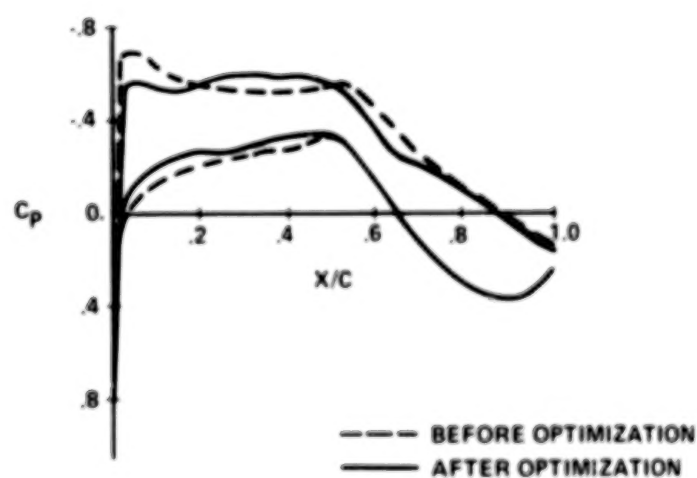


FIGURE 8. EXAMPLE OF PRESSURE DISTRIBUTION  
OPTIMIZATION



(a) MACH NO. = 0.86      ETA = 0

FIGURE 9. WING NO. 2 STARTING AND OPTIMIZED GEOMETRY AND PRESSURES



(b) MACH NO. = 0.86      ETA = 0.39

FIGURE 9. WING NO. 2 STARTING AND OPTIMIZED GEOMETRY AND PRESSURES

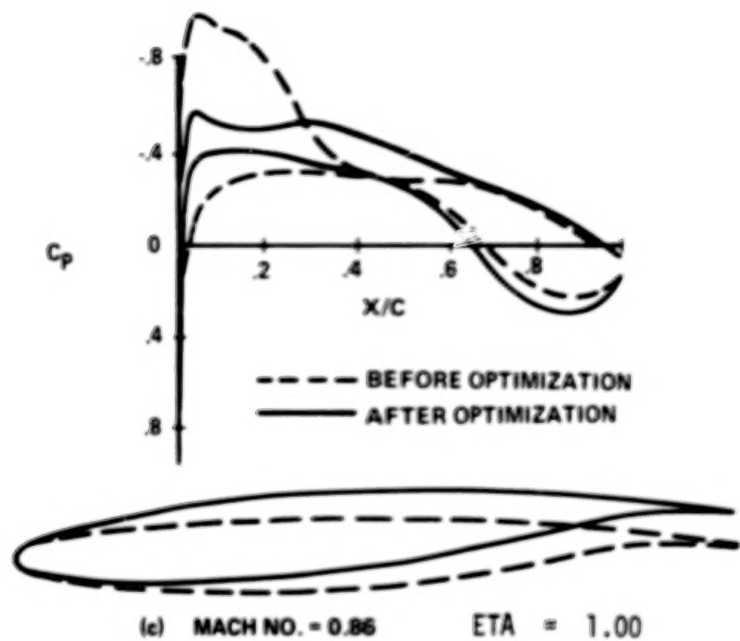


FIGURE 9. WING NO. 2 STARTING AND OPTIMIZED GEOMETRY AND PRESSURES

COMPARISON OF TRANSONIC DRAG RISE

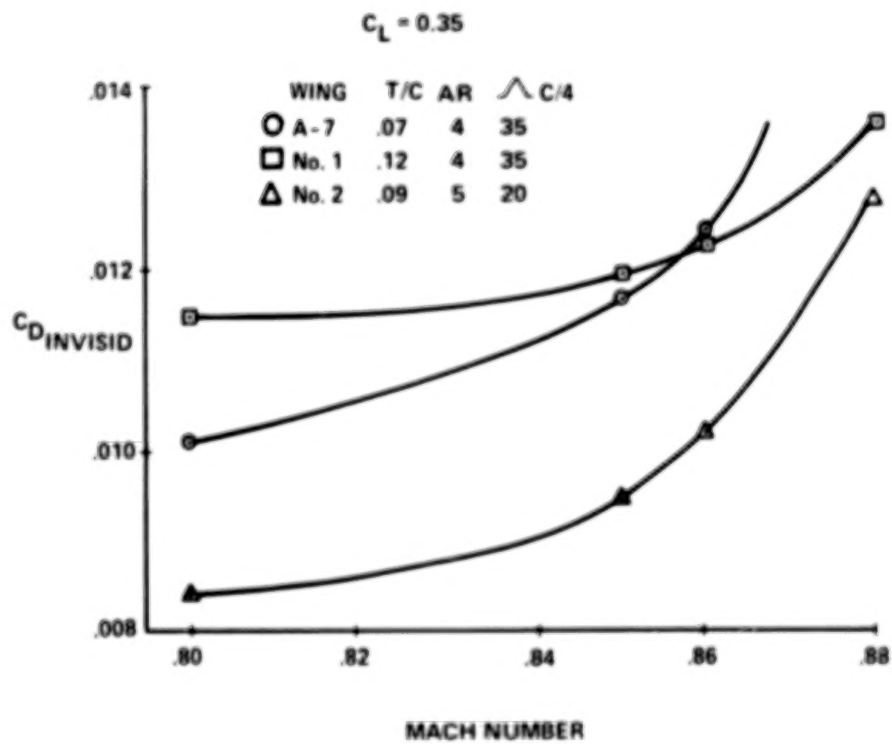
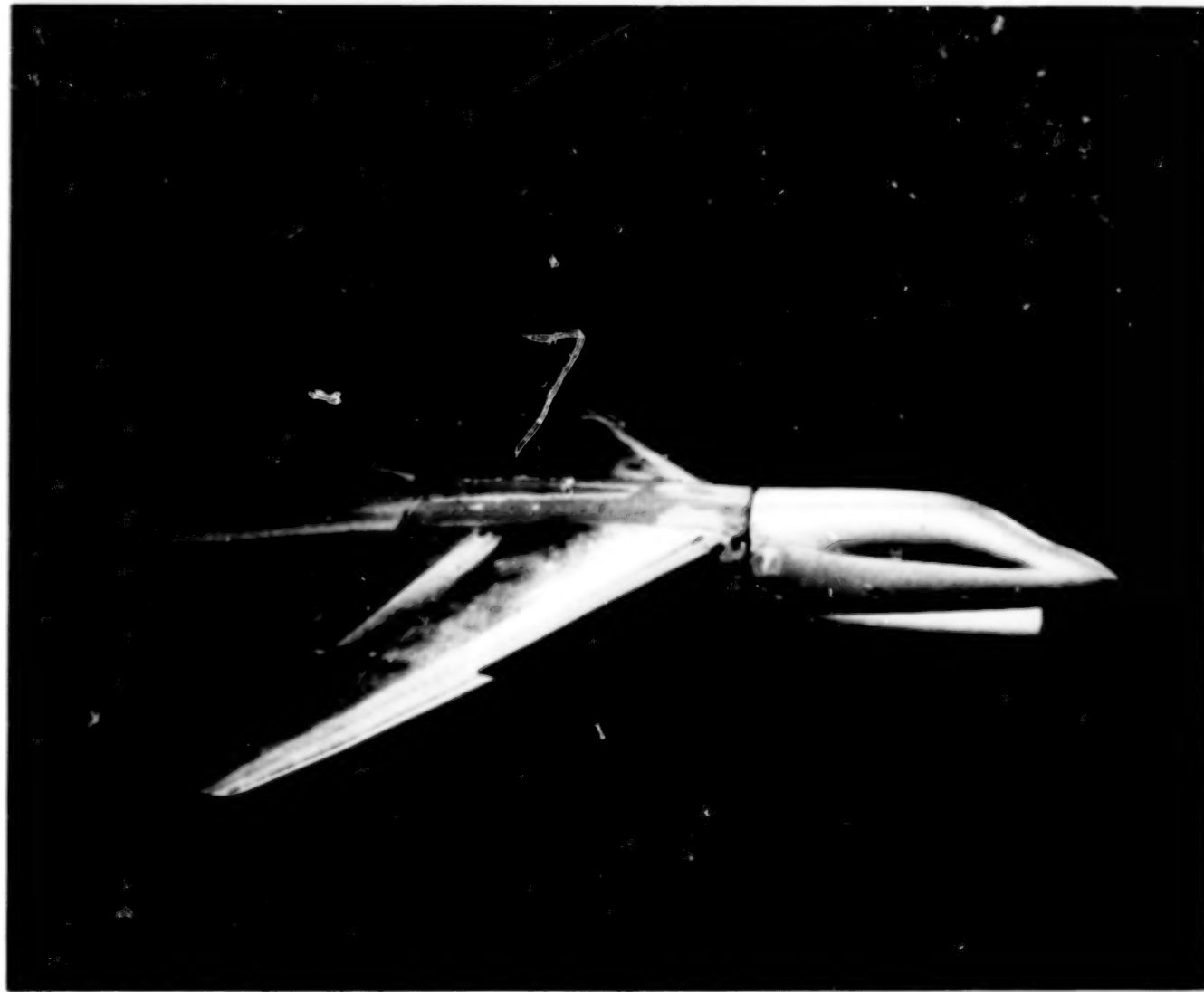
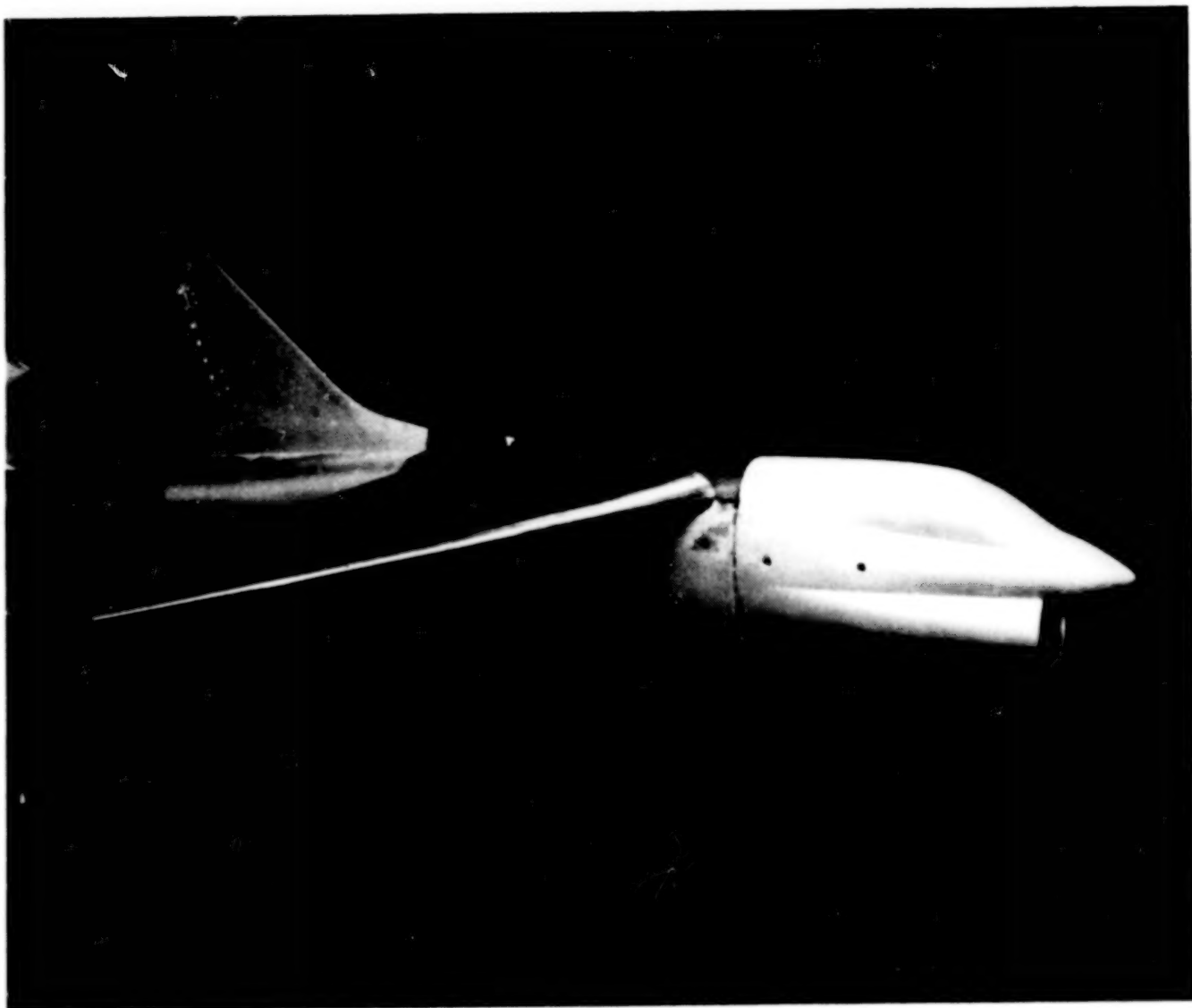


FIGURE 10. ANALYTICAL DRAG CHARACTERISTICS



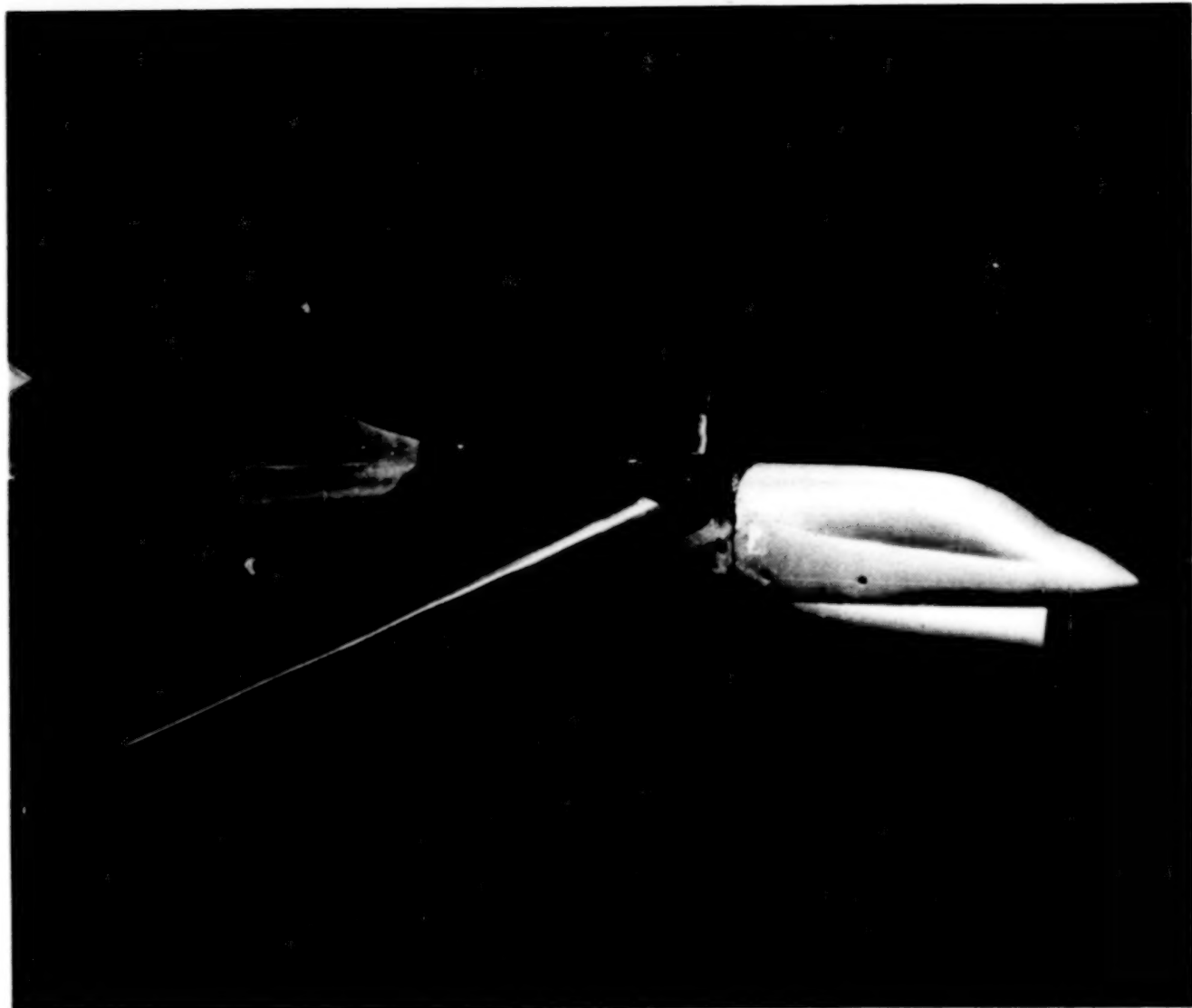
(a) A-7 Wing

Figure 11. - One-tenth scale wind tunnel model.



(b) Wing No. 1

Figure 11. - One-tenth scale wind tunnel model.

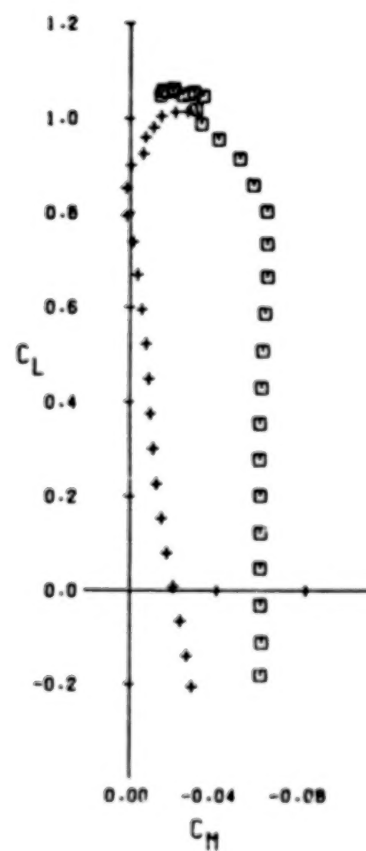
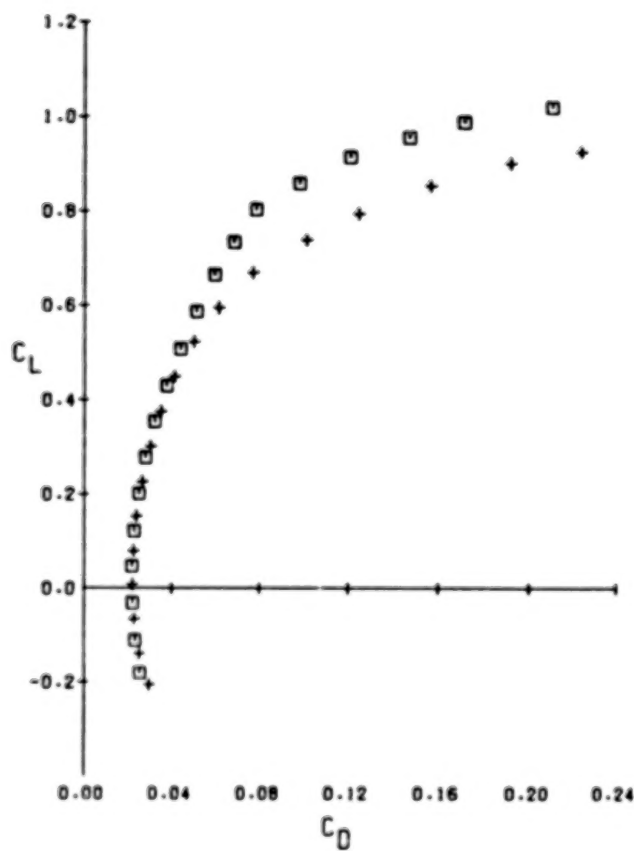
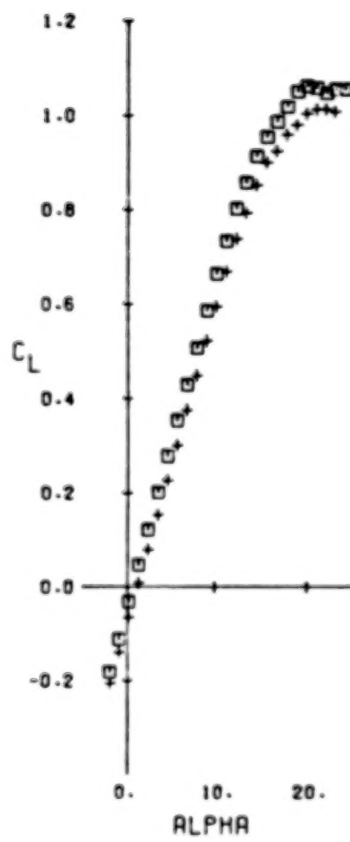


(c) Wing No. 2

Figure 11. - One-tenth scale wind tunnel model.

NASA AMES WIND TUNNEL TEST 231-1-11  
 A-7 TRANSONIC WING DESIGNS

SYM RUN CONF MACH RN/FT  
 + 11B A-7 0.40 5.04 MILLION  
 □ 202 NO.1 0.40 5.21 MILLION



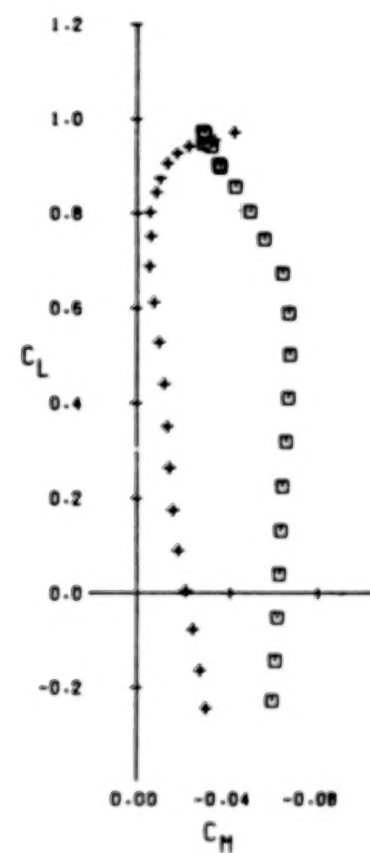
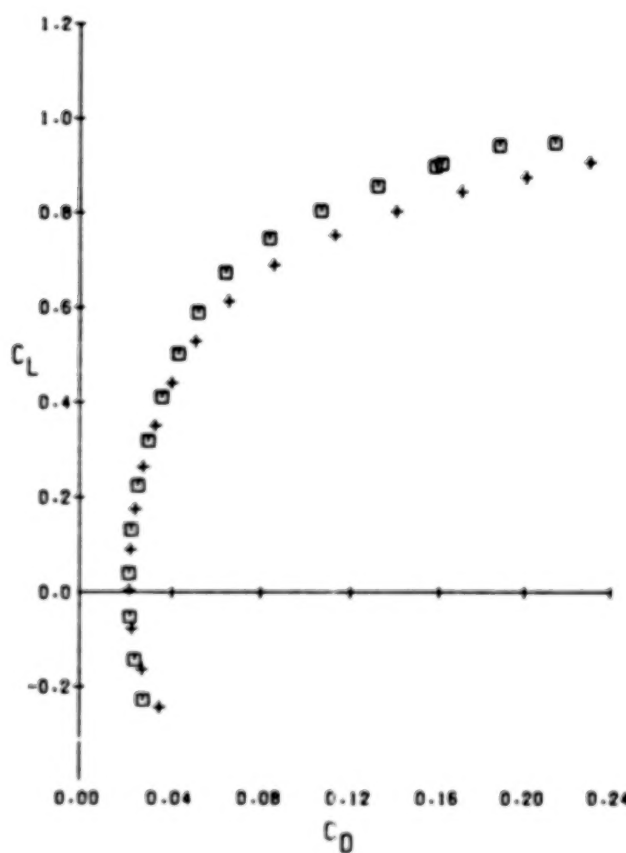
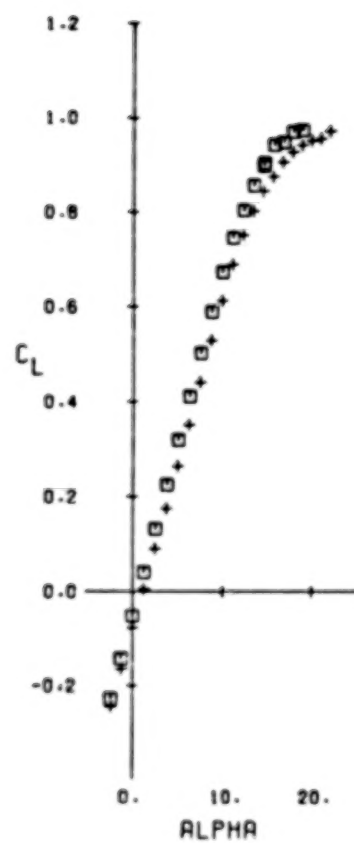
(A) MACH = 0.40

FIGURE 12.- COMPARISON OF AERODYNAMIC PARAMETERS FOR THE A-7 AND WING NO. 1

NASA AMES WIND TUNNEL TEST 231-1-11

A-7 TRANSONIC WING DESIGNS

SYM RUN CONF	MACH	RN/FT	
+ 119	A-7	0.60	5.98 MILLION
□ 203	NO.1	0.60	6.02 MILLION

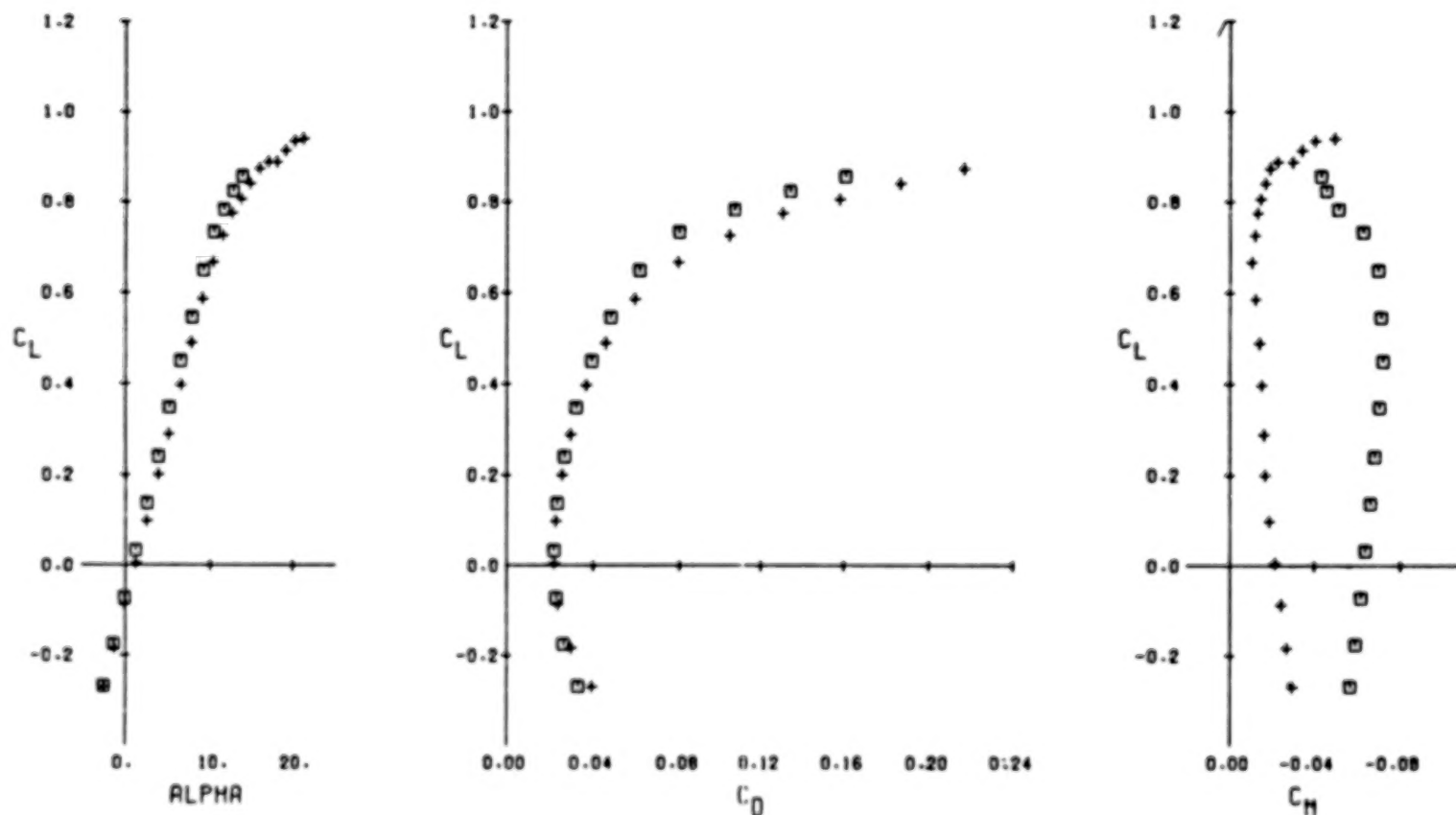


(B) MACH = 0.60

FIGURE 12.- COMPARISON OF AERODYNAMIC PARAMETERS FOR THE A-7 AND WING NO. 1

NASA AMES WIND TUNNEL TEST 231-1-11  
 A-7 TRANSONIC WING DESIGNS

SYM RUN CONF MACH .RN/FT  
 + 120 A-7 0.70 6.03 MILLION  
 □ 204 NO.1 0.70 5.99 MILLION

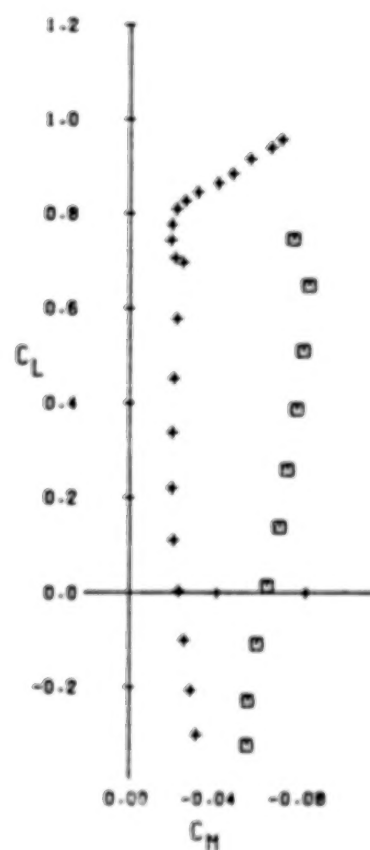
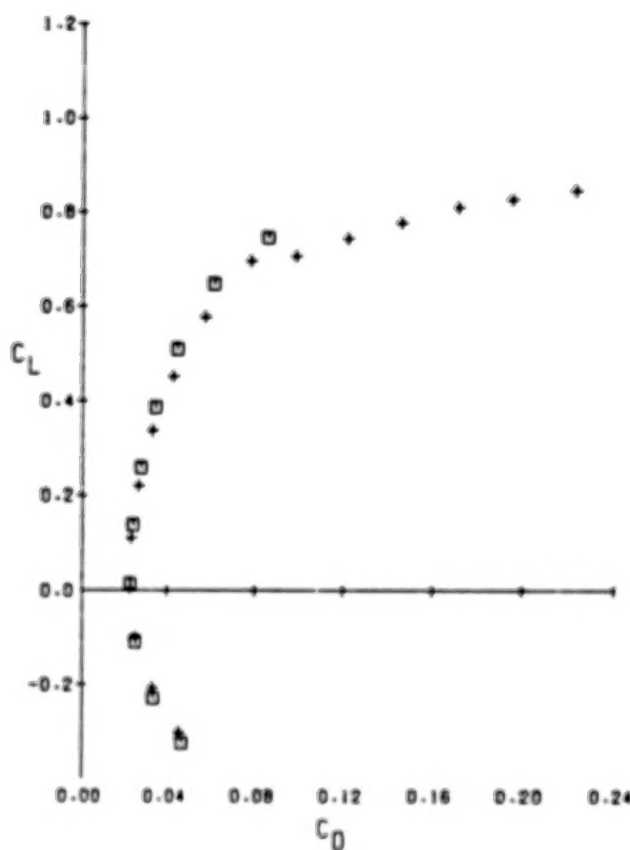
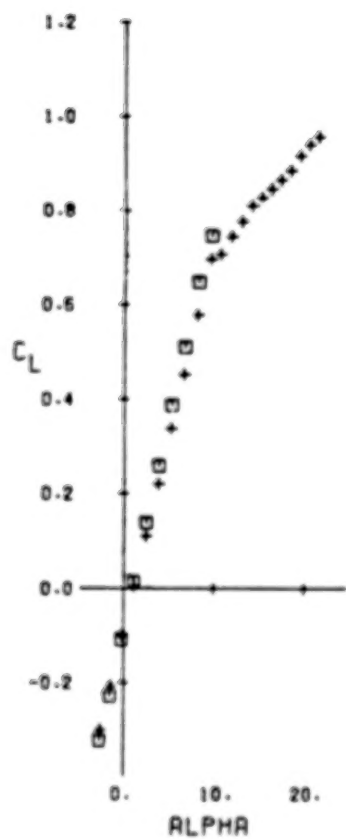


(C) MACH = 0.70

FIGURE 12.- COMPARISON OF AERODYNAMIC PARAMETERS FOR THE A-7 AND WING NO. 1

NASA AMES WIND TUNNEL TEST 231-1-11  
 A-7 TRANSONIC WING DESIGNS

SYM RUN CONF MACH RN/FT  
 + 121 A-7 0.80 5.99 MILLION  
 □ 205 NO.1 0.80 6.00 MILLION



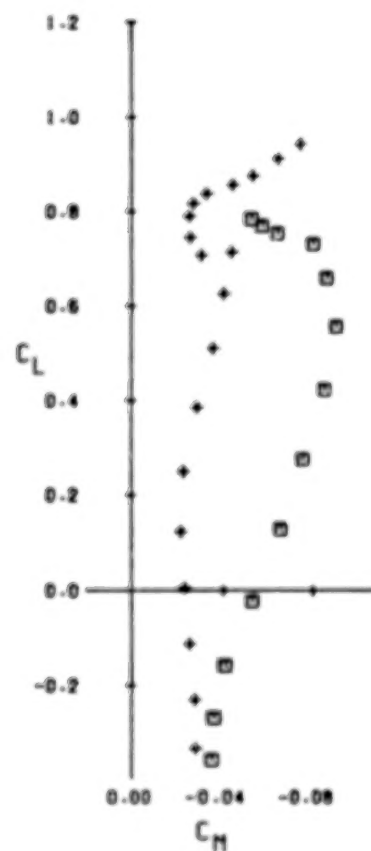
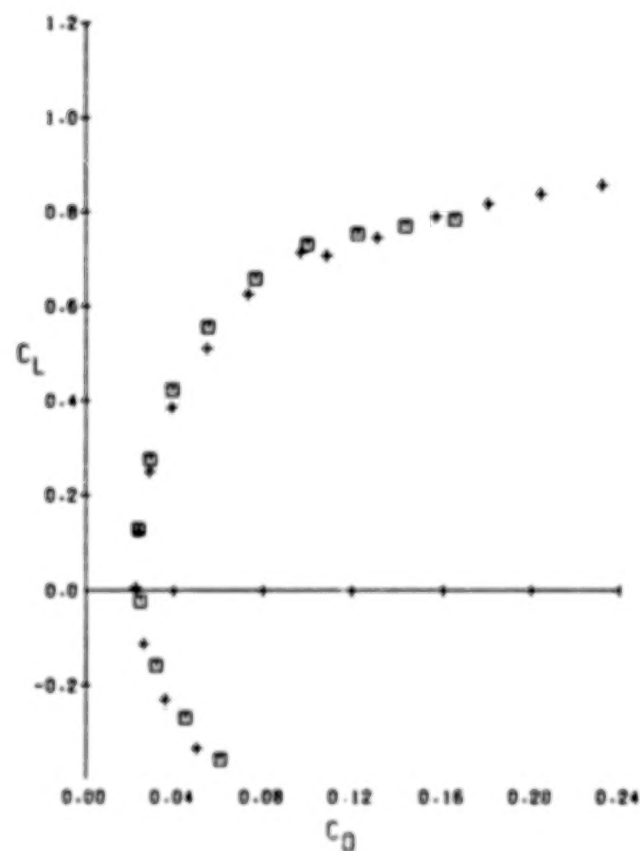
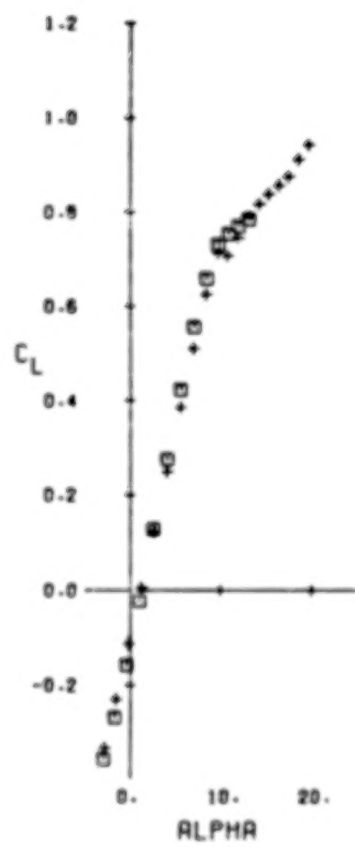
(D) MACH = 0.80

FIGURE 12.- COMPARISON OF AERODYNAMIC PARAMETERS FOR THE A-7 AND WING NO. 1

## NASA AMES WIND TUNNEL TEST 231-1-11

## A-7 TRANSONIC WING DESIGNS

SYM RUN CONF MACH RHO/FT  
 + 122 A-7 0.85 5.98 MILLION  
 □ 206 NO.1 0.85 6.02 MILLION



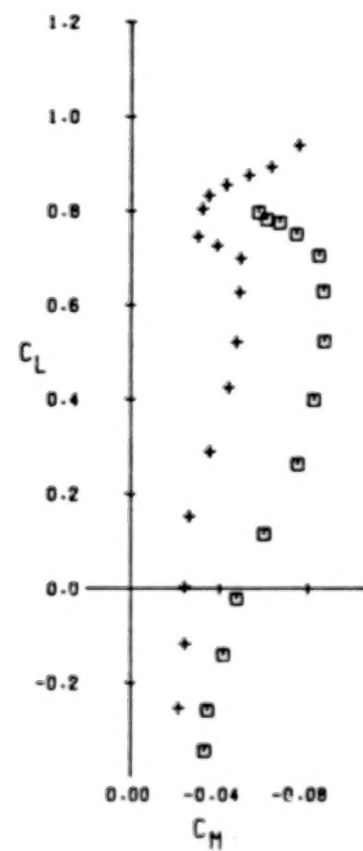
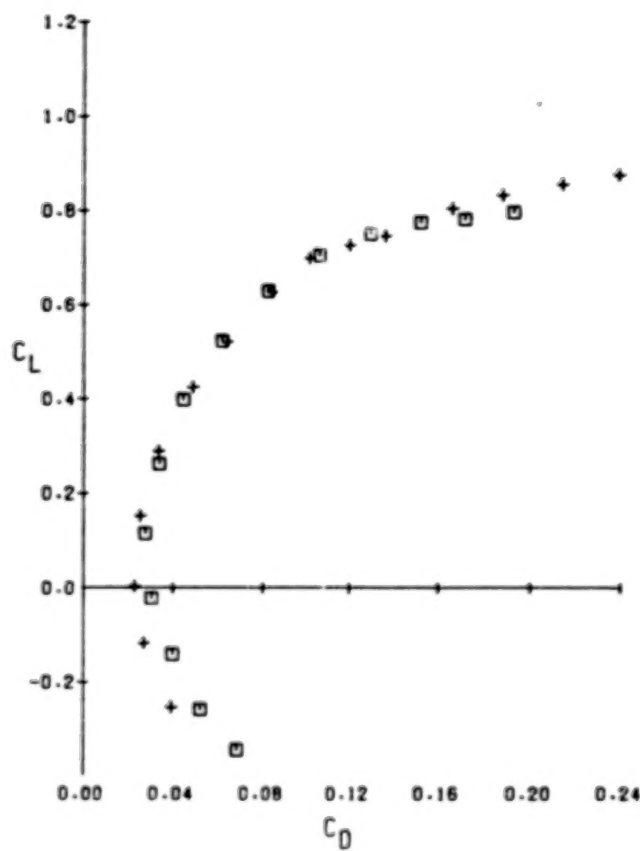
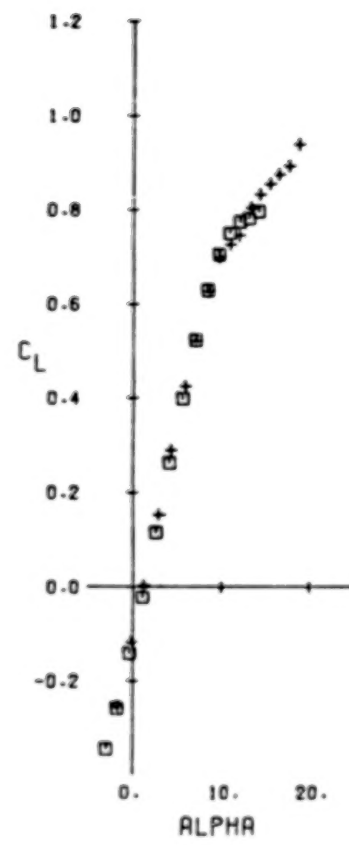
(E) MACH = 0.85

FIGURE 12.- COMPARISON OF AERODYNAMIC PARAMETERS FOR THE A-7 AND WING NO. 1

NASA JAMES WIND TUNNEL TEST 231-1-T1

A-7 TRANSONIC WING DESIGNS

SYM RUN CONF MACH \_\_\_\_RN/FT  
 + 130 A-7 0.88 5.98 MILLION  
 □ 207 NO.1 0.88 5.99 MILLION



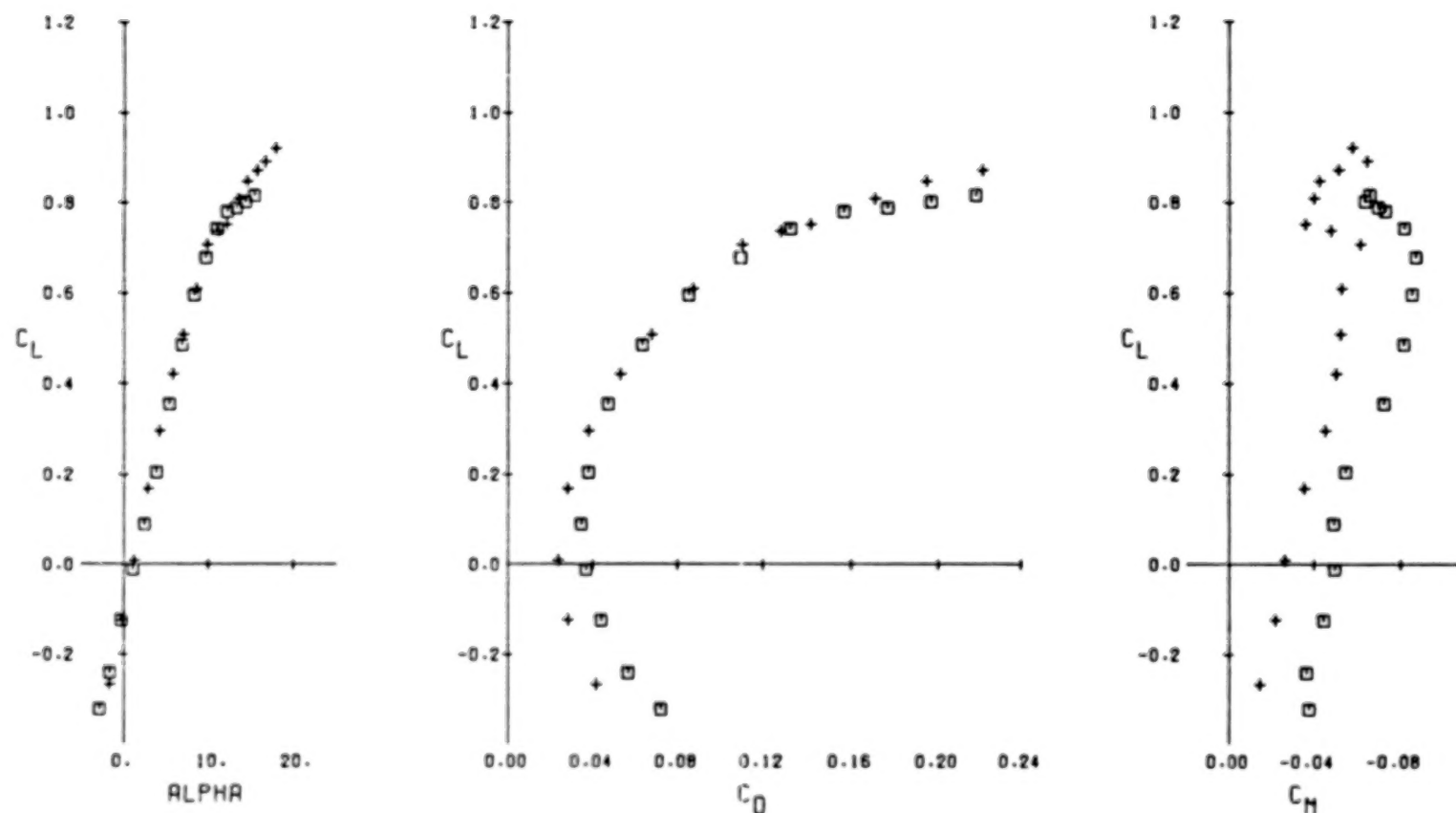
(F) MACH = 0.88

FIGURE 12-- COMPARISON OF AERODYNAMIC PARAMETERS FOR THE A-7 AND WING NO. 1

## NASA AMES WIND TUNNEL TEST 231-1-11

## A-7 TRANSONIC WING DESIGNS

SYM RUN	CONF	MACH	RN/FT	
+	131	A-7	0.90	6.02 MILLION
□	208	NO.1	0.90	5.99 MILLION

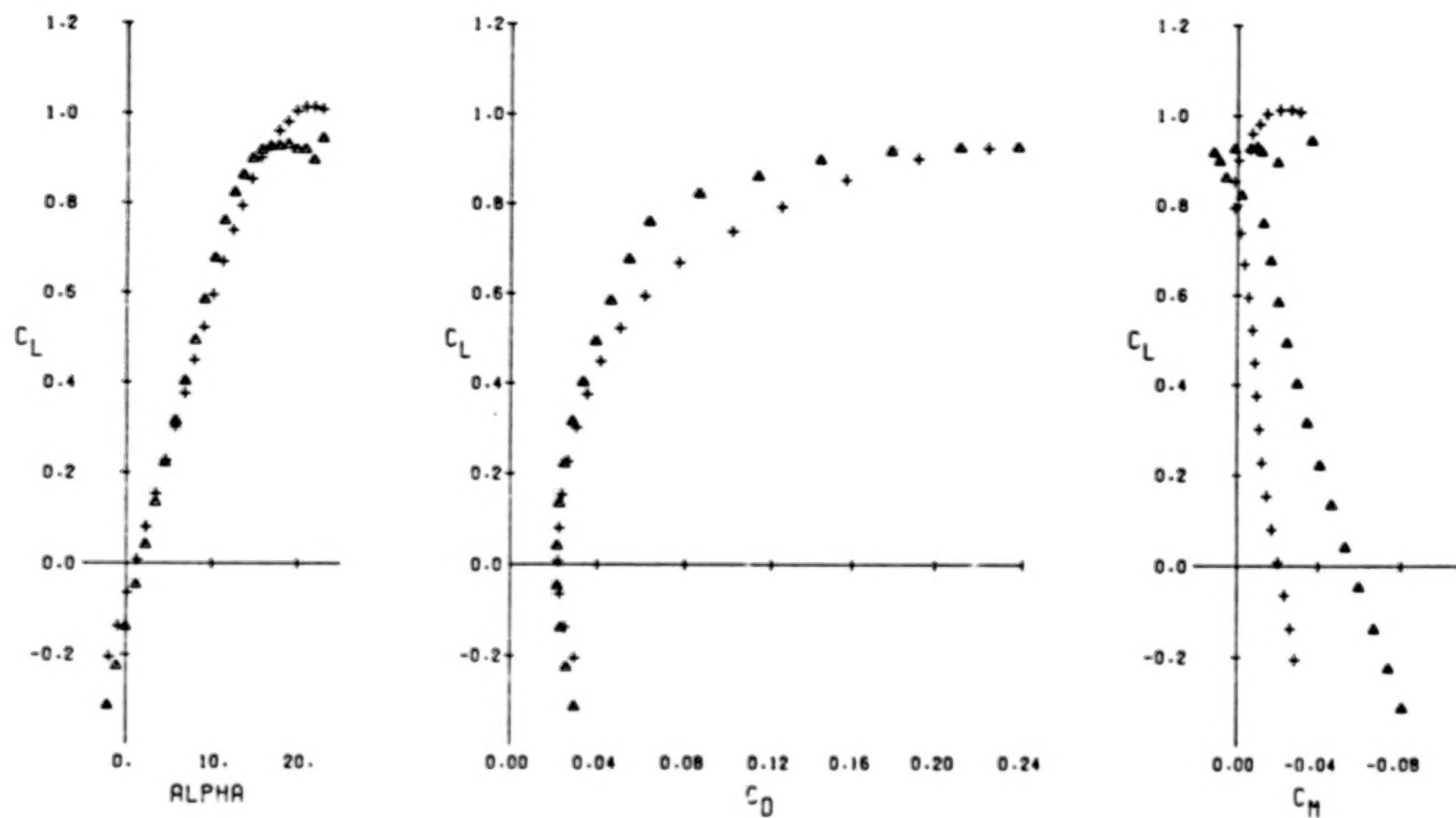


(G) MACH = 0.90

FIGURE 12.- COMPARISON OF AERODYNAMIC PARAMETERS FOR THE A-7 AND WING NO. 1

NASA AMES WIND TUNNEL TEST 231-1-11  
 A-7 TRANSONIC WING DESIGNS

SYM RUN CONF MACH RN/FT  
 + 11B R-7 0.40 5.04 MILLION  
 ▲ 303 NO.2 0.40 5.19 MILLION

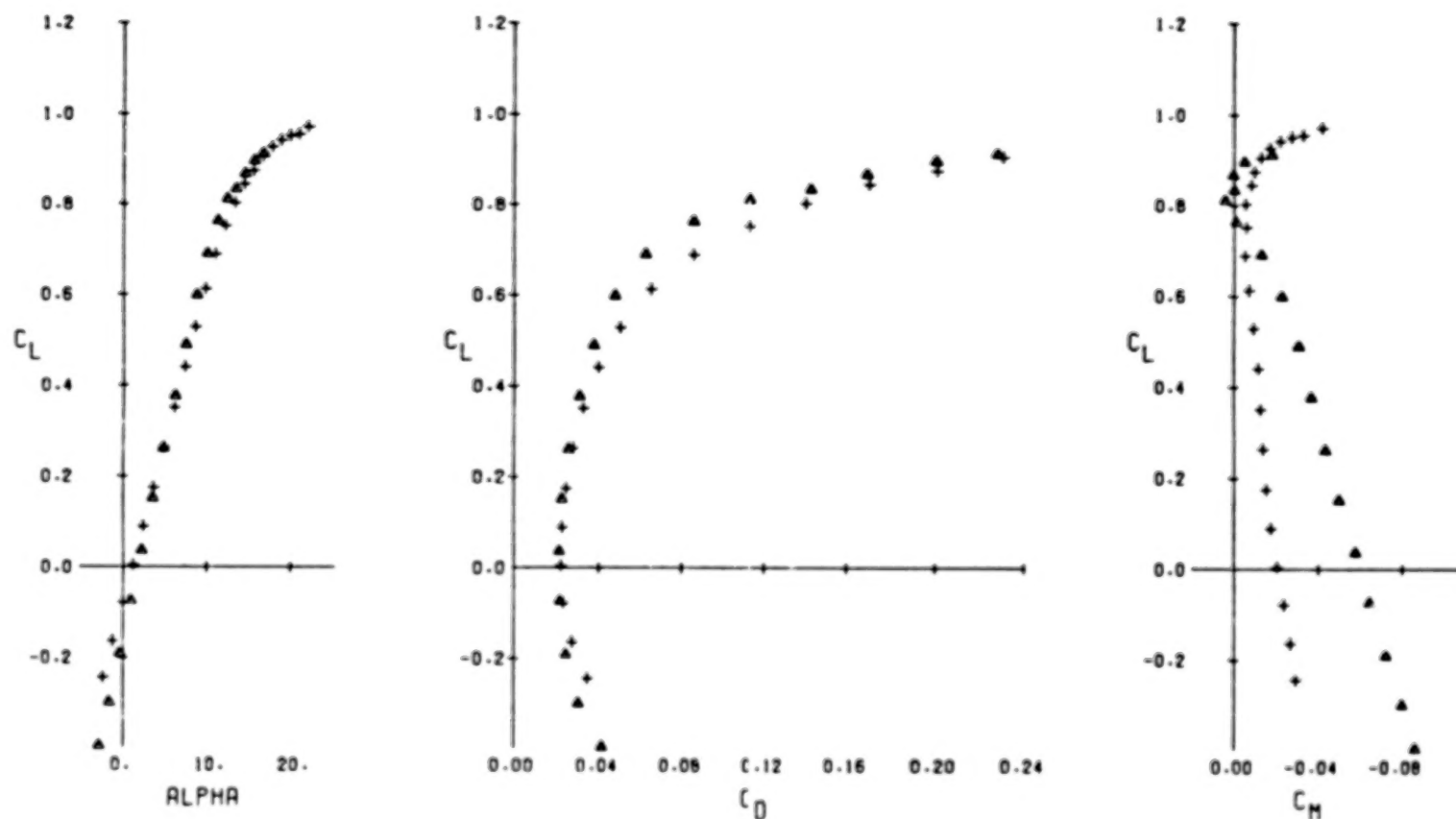


(A) MACH = 0.40

FIGURE 13.- COMPARISON OF AERODYNAMIC PARAMETERS FOR THE A-7 AND WING NO. 2

NASA AMES WIND TUNNEL TEST 231-1-11  
 A-7 TRANSONIC WING DESIGNS

SYM RUN CONF MACH RN/FT  
 + 119 R-7 0.60 5.98 MILLION  
 ▲ 304 NO.2 0.60 6.03 MILLION

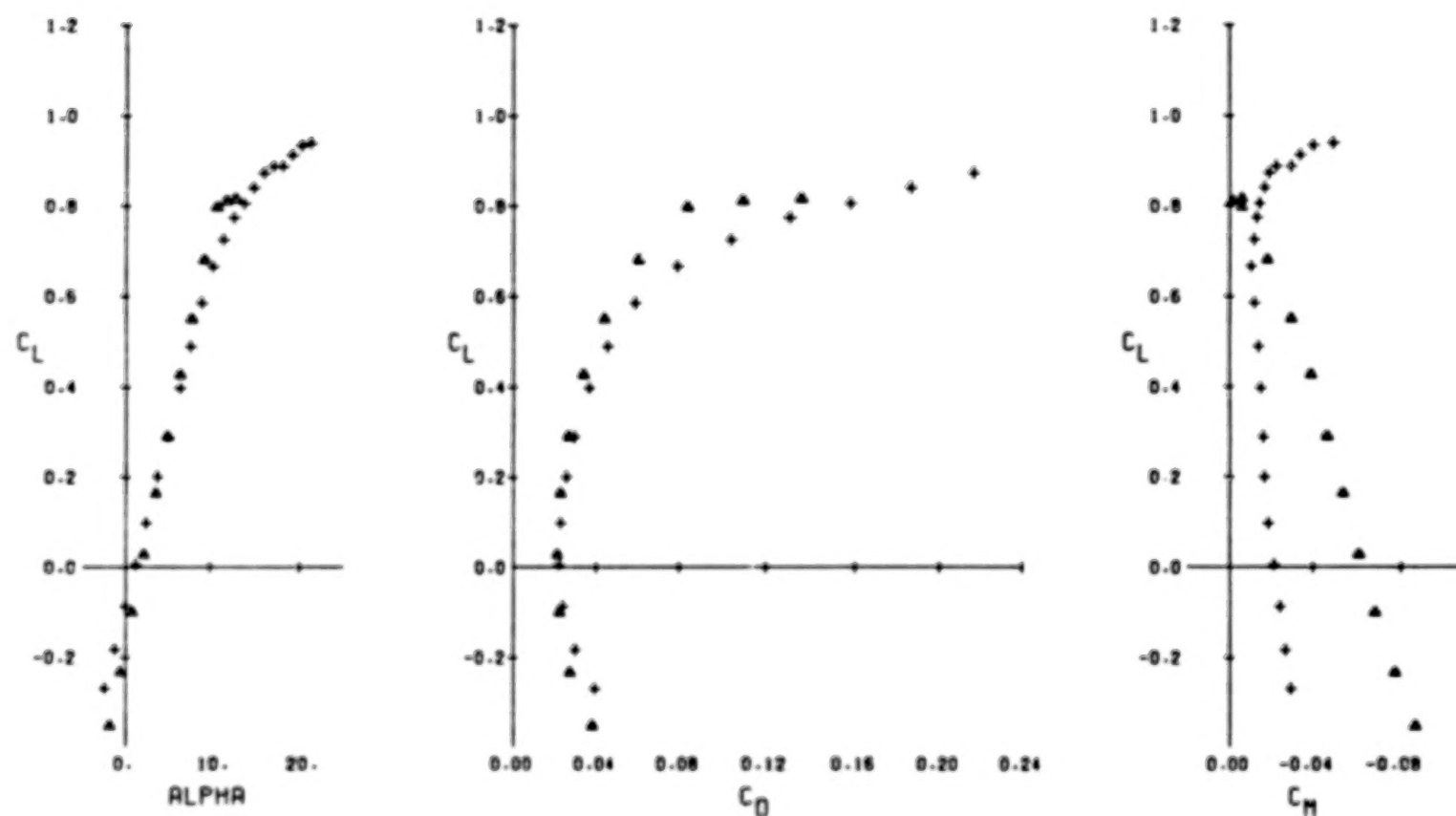


(B) MACH = 0.60

FIGURE 13.- COMPARISON OF AERODYNAMIC PARAMETERS FOR THE A-7 AND WING NO. 2

NASA AMES WIND TUNNEL TEST 231-1-11  
 A-7 TRANSONIC WING DESIGNS

SYM RUN CONF MACH RM/FT  
 + 120 R-7 0.70 6.03 MILLION  
 ▲ 305 NO.2 0.70 6.04 MILLION



(C) MACH = 0.70

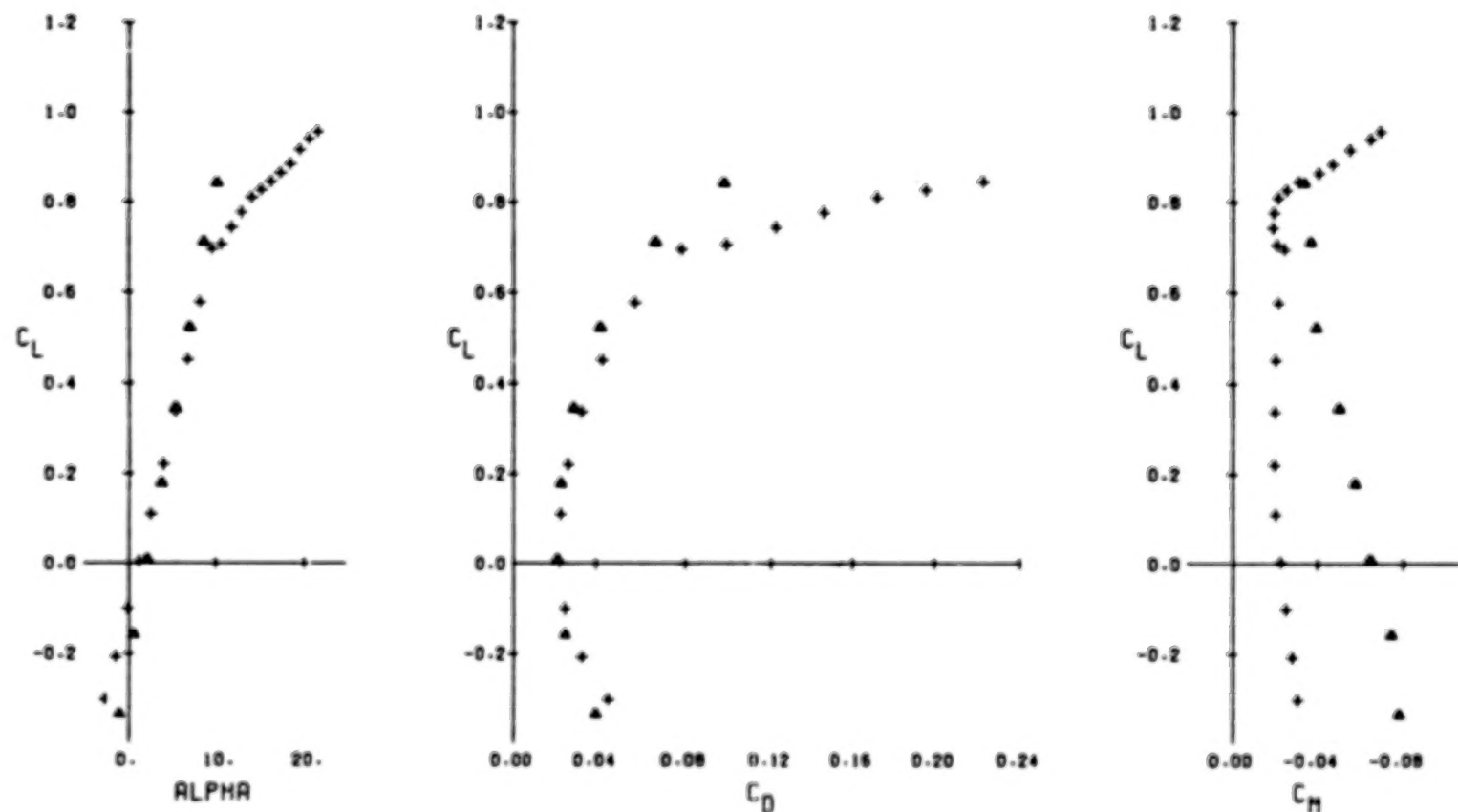
FIGURE 13.- COMPARISON OF AERODYNAMIC PARAMETERS FOR THE A-7 AND WING NO. 2

## NASA AMES WIND TUNNEL TEST 231-1-11

## A-7 TRANSONIC WING DESIGNS

SYM RUN CONF MACH BN/FT

- + 121 A-7 0.80 5.99 MILLION
- ▲ 306 NO.2 0.80 6.06 MILLION



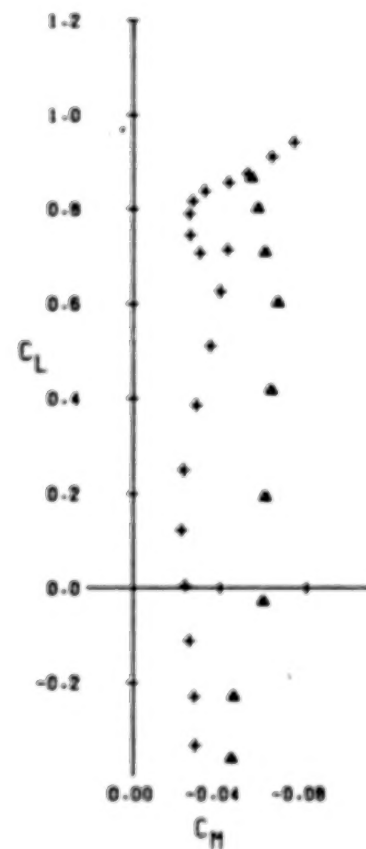
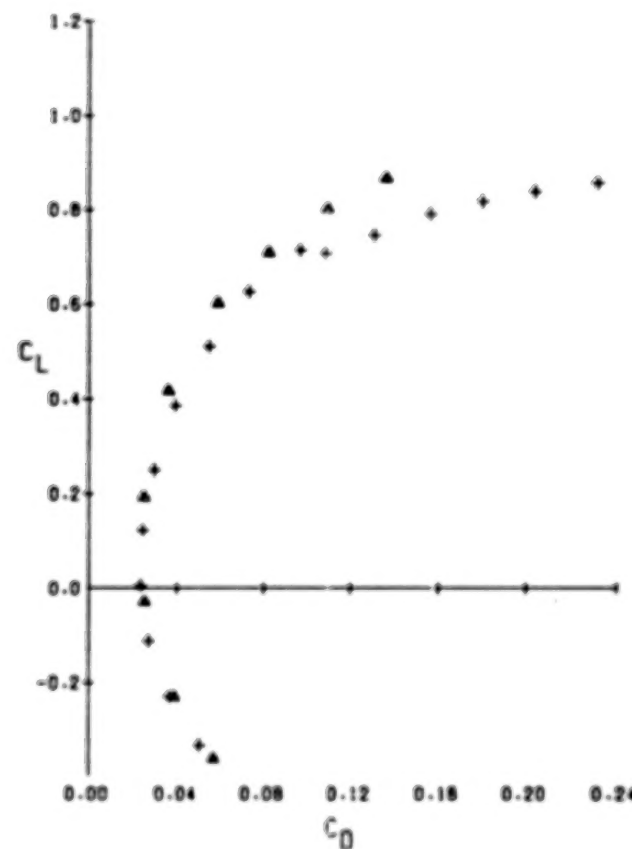
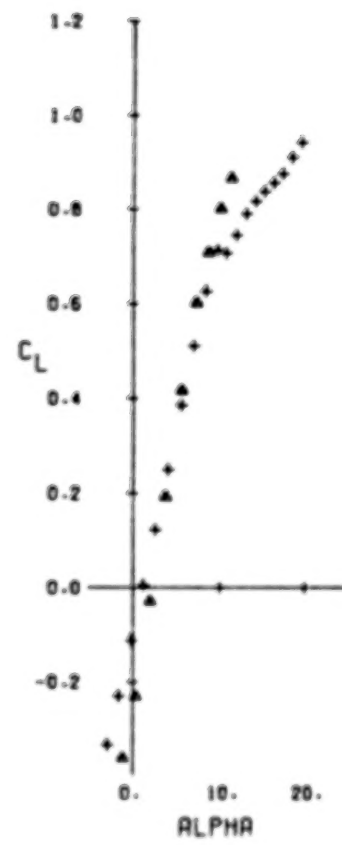
(D) MACH = 0.80

FIGURE 13.- COMPARISON OF AERODYNAMIC PARAMETERS FOR THE A-7 AND WING NO. 2

## NASA AMES WIND TUNNEL TEST 231-1-11

## A-7 TRANSONIC WING DESIGNS

SYM RUN CDMF MACH BN/FT  
 + 122 A-7 0.25 5.98 MILLION  
 ▲ 307 NO. 2 0.85 6.04 MILLION



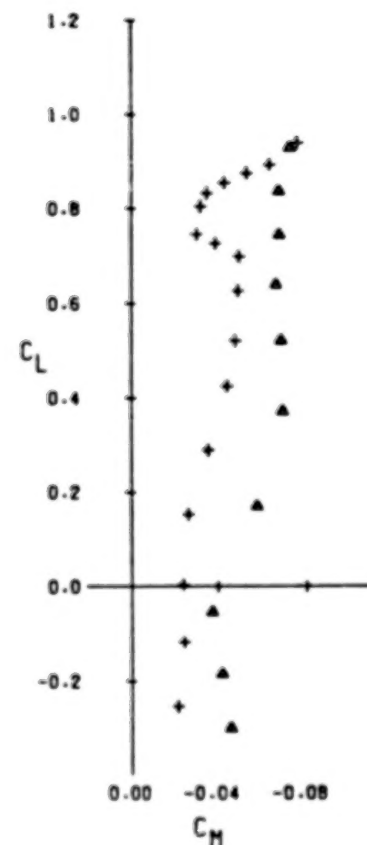
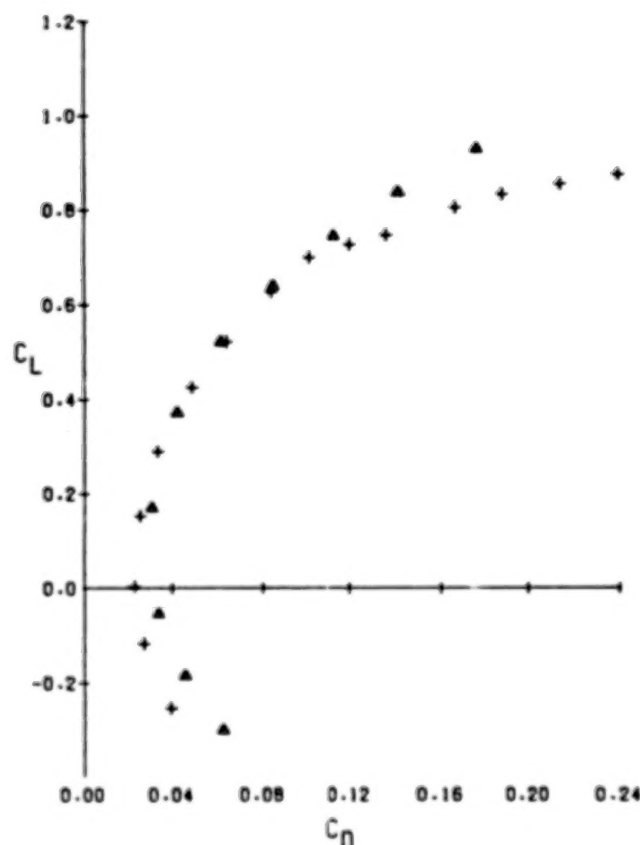
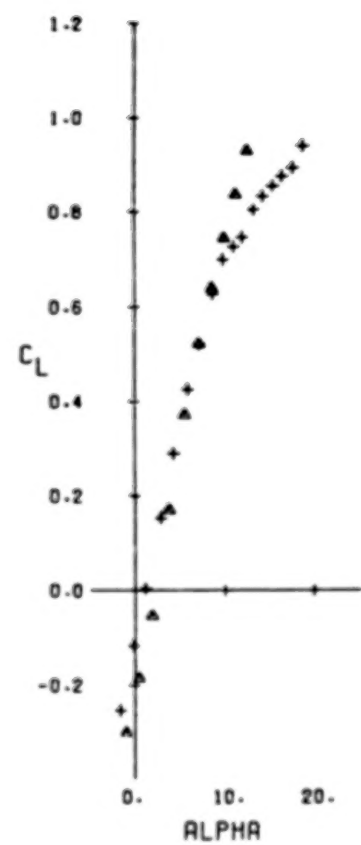
(E) MACH = 0.85

FIGURE 13.- COMPARISON OF AERODYNAMIC PARAMETERS FOR THE A-7 AND WING NO. 2

## NASA AMES WIND TUNNEL TEST 231-1-11

## A-7 TRANSONIC WING DESIGNS

SYM RUN CONF MACH RN/FT  
 + 130 A-7 0.88 5.98 MILLION  
 ▲ 312 NO.2 0.88 6.03 MILLION

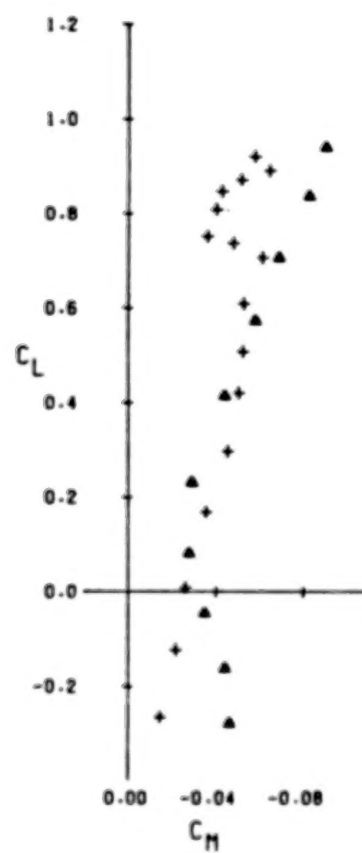
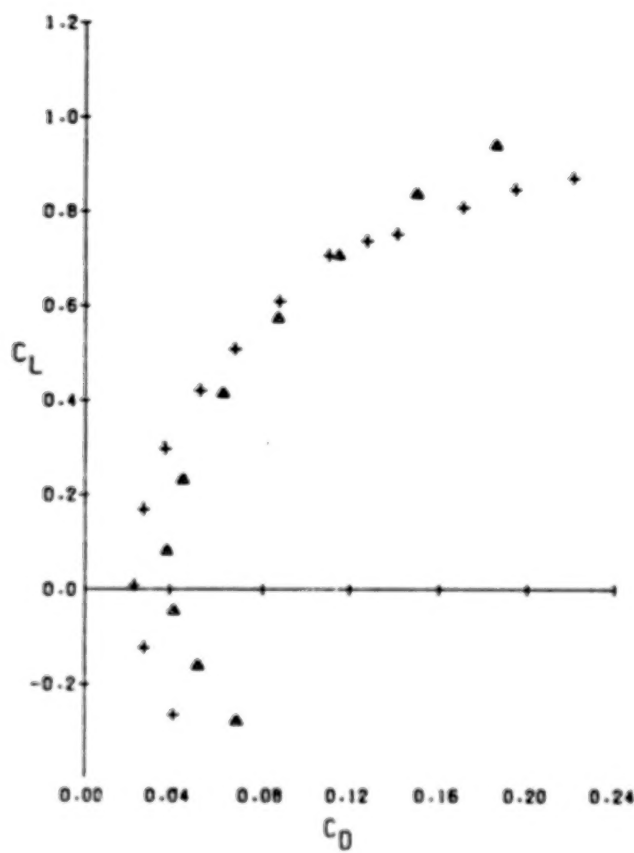
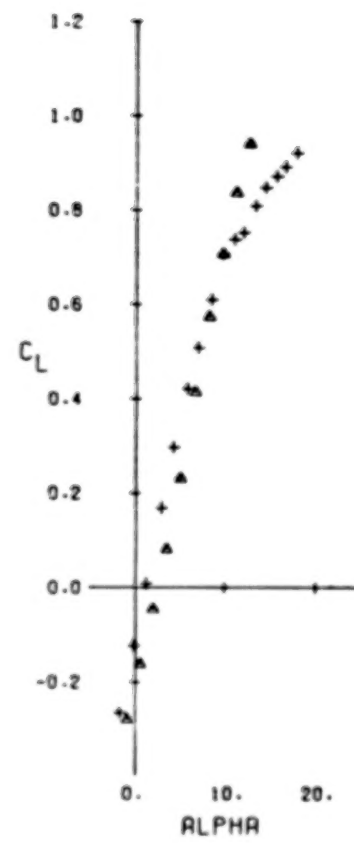


(F) MACH = 0.88

FIGURE 13.- COMPARISON OF AERODYNAMIC PARAMETERS FOR THE A-7 AND WING NO. 2

NASA AMES WIND TUNNEL TEST 231-1-11  
 A-7 TRANSONIC WING DESIGNS

SYM RUN CONE MACH RN/FT  
 + 131 A-7 0.90 6.02 MILLION  
 ▲ 313 NO.2 0.90 6.00 MILLION



(G) MACH = 0.90

FIGURE 13.- COMPARISON OF AERODYNAMIC PARAMETERS FOR THE A-7 AND WING NO. 2

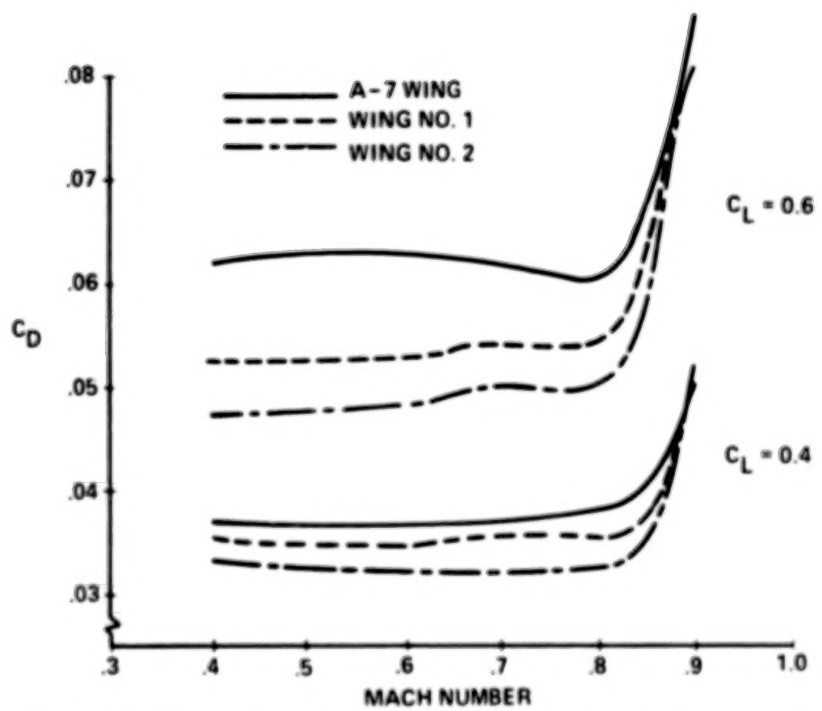
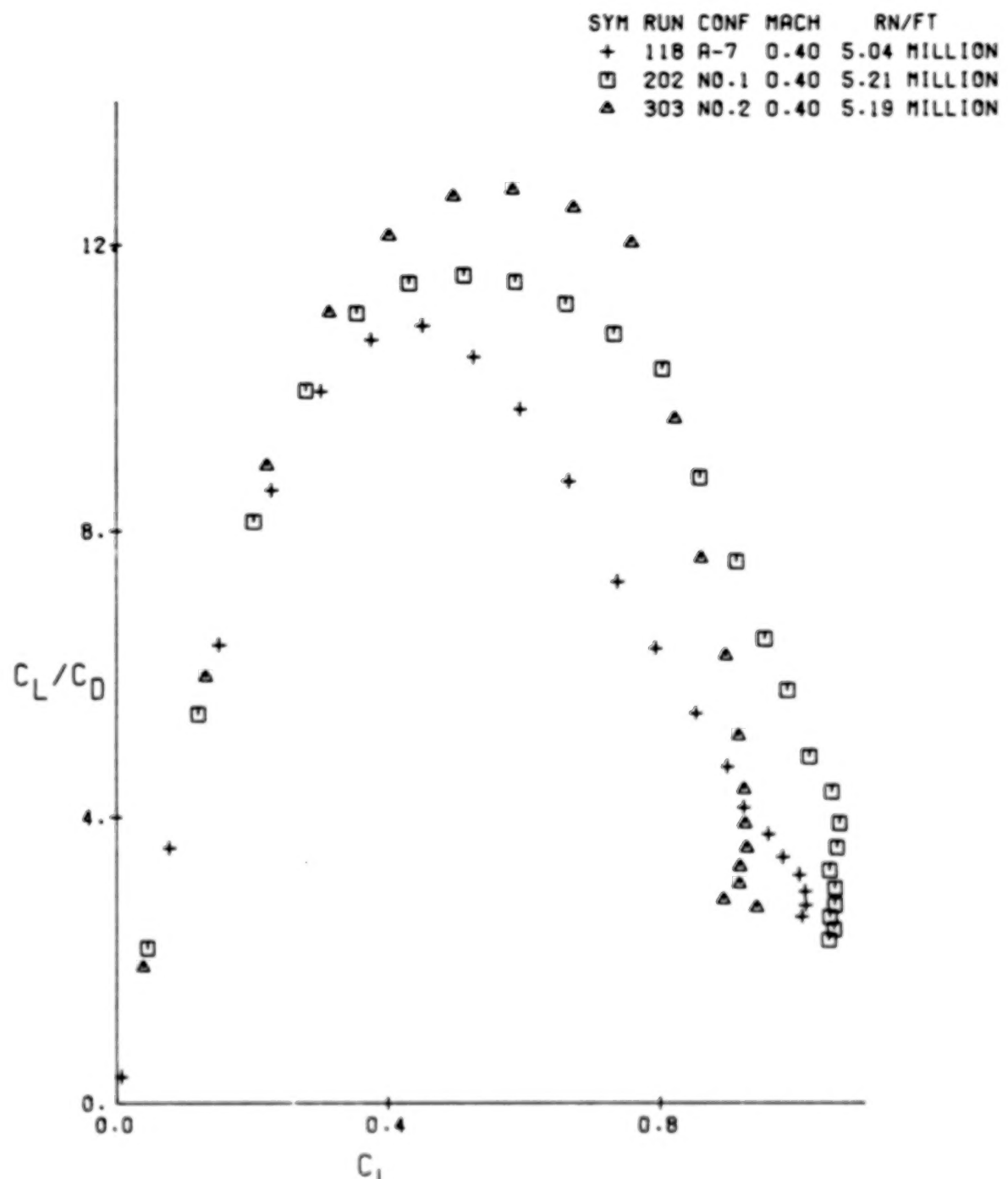


FIGURE 14. EXPERIMENTAL DRAG DIVERGENCE AT CONSTANT LIFT COEFFICIENTS

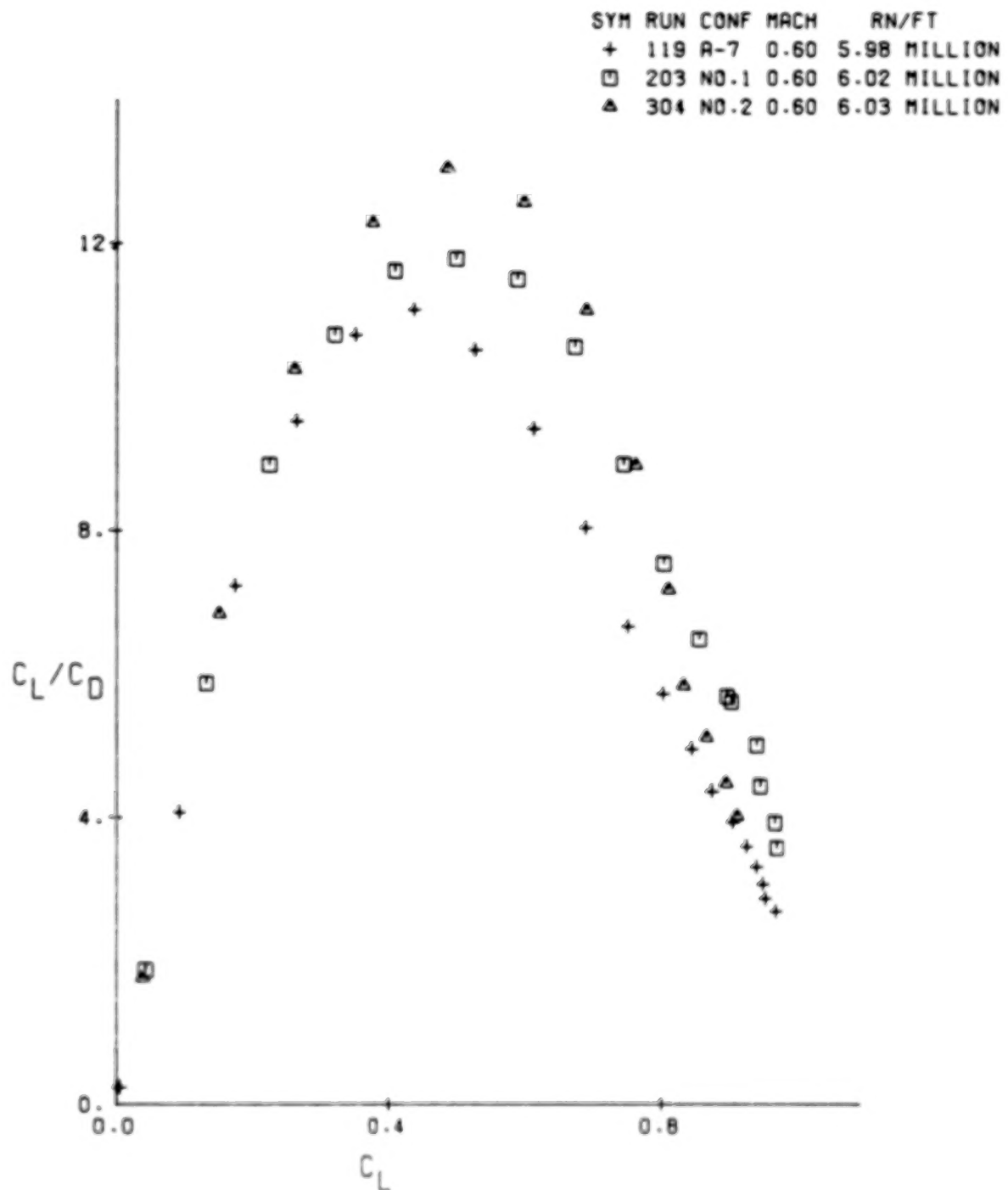
NASA AMES WIND TUNNEL TEST 231-1-11



(A) MACH = 0.40

FIGURE 15.- LIFT TO DRAG RATIOS

NASA AMES WIND TUNNEL TEST 231-1-11

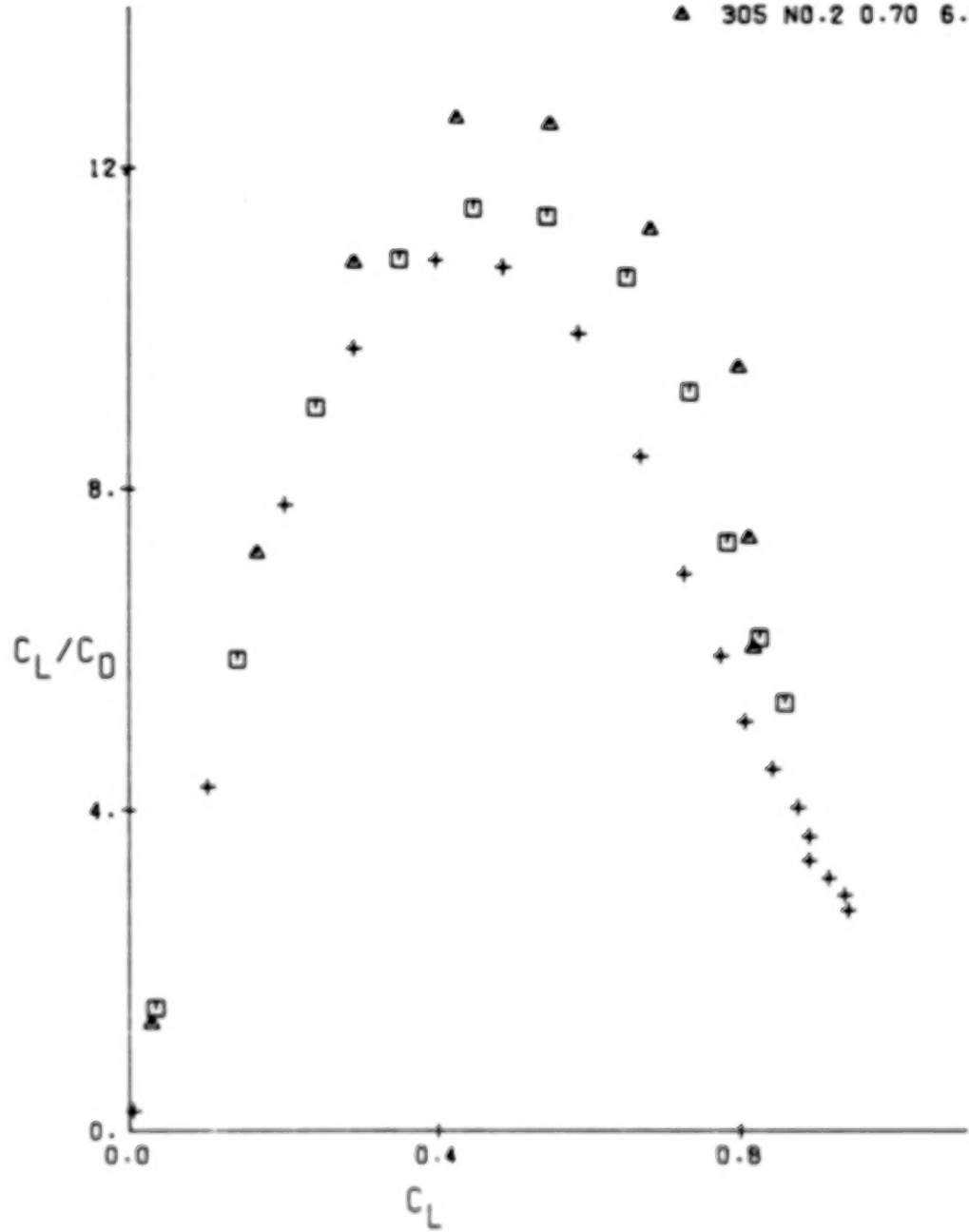


(B) MACH = 0.60

FIGURE 15.- LIFT TO DRAG RATIOS

NASA AMES WIND TUNNEL TEST 231-1-11

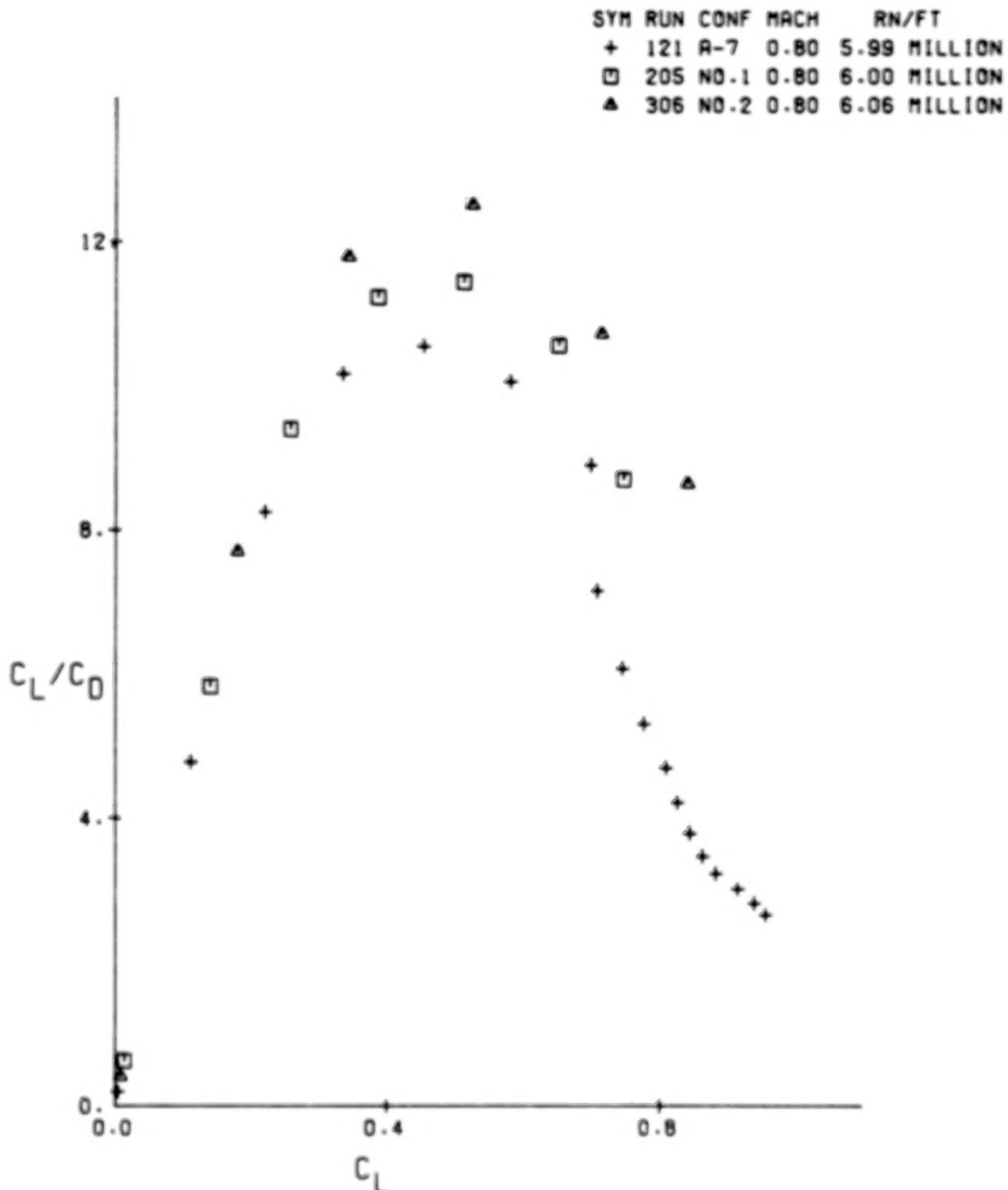
SYM	RUN	CONF	MACH	RN/FT
+	120	A-7	0.70	6.03 MILLION
□	204	NO.1	0.70	5.99 MILLION
▲	305	NO.2	0.70	6.04 MILLION



(C) MACH = 0.70

FIGURE 15.- LIFT TO DRAG RATIOS

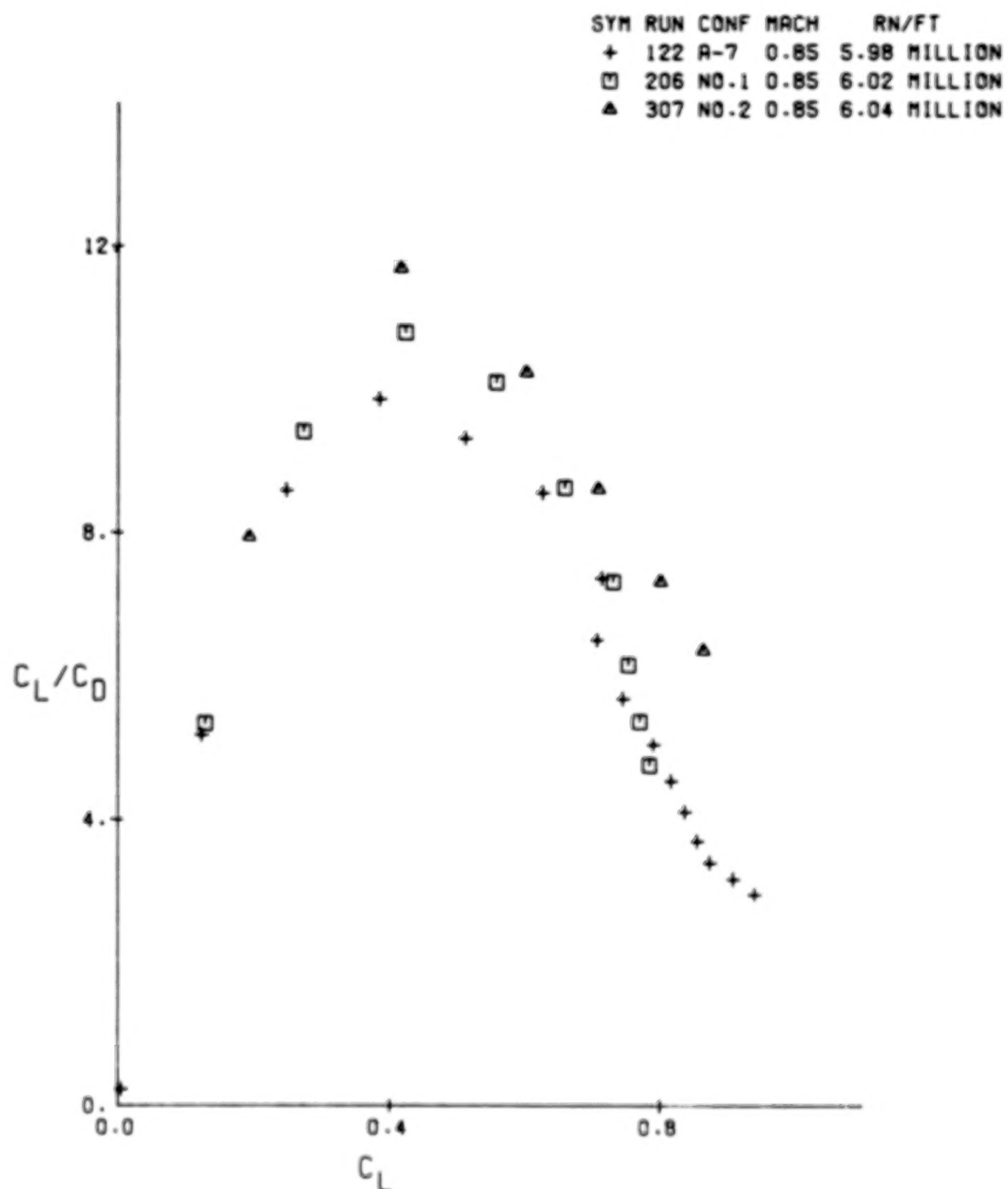
NASA AMES WIND TUNNEL TEST 231-1-11



(D) MACH = 0.80

FIGURE 15.- LIFT TO DRAG RATIOS

NASA AMES WIND TUNNEL TEST 231-1-11

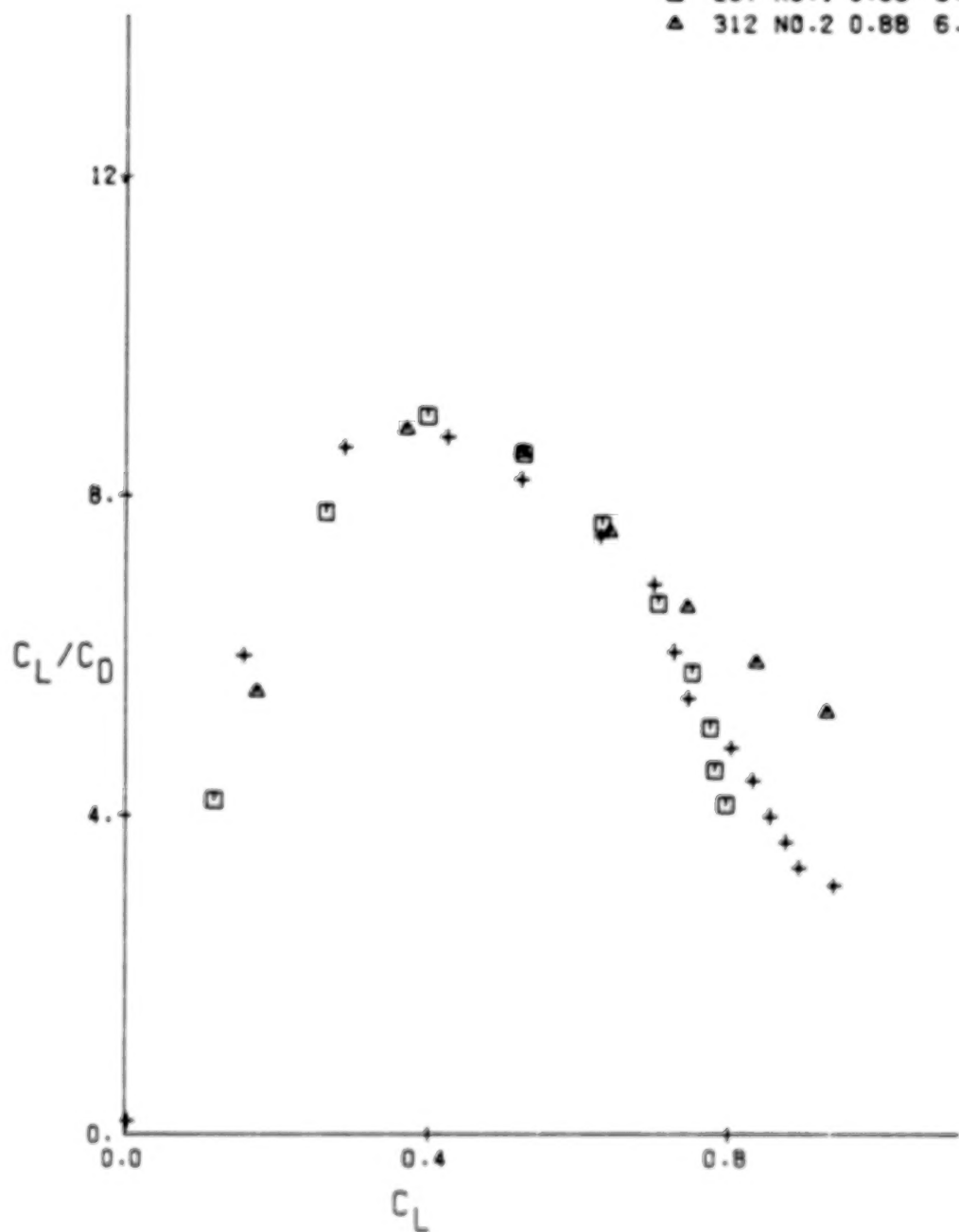


(E) MACH = 0.85

FIGURE 15.- LIFT TO DRAG RATIOS

NASA AMES WIND TUNNEL TEST 231-1-11

SYM	RUN	CONF	MACH	RN/FT
+	130	A-7	0.88	5.98 MILLION
□	207	NO.1	0.88	5.99 MILLION
△	312	NO.2	0.88	6.03 MILLION

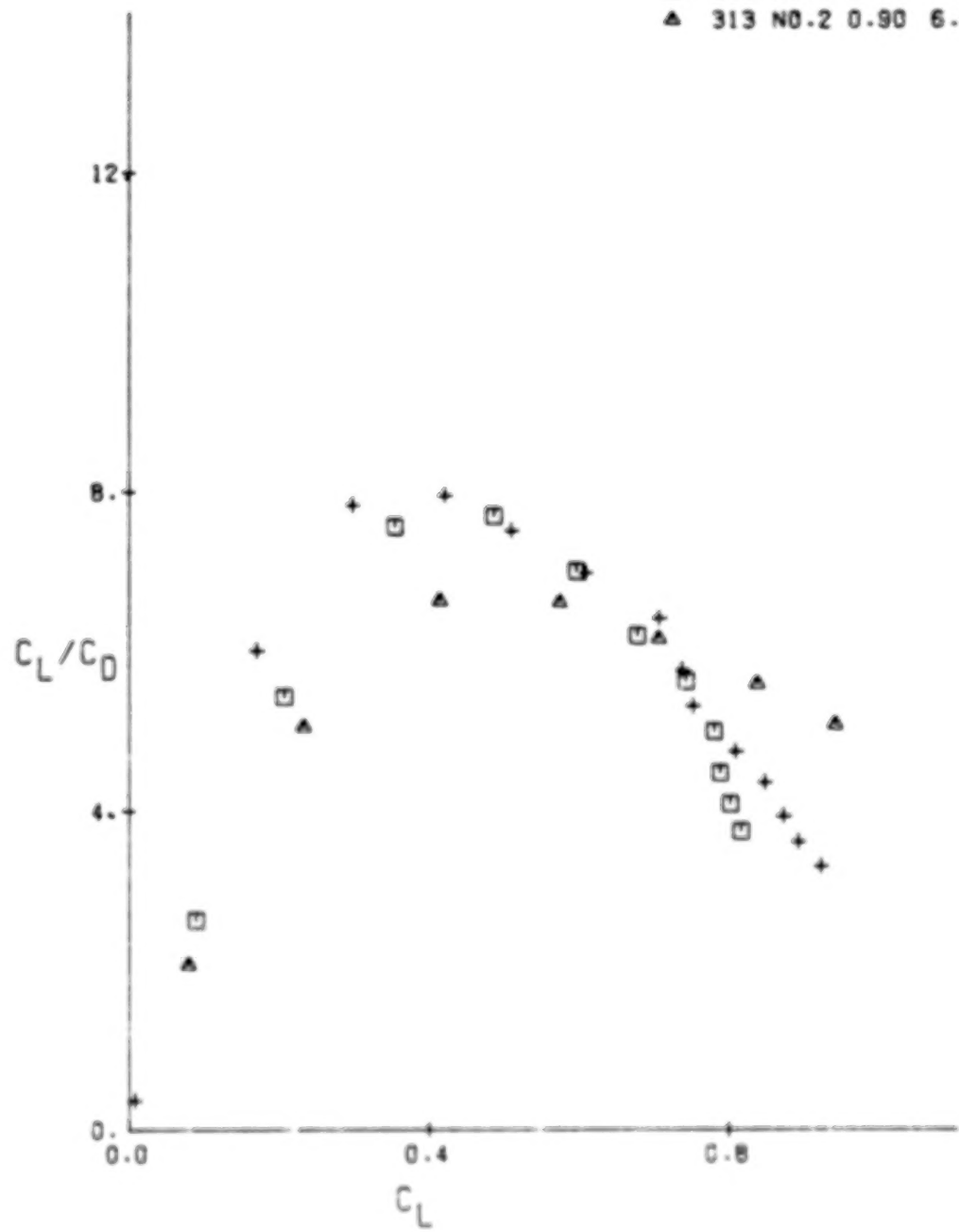


(F) MACH = 0.88

FIGURE 15.- LIFT TO DRAG RATIOS

NASA AMES WIND TUNNEL TEST 231-1-11

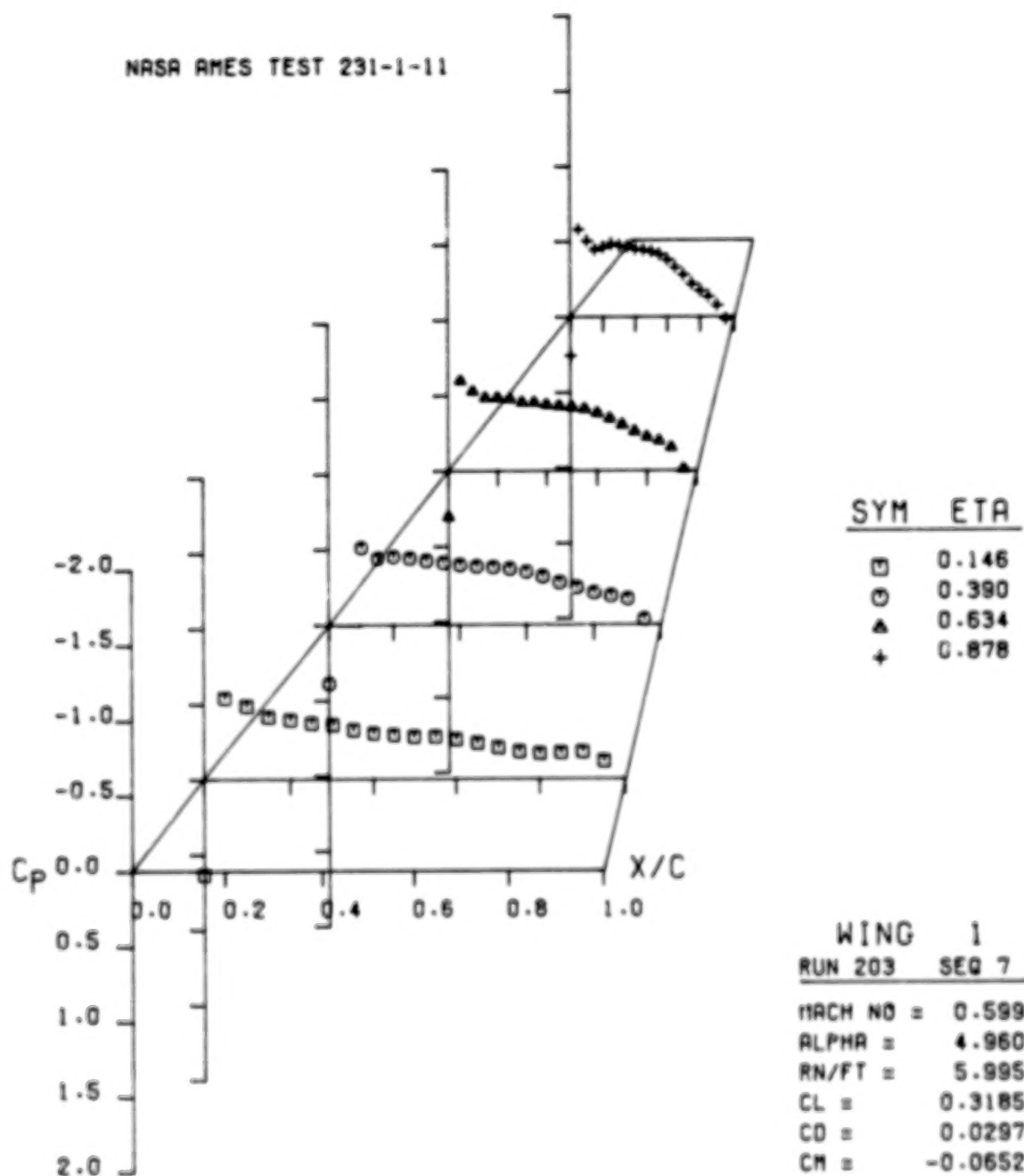
SYM	RUN	CONF	MACH	RN/FT
+	131	A-7	0.90	6.02 MILLION
□	208	N0.1	0.90	5.99 MILLION
△	313	N0.2	0.90	6.00 MILLION



(G) MACH = 0.90

FIGURE 15.- LIFT TO DRAG RATIOS

NASA AMES TEST 231-1-11



(A) ALPHA = 4.96

FIGURE 16.- WING NO. 1 UPPER SURFACE PRESSURES, MACH=0.599

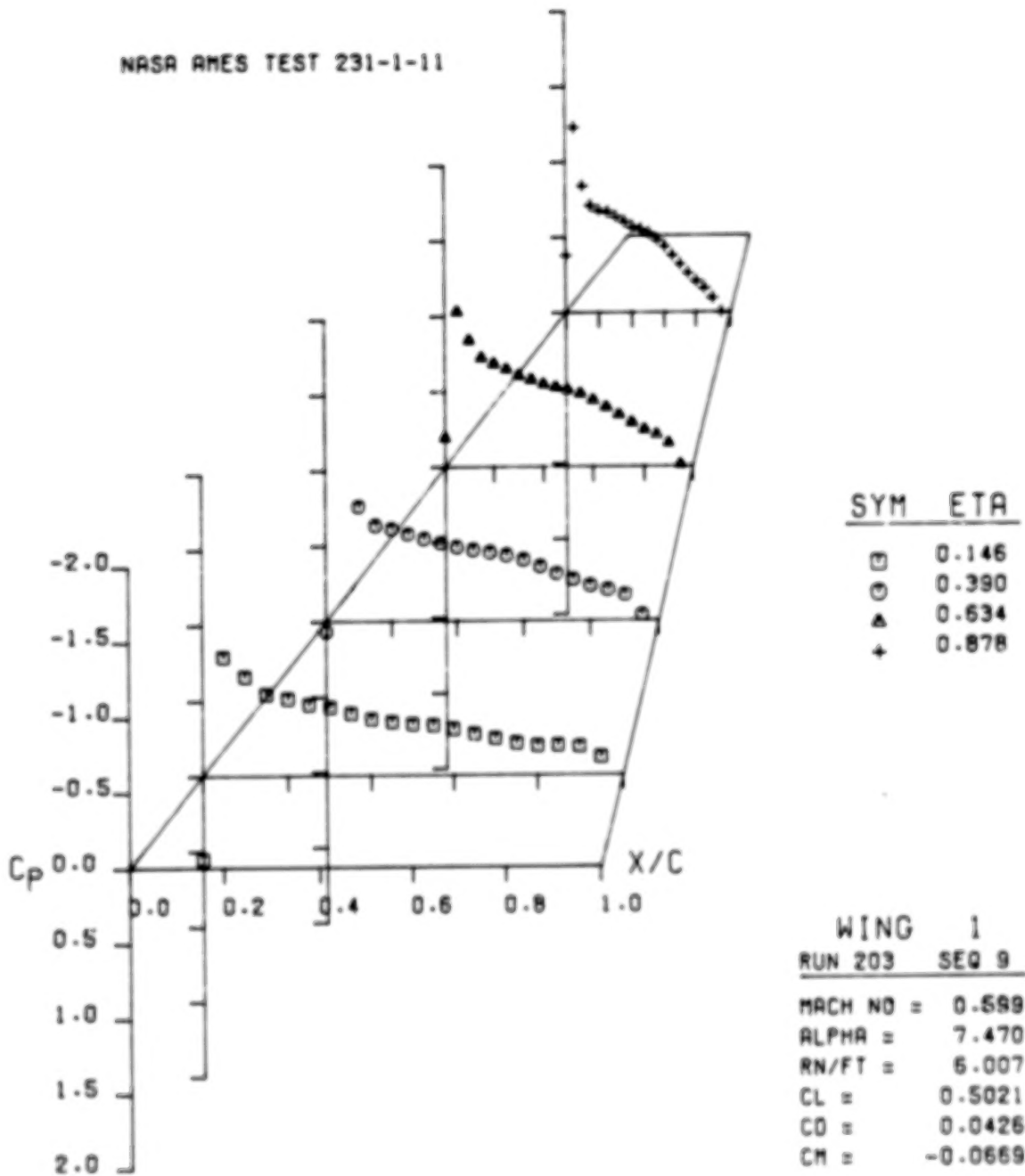


FIGURE 16.- WING NO. 1 UPPER SURFACE PRESSURES. MACH=0.599

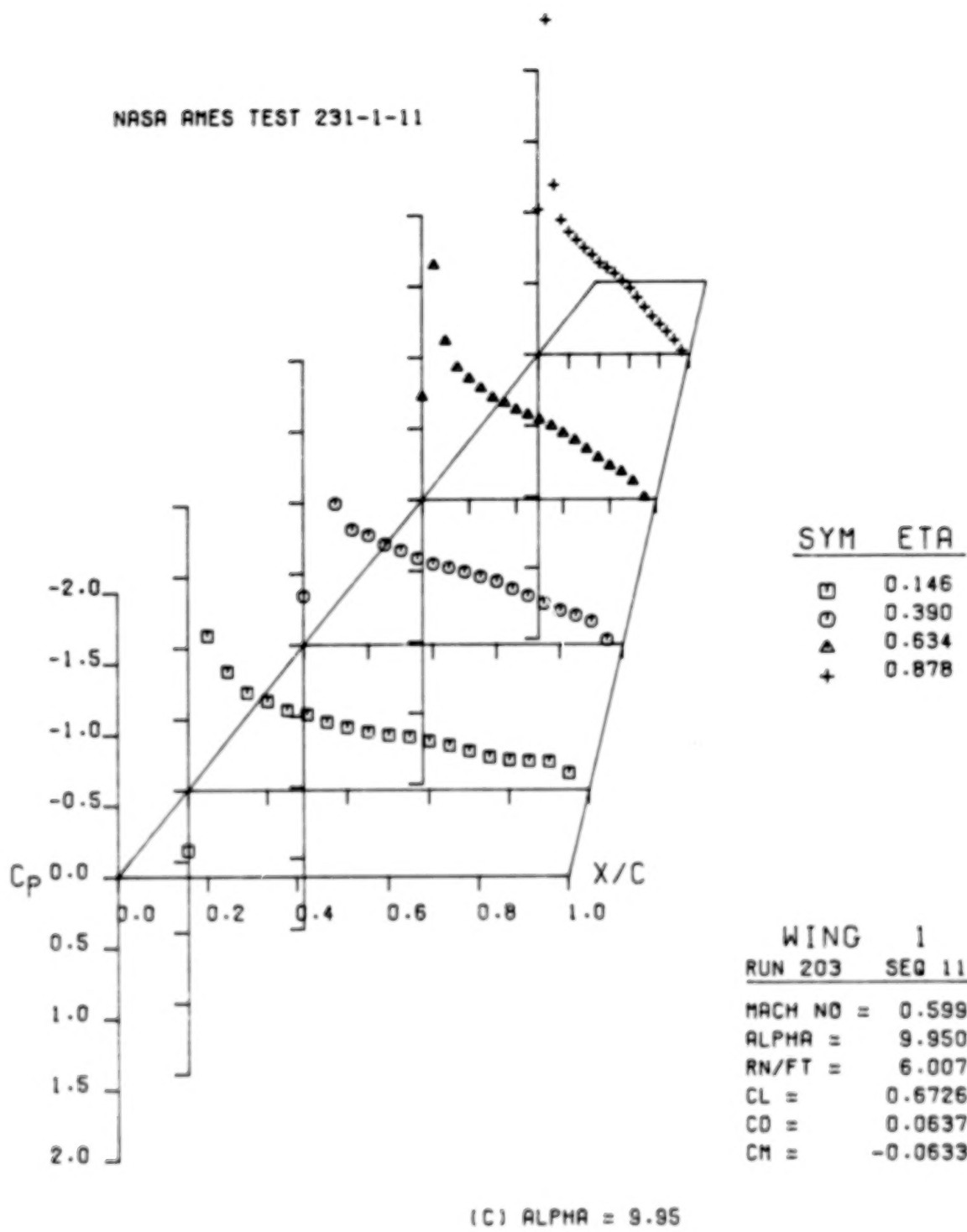


FIGURE 16.- WING NO. 1 UPPER SURFACE PRESSURES. MACH=0.599

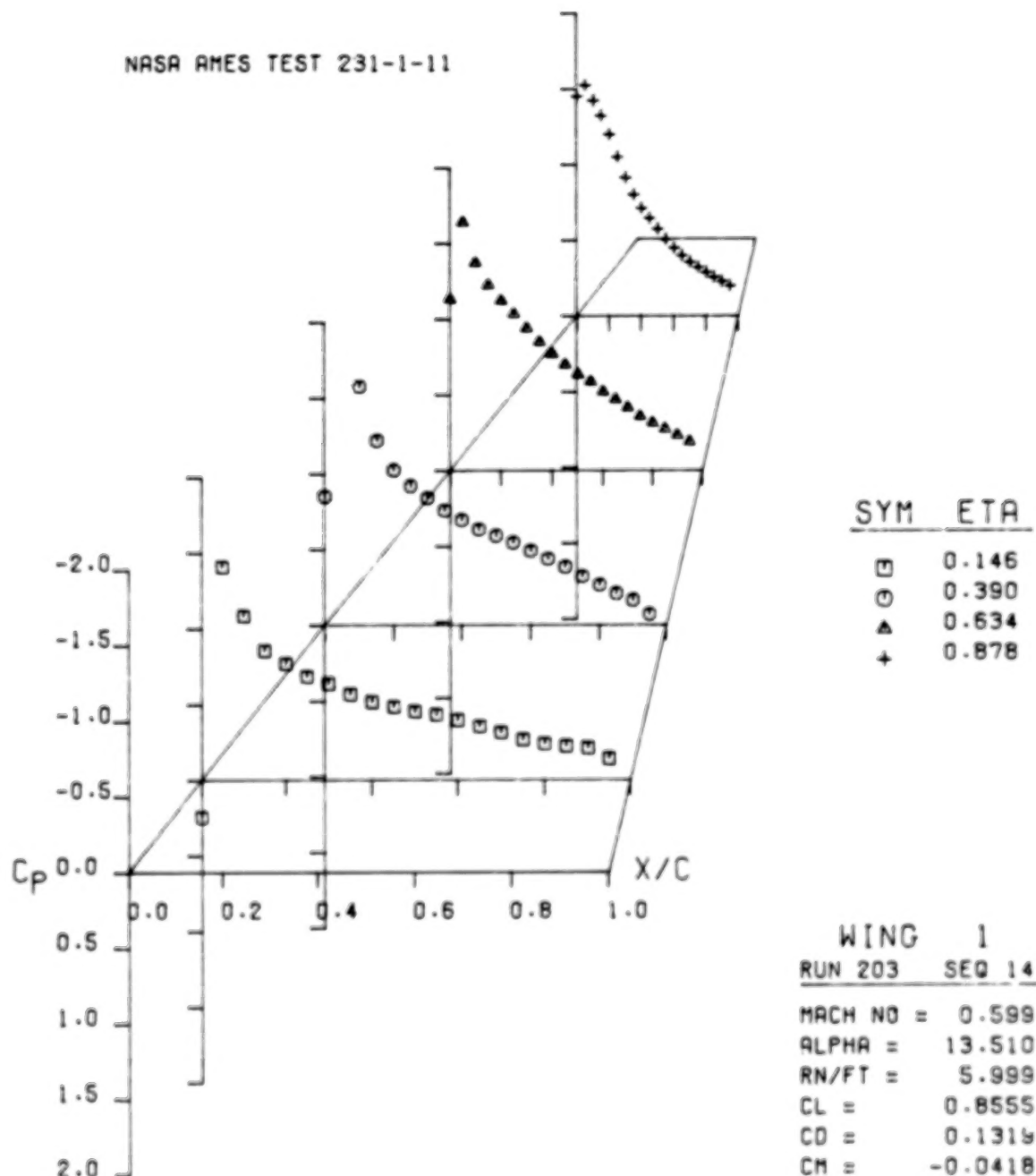


FIGURE 16.- WING NO. 1 UPPER SURFACE PRESSURES, MACH=0.599

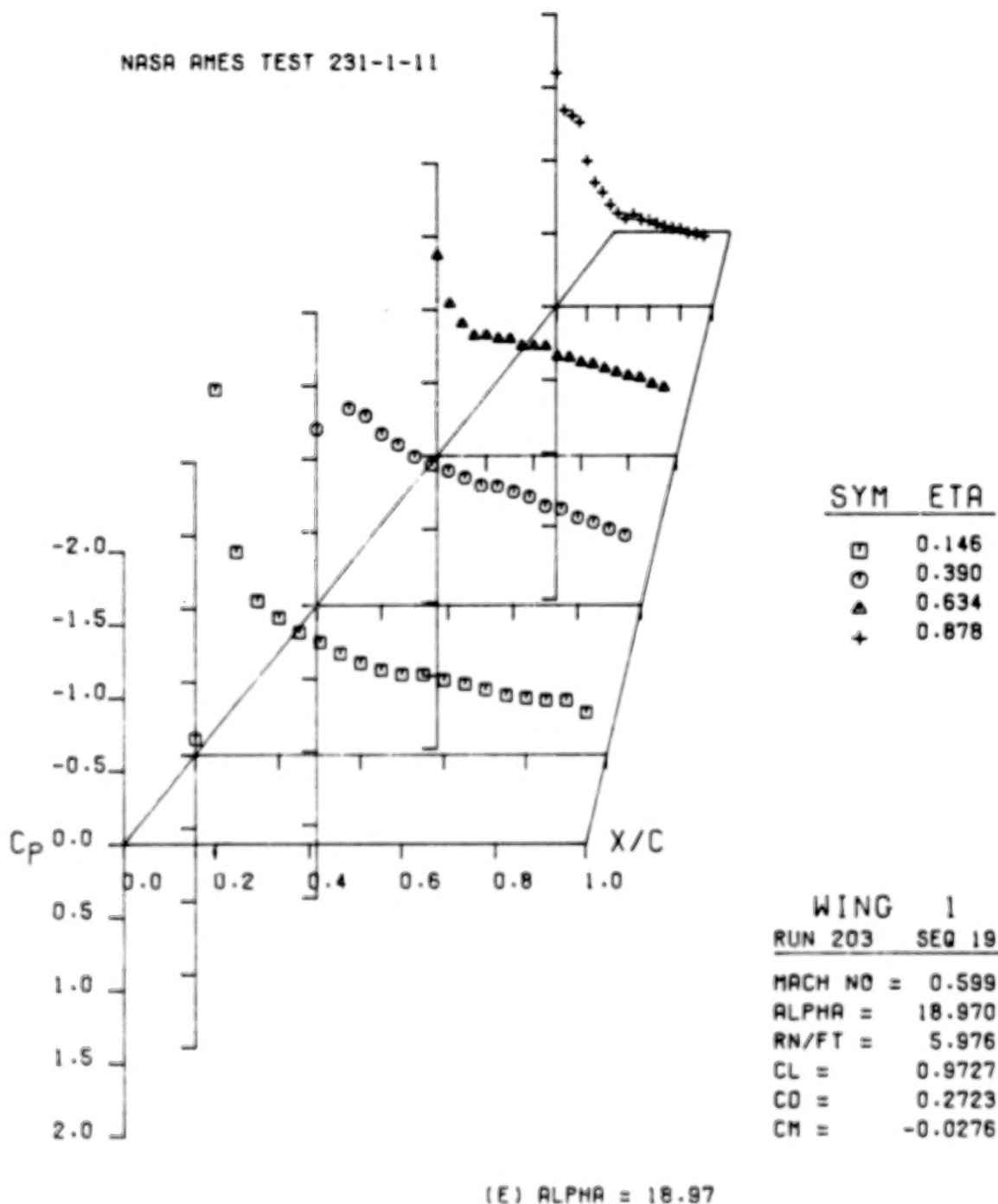
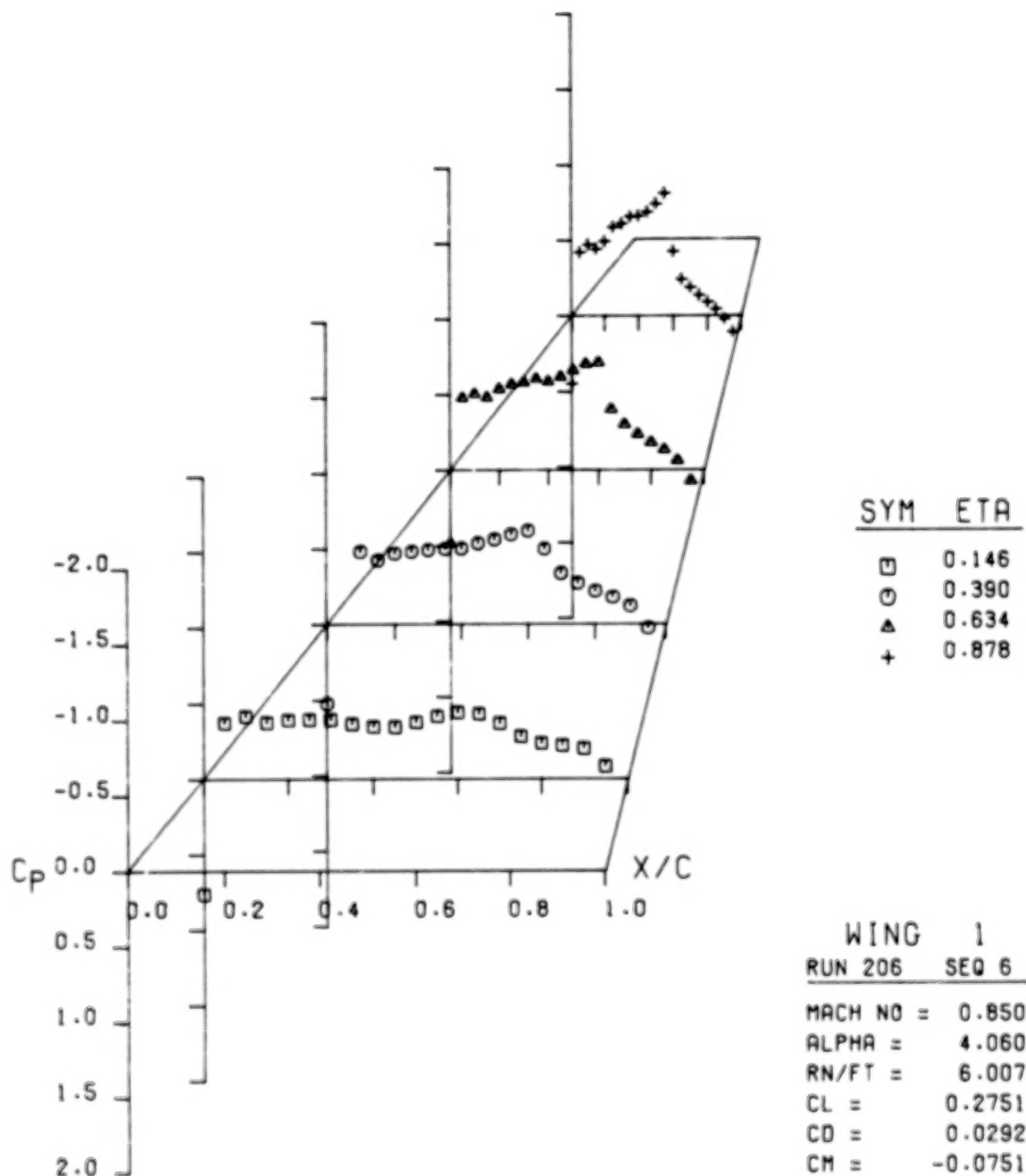
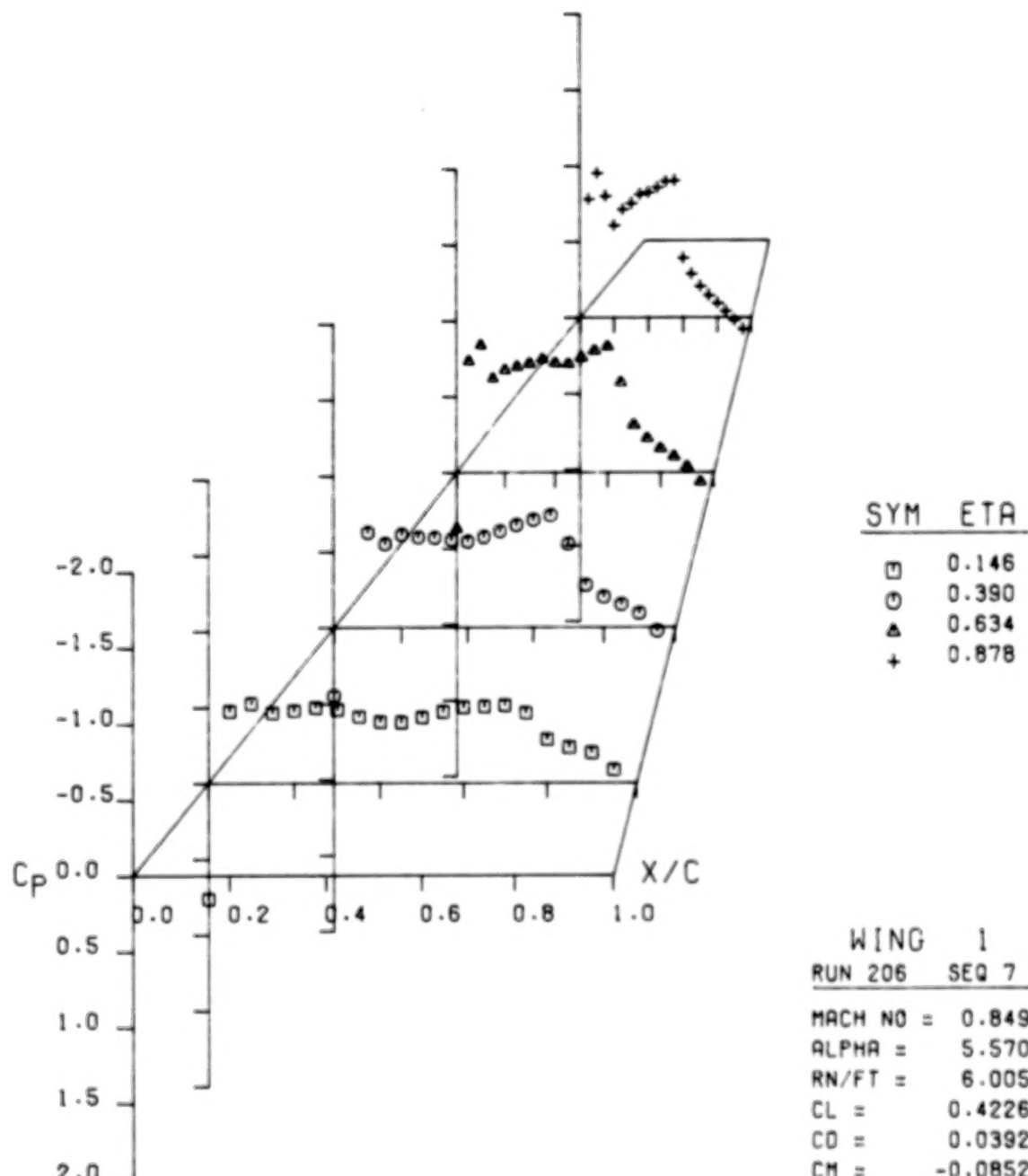


FIGURE 16.- WING NO. 1 UPPER SURFACE PRESSURES, MACH=0.599



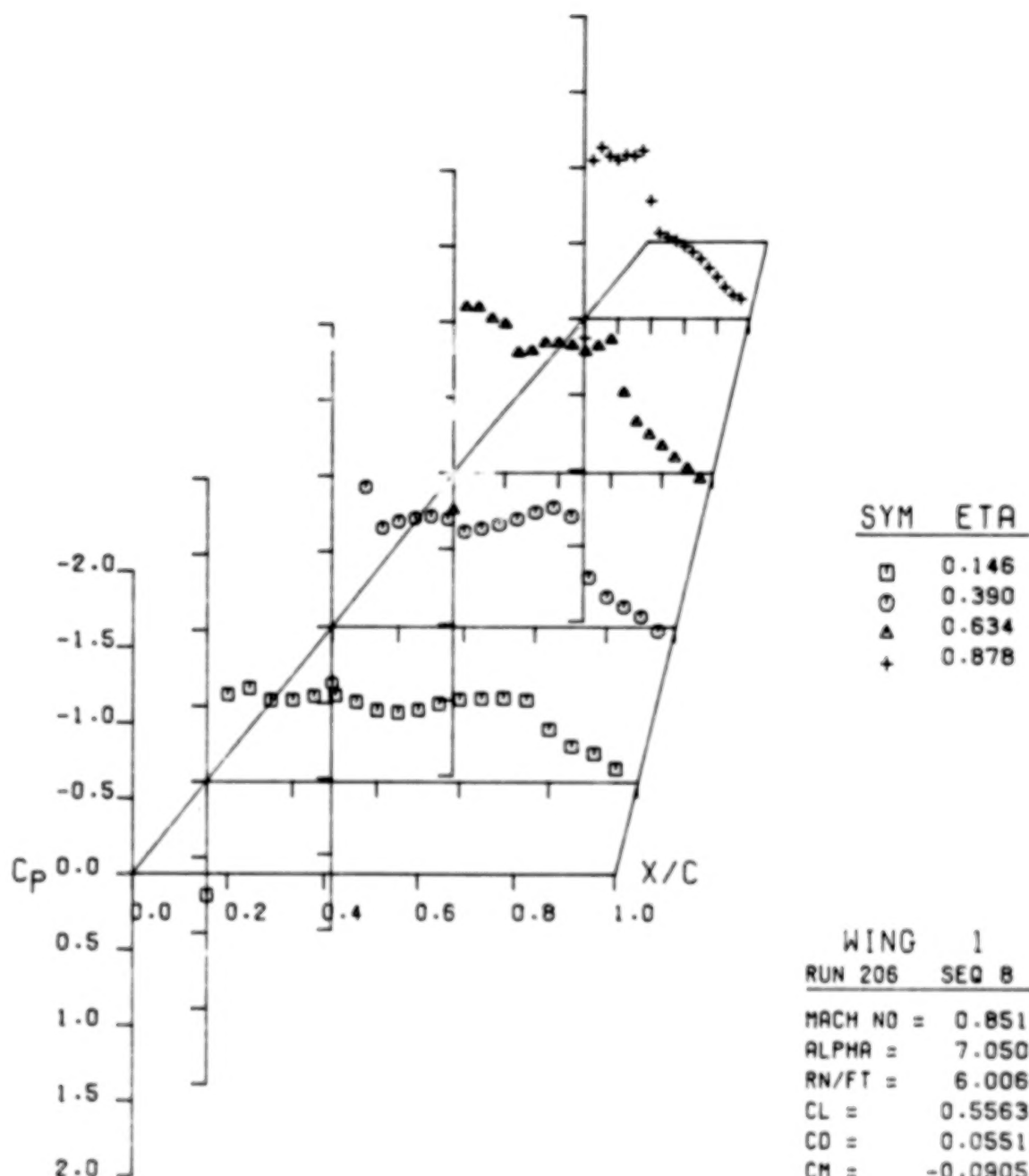
(A) ALPHA = 4.06

FIGURE 17.- WING NO. 1 UPPER SURFACE PRESSURES, MACH=0.85



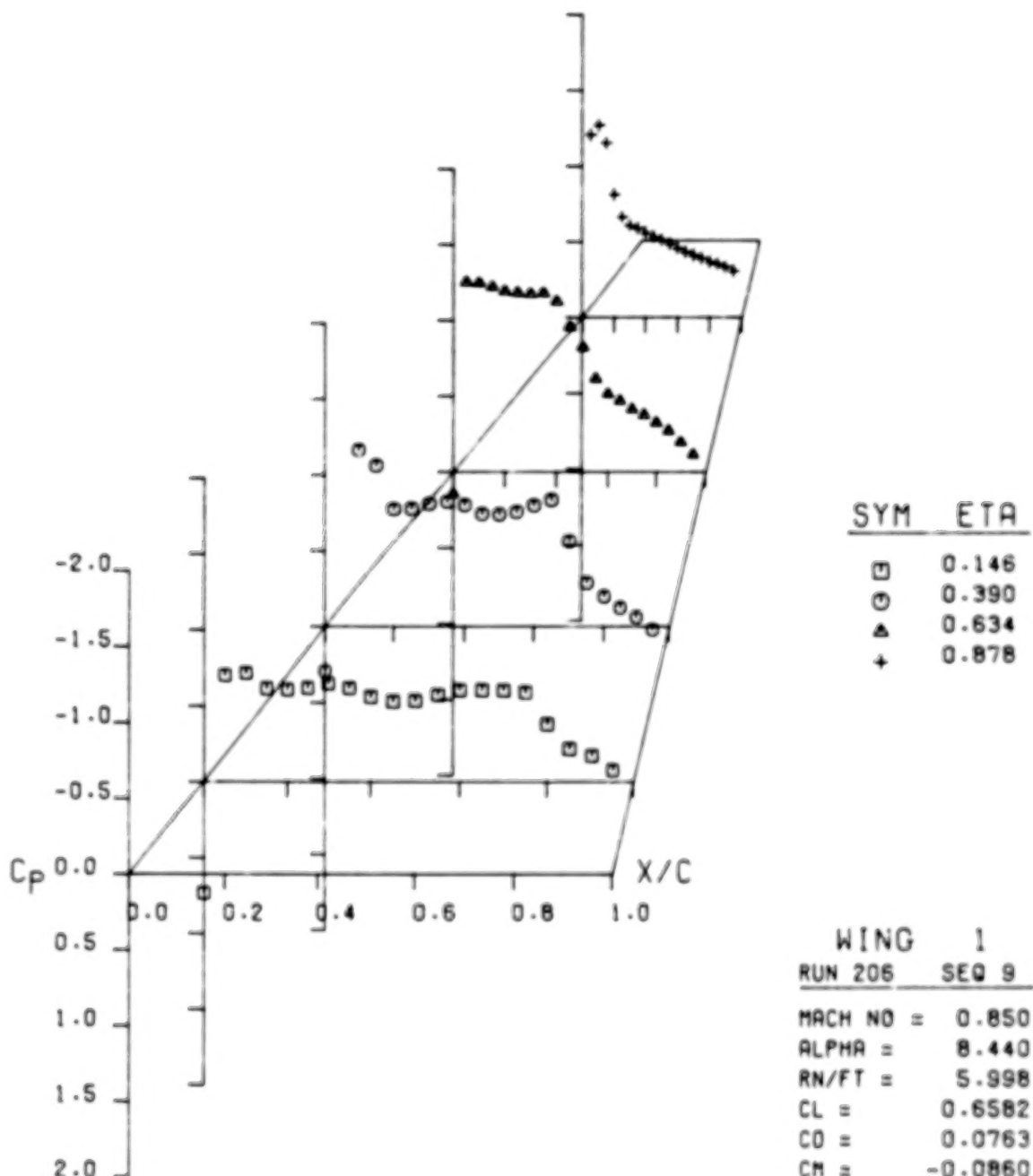
(B) ALPHA = 5.57

FIGURE 17.- WING NO. 1 UPPER SURFACE PRESSURES, MACH=0.85



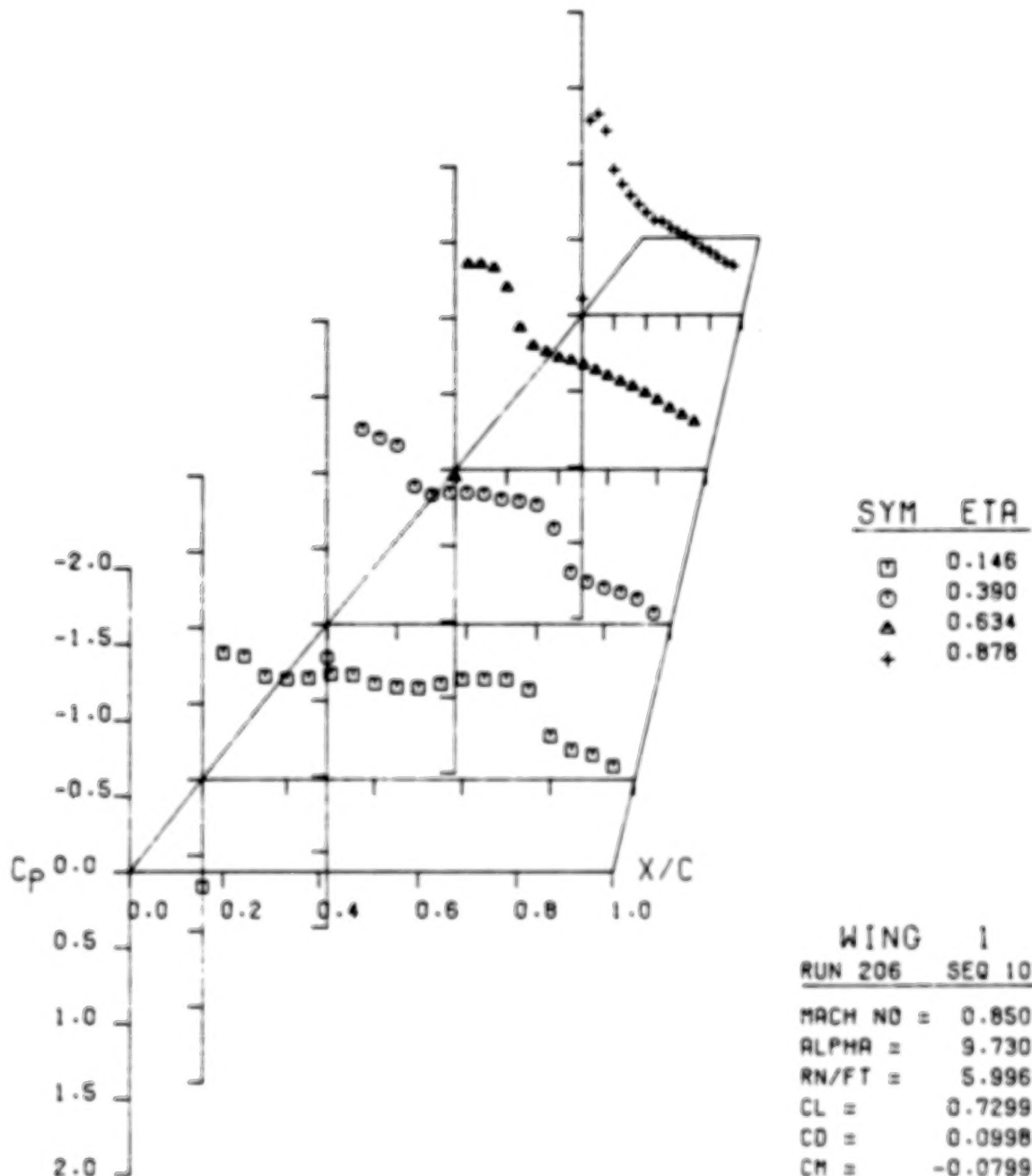
(C) ALPHA = 7.05

FIGURE 17.- WING NO. 1 UPPER SURFACE PRESSURES, MACH=0.85



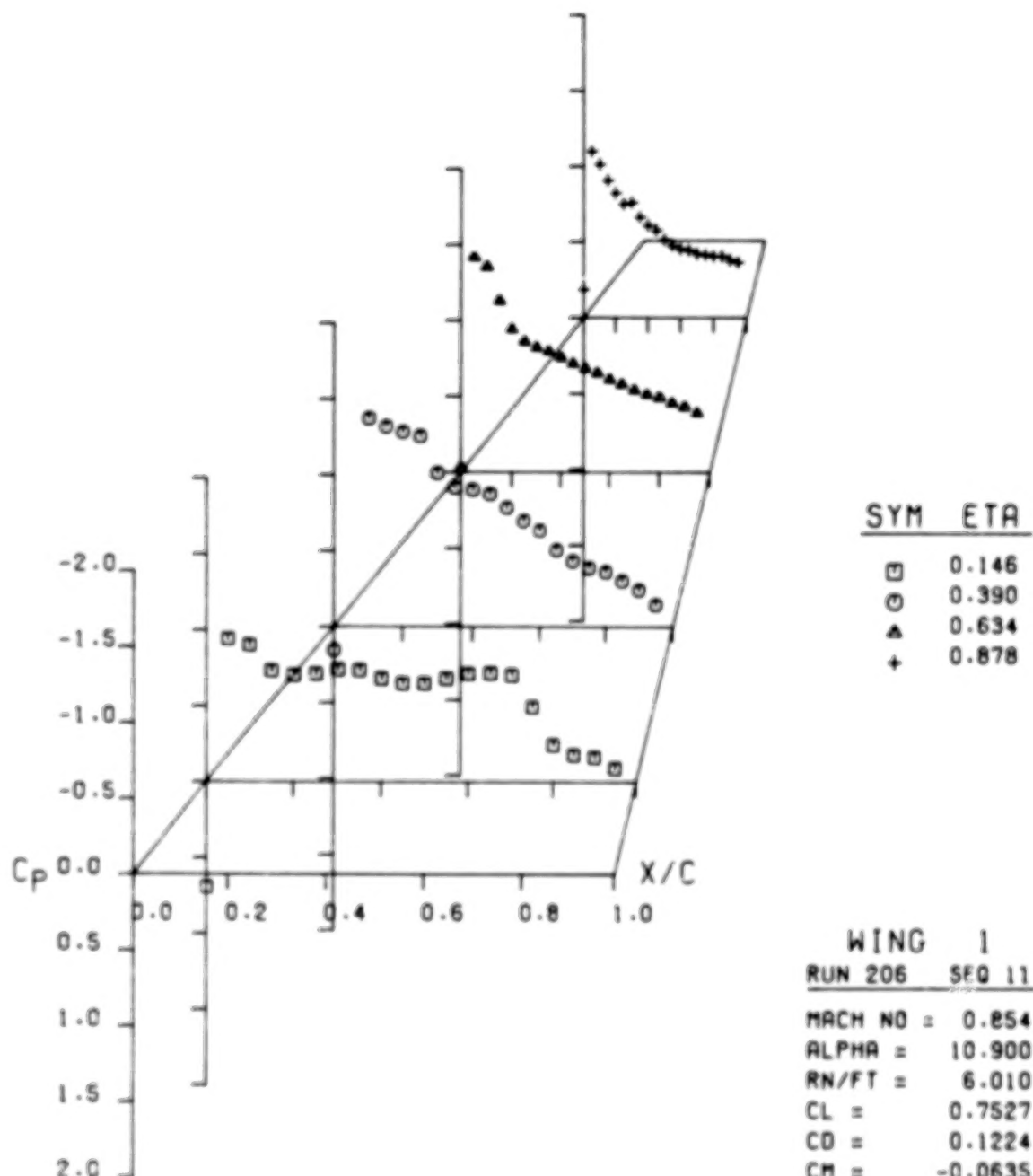
(D) ALPHA = 8.44

FIGURE 17.- WING NO. 1 UPPER SURFACE PRESSURES, MACH=0.85



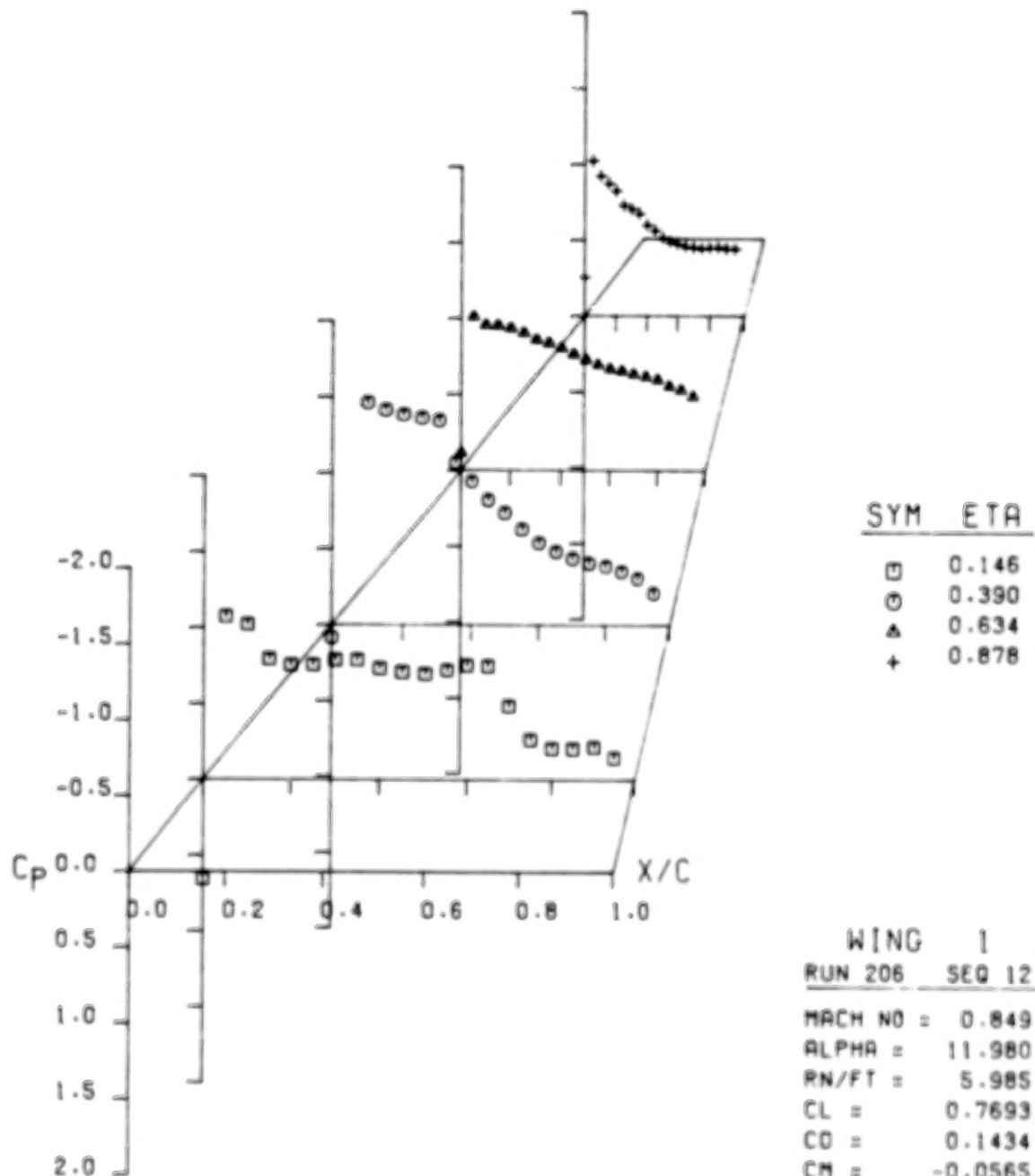
(E) ALPHA = 9.73

FIGURE 17.- WING NO. 1 UPPER SURFACE PRESSURES. MACH=0.85



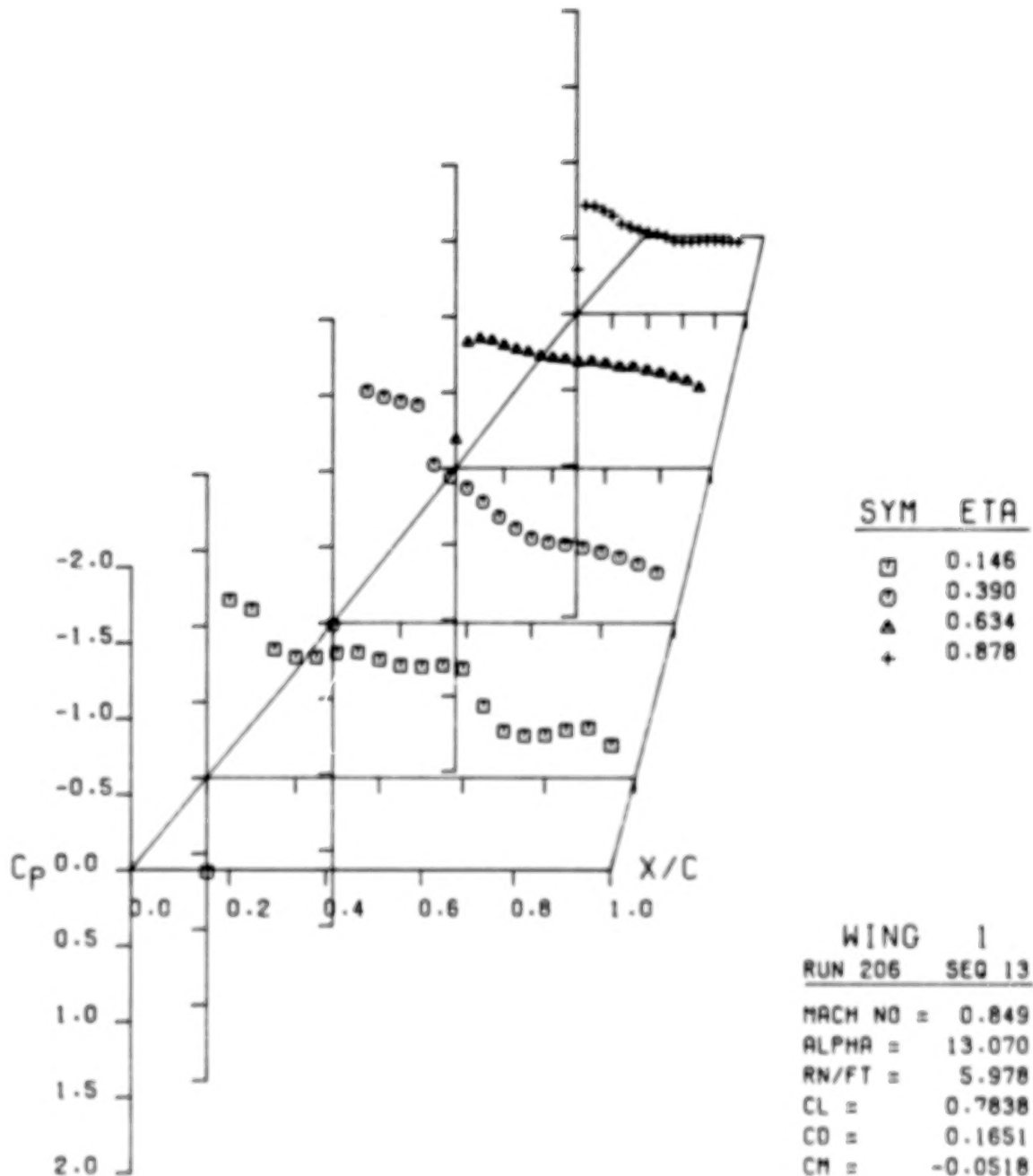
(F) ALPHA = 10.9

FIGURE 17.- WING NO. 1 UPPER SURFACE PRESSURES. MACH=0.85



(C) ALPHA = 11.98

FIGURE 17.- WING NO. 1 UPPER SURFACE PRESSURES, MACH=0.85



(H) ALPHA = 13.07

FIGURE 17.- WING NO. 1 UPPER SURFACE PRESSURES. MACH=0.85



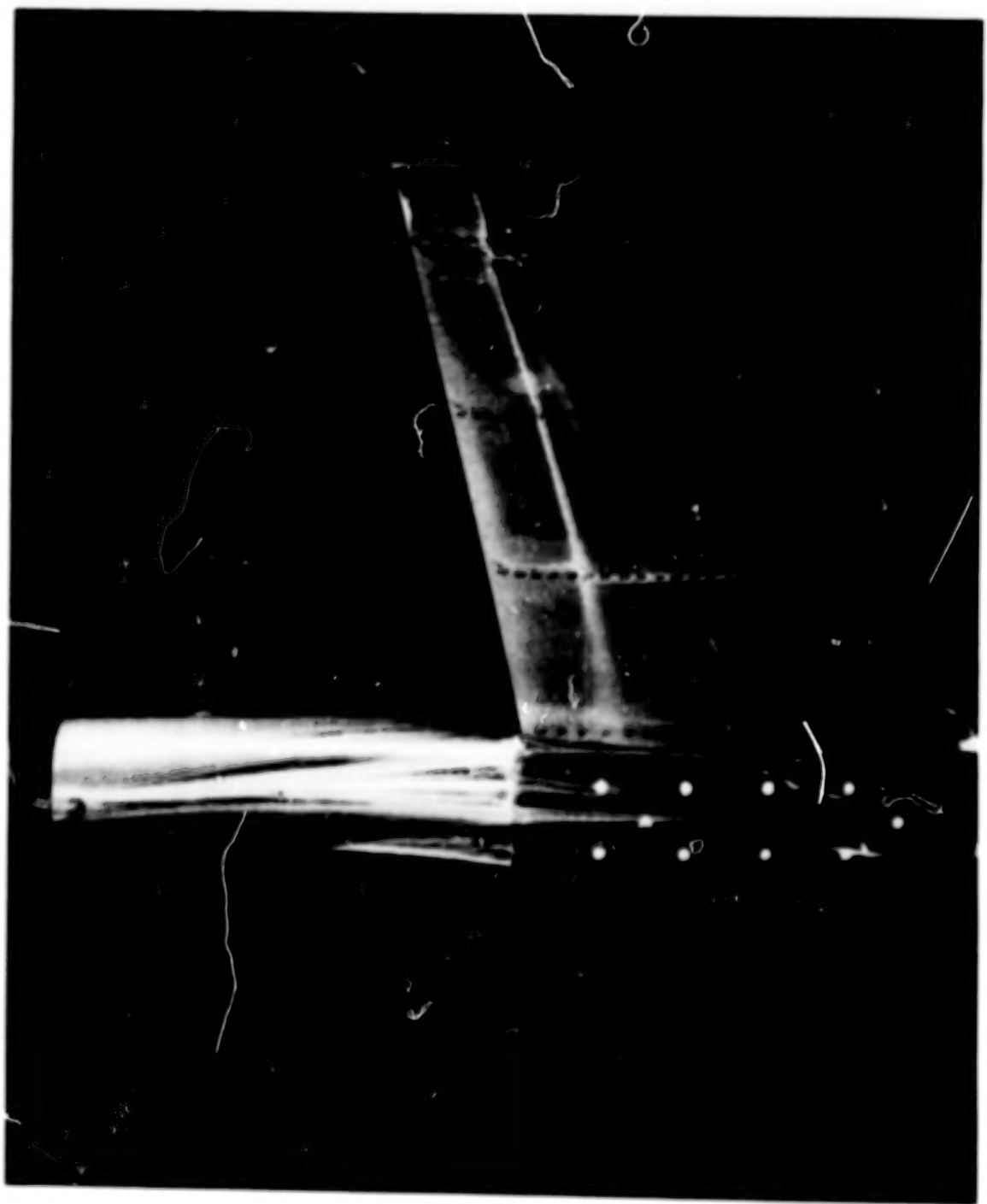
(A)  $\text{ALPHA} = 4.06$

FIGURE 18. - WING NO. 1 OIL FLOW PATTERNS, MACH = 0.85



(B)  $\text{ALPHA} = 5.53$

FIGURE 18.- WING NO. 1 OIL FLOW PATTERNS, MACH = 0.85



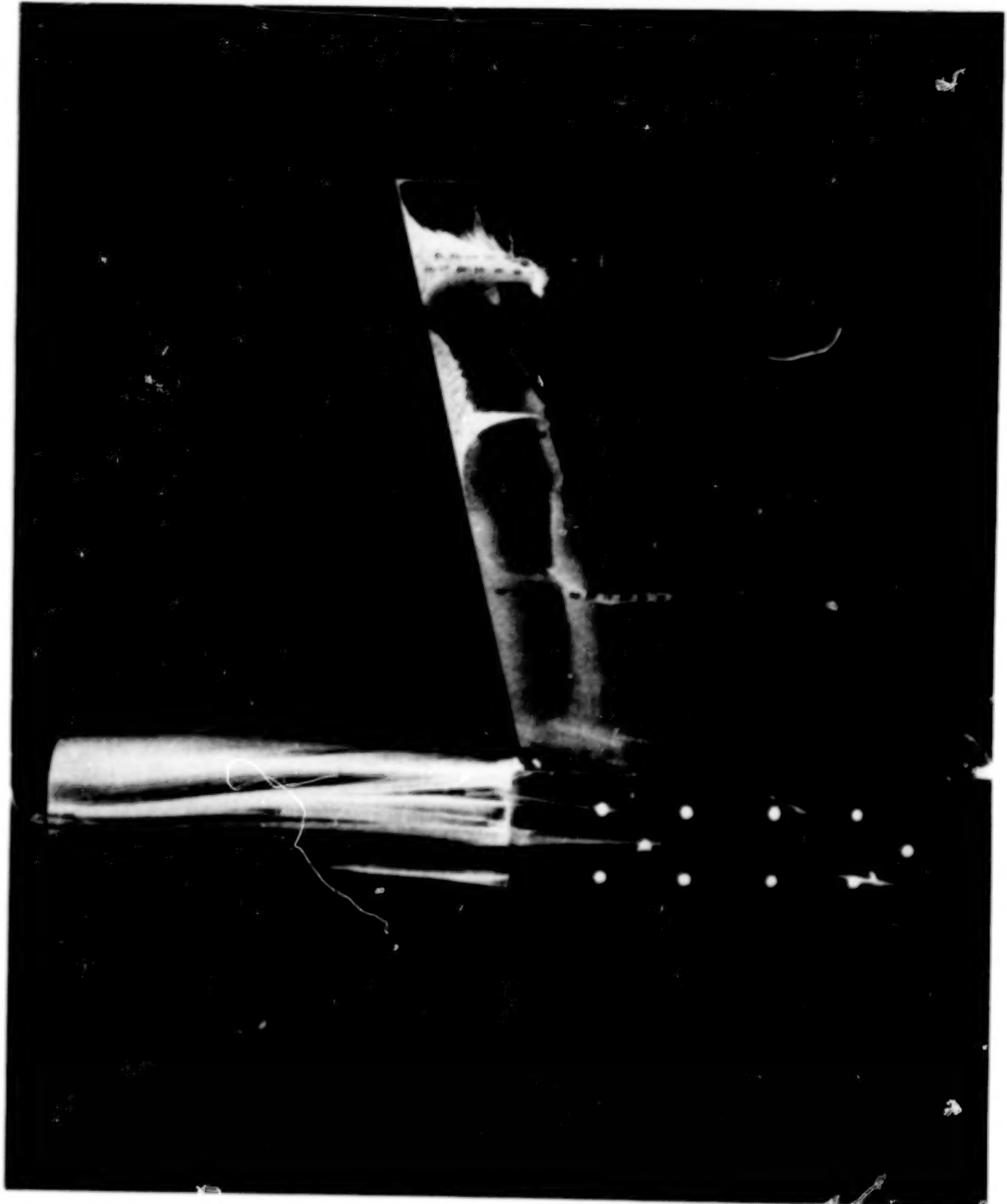
(C)  $\text{ALPHA} = 7.00$

FIGURE 18.- WING NO. 1 OIL FLOW PATTERNS, MACH = 0.85



(D)  $\text{ALPHA} = 8.37$

FIGURE 18.- WING NO. 1 OIL FLOW PATTERNS, MAC



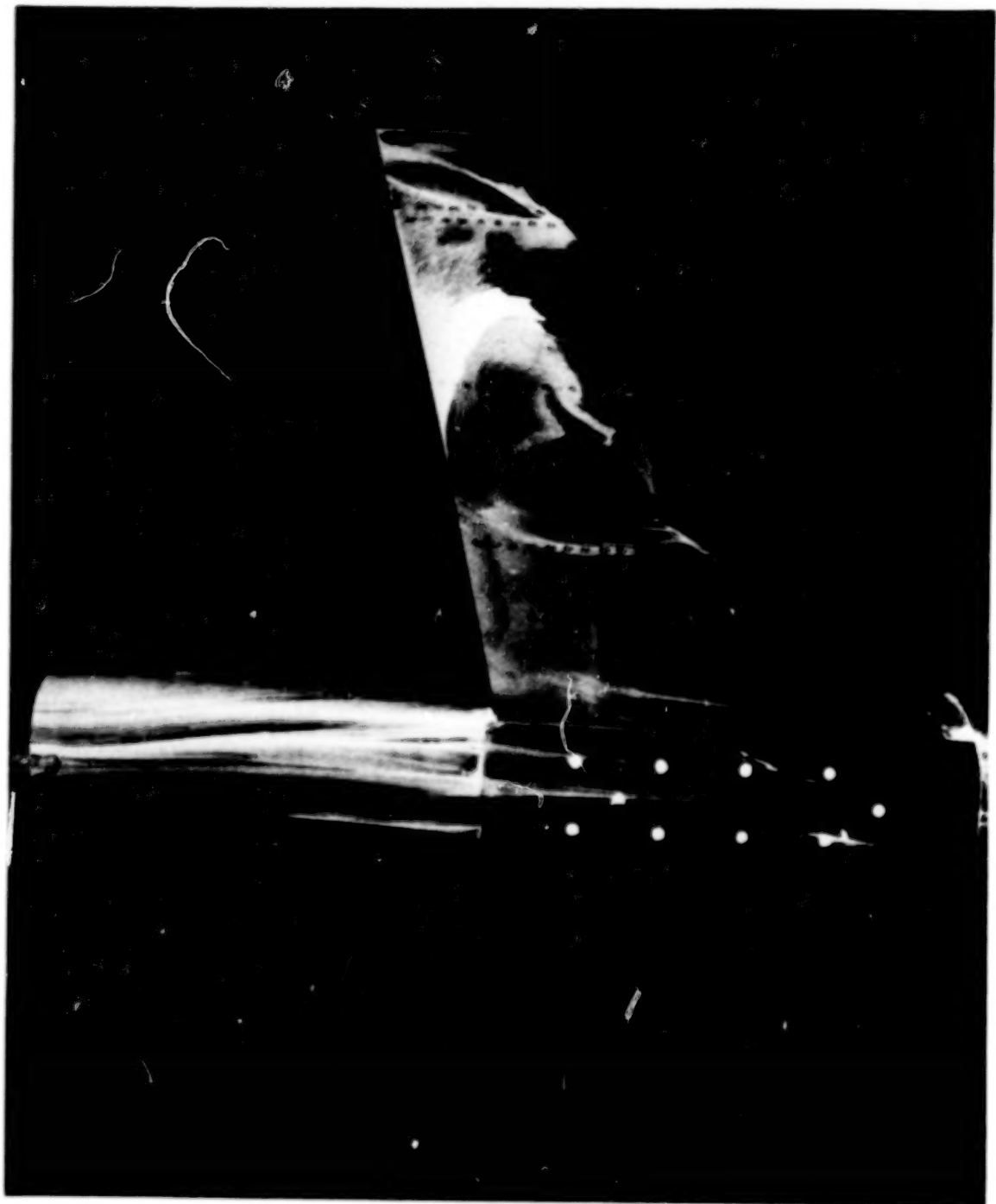
(E)  $\text{ALPHA} = 9.67$

FIGURE 18.- WING NO. 1 OIL FLOW PATTERNS, MACH = 0.85



(F)  $\text{ALPHA} = 10.83$

FIGURE 18.- WING NO. 1 OIL FLOW PATTERNS, MACH = 0.85



(G)  $\text{ALPHA} = 11.88$

FIGURE 18.- WING NO. 1 OIL FLOW PATTERNS, MACH = 0.85

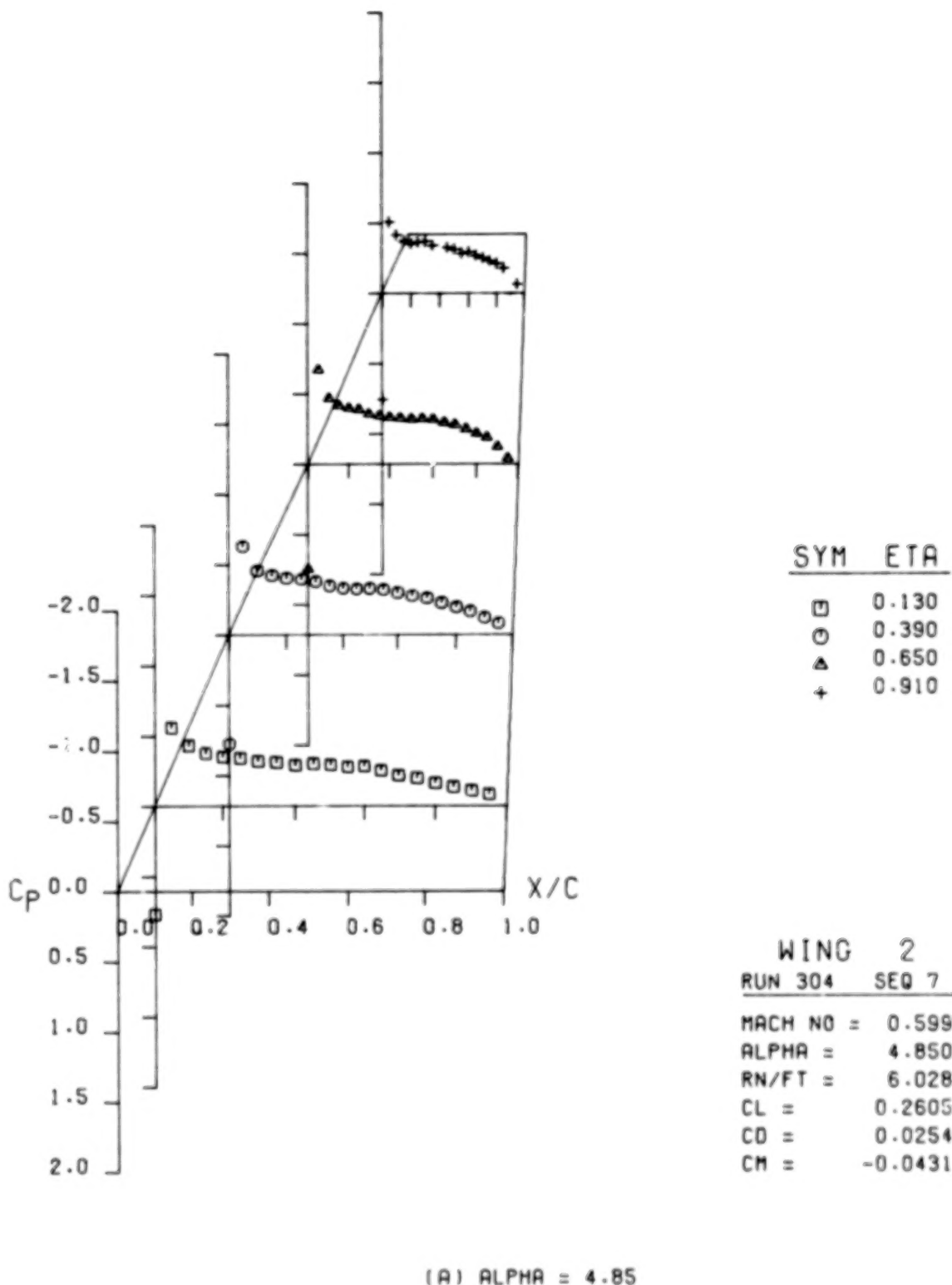
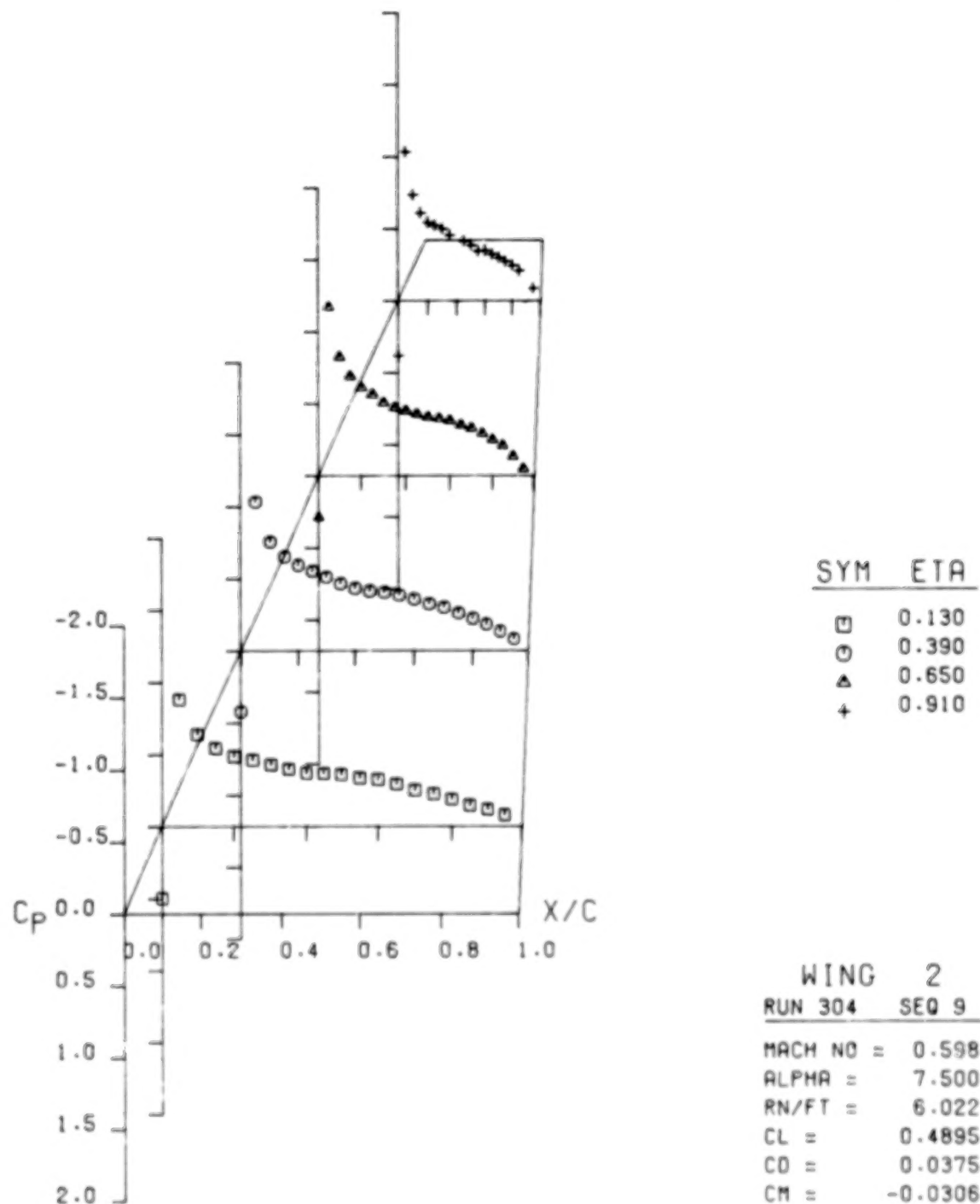


FIGURE 19.- WING NO. 2 UPPER SURFACE PRESSURES. MACH=0.599

NASA AMES TEST 231-1-11



(B) ALPHA = 7.50

FIGURE 19.- WING NO. 2 UPPER SURFACE PRESSURES. MACH=0.598

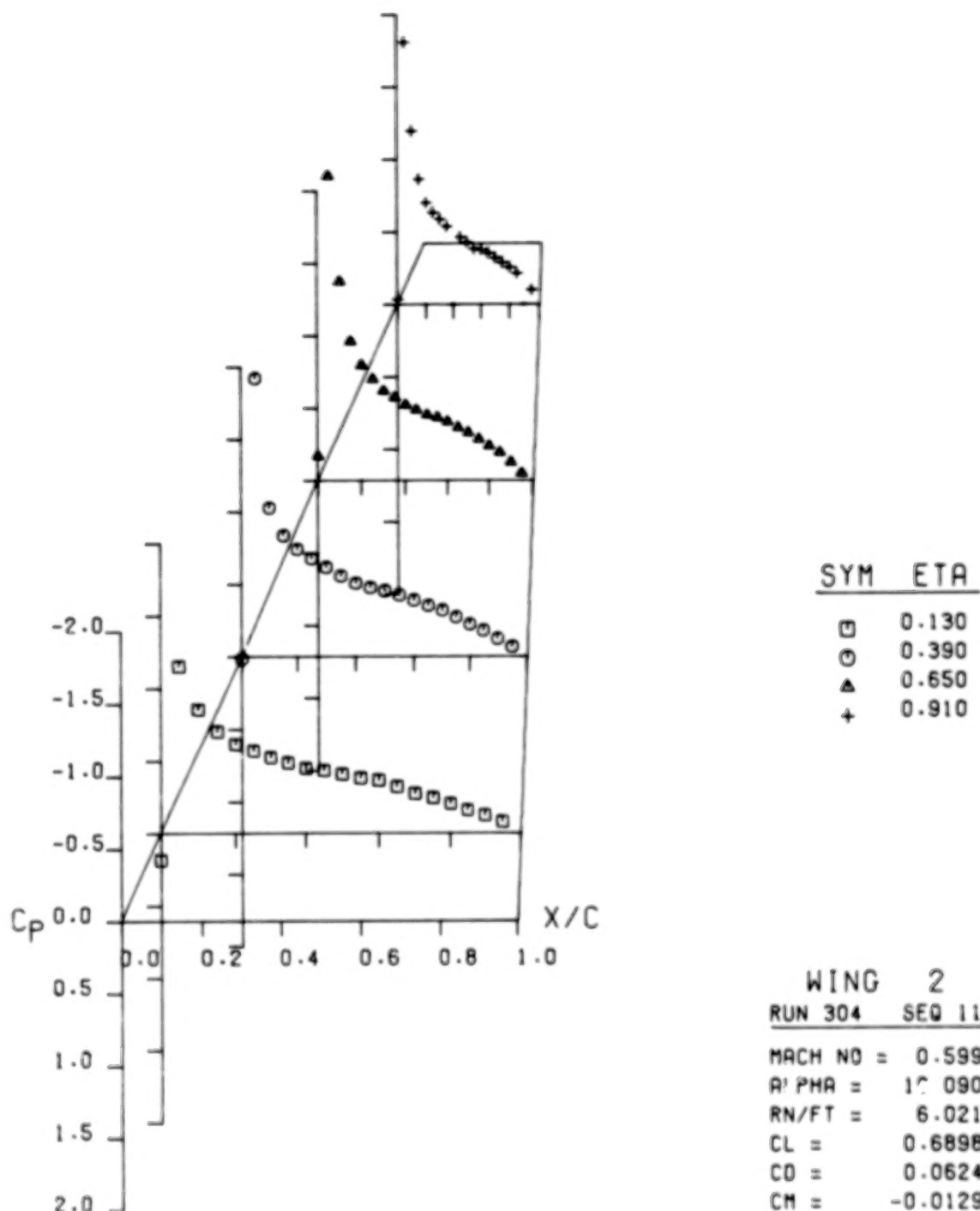
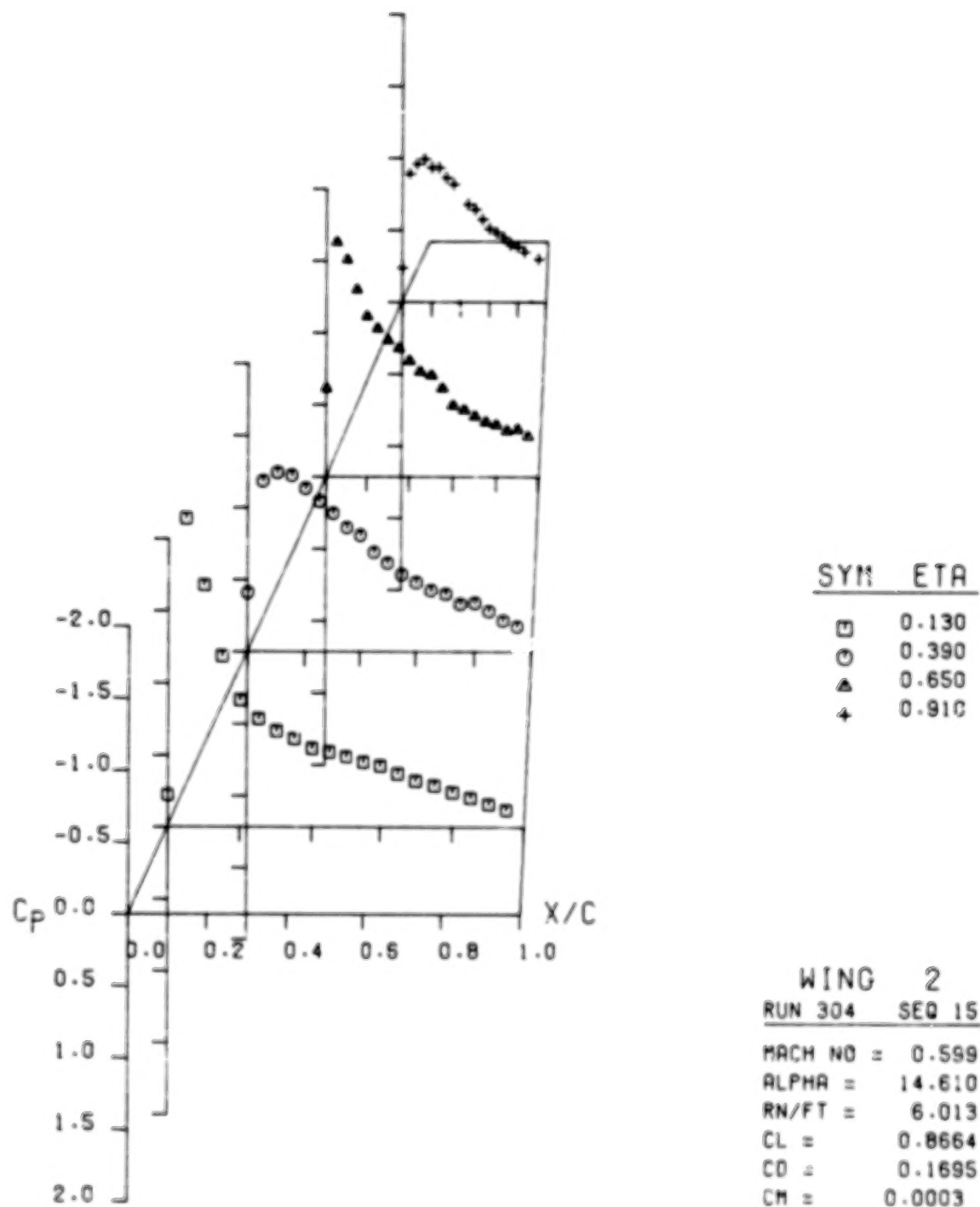
(C)  $\alpha$  = 10.09

FIGURE 19.- WING NO. 2 UPPER SURFACE PRESSURES, MACH=0.599



(D) ALPHA = 14.61

FIGURE 19.- WING NO. 2 UPPER SURFACE PRESSURES, MACH=0.599

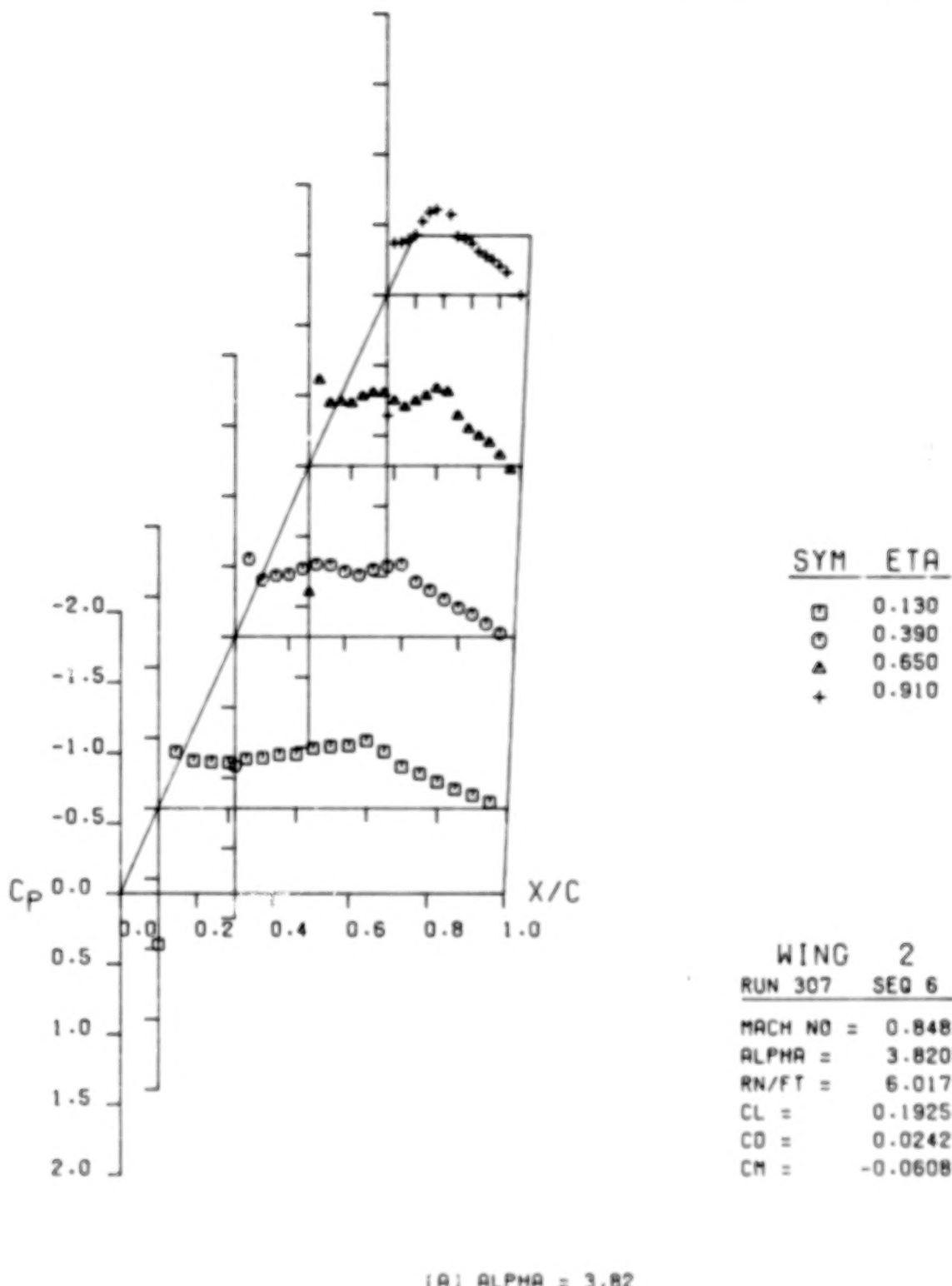
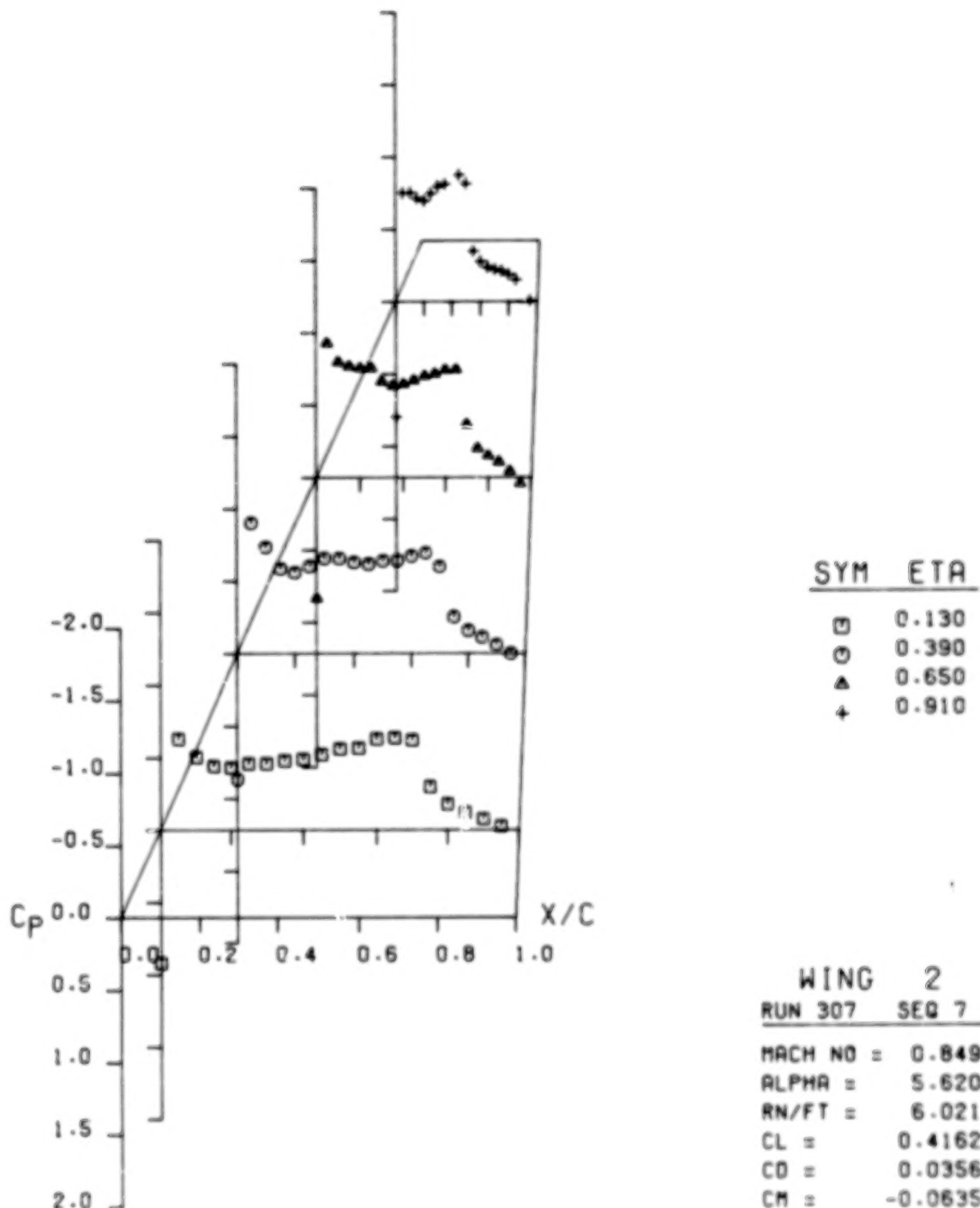
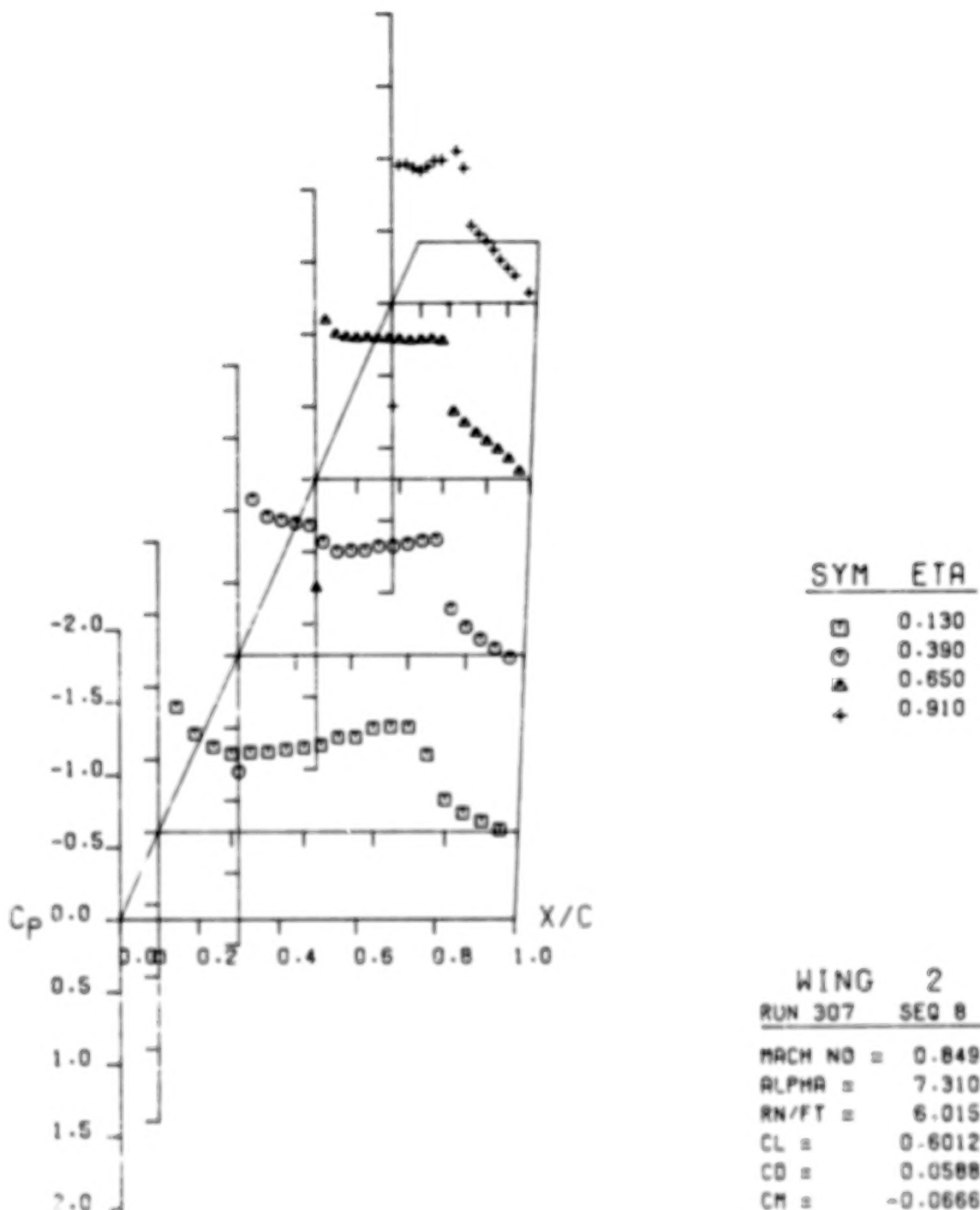


FIGURE 20.- WING NO. 2 UPPER SURFACE PRESSURES, MACH=0.85



(B) ALPHA = 5.62

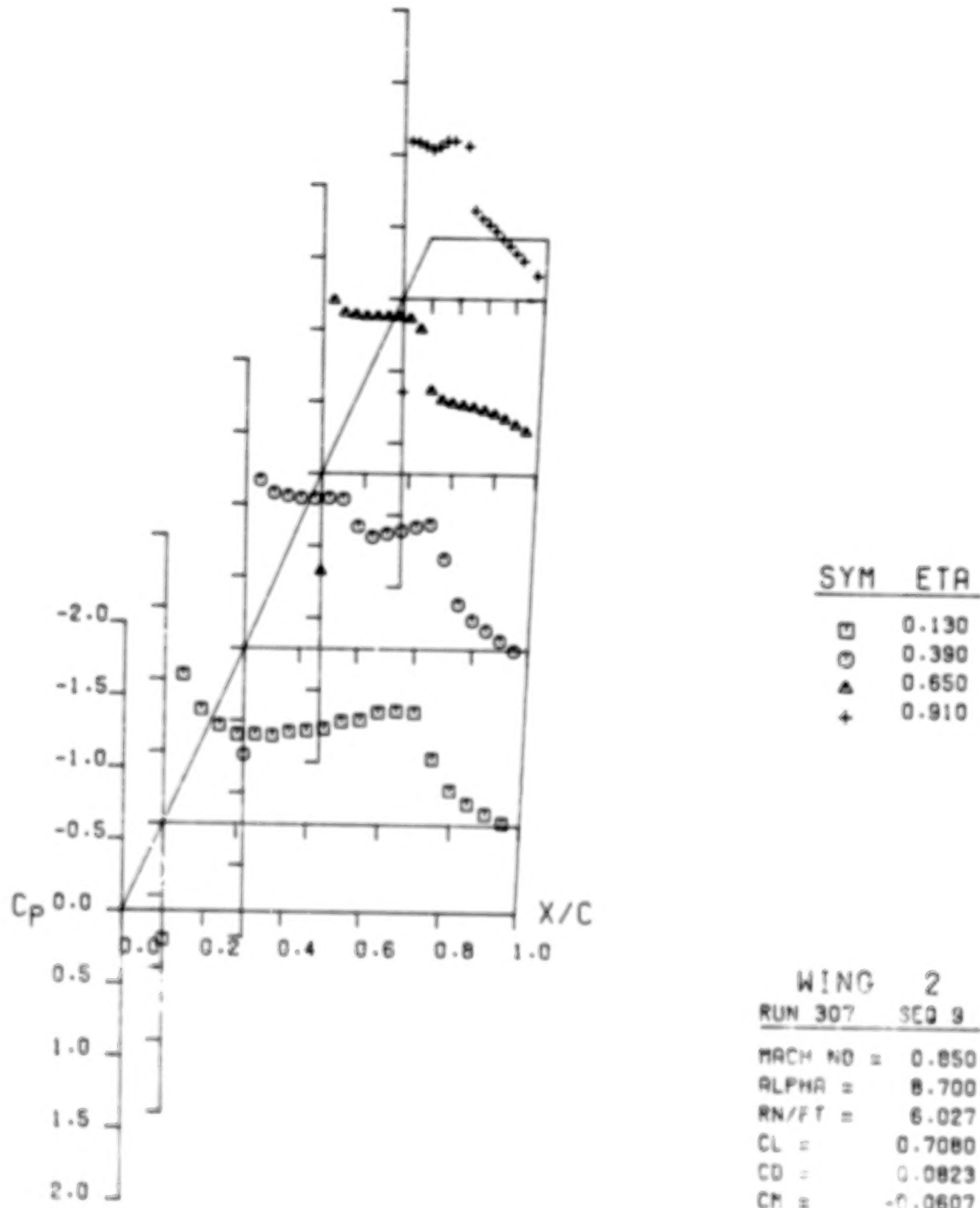
FIGURE 20.- WING NO. 2 UPPER SURFACE PRESSURES, MACH=0.85



(C) ALPHA = 7.31

FIGURE 20.- WING NO. 2 UPPER SURFACE PRESSURES. MACH=0.85

NASA AMES TEST 231-1-11



(D) ALPHA = 8.70

FIGURE 20.- WING NO. 2 UPPER SURFACE PRESSURES. MACH=0.85

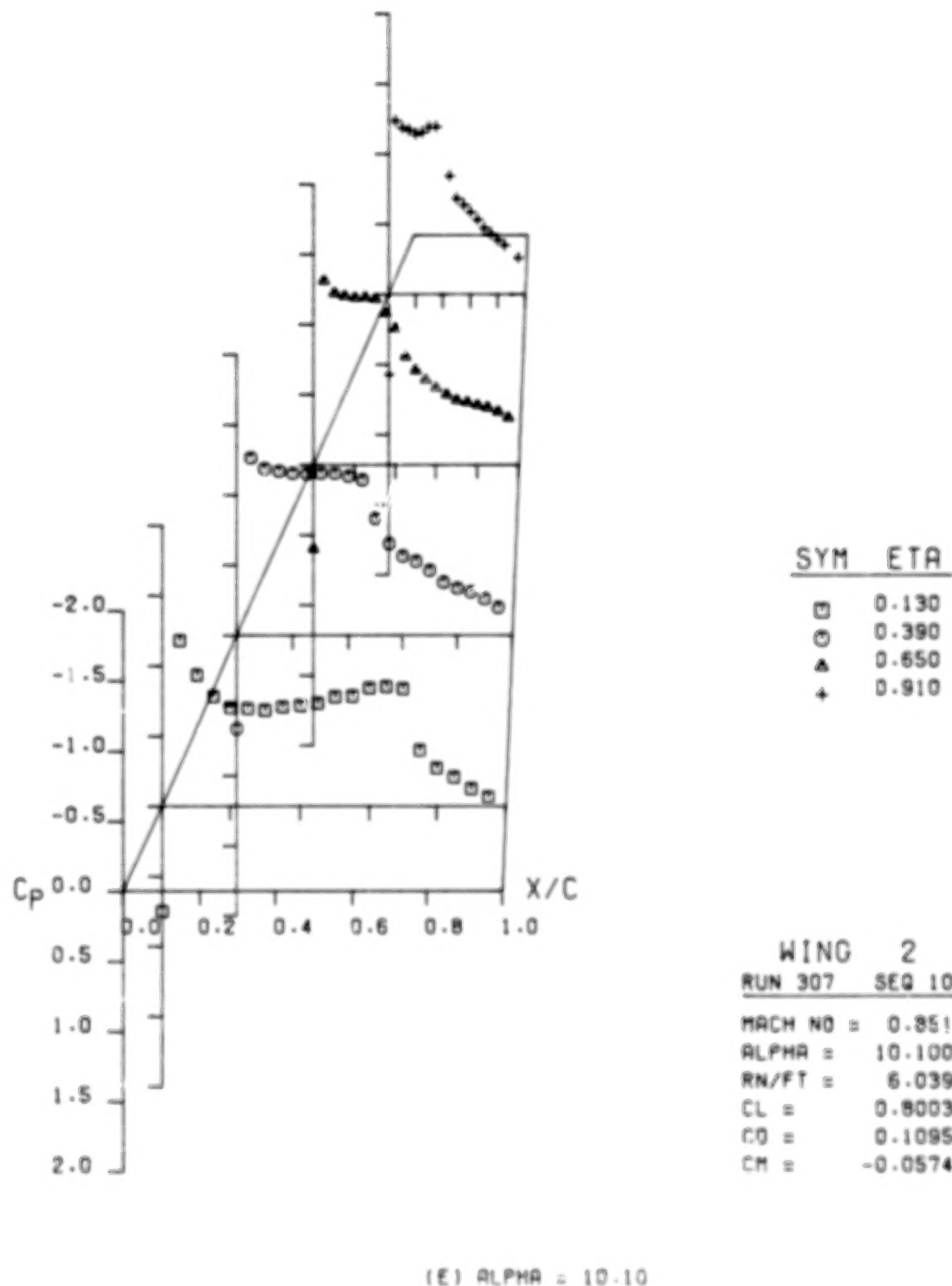
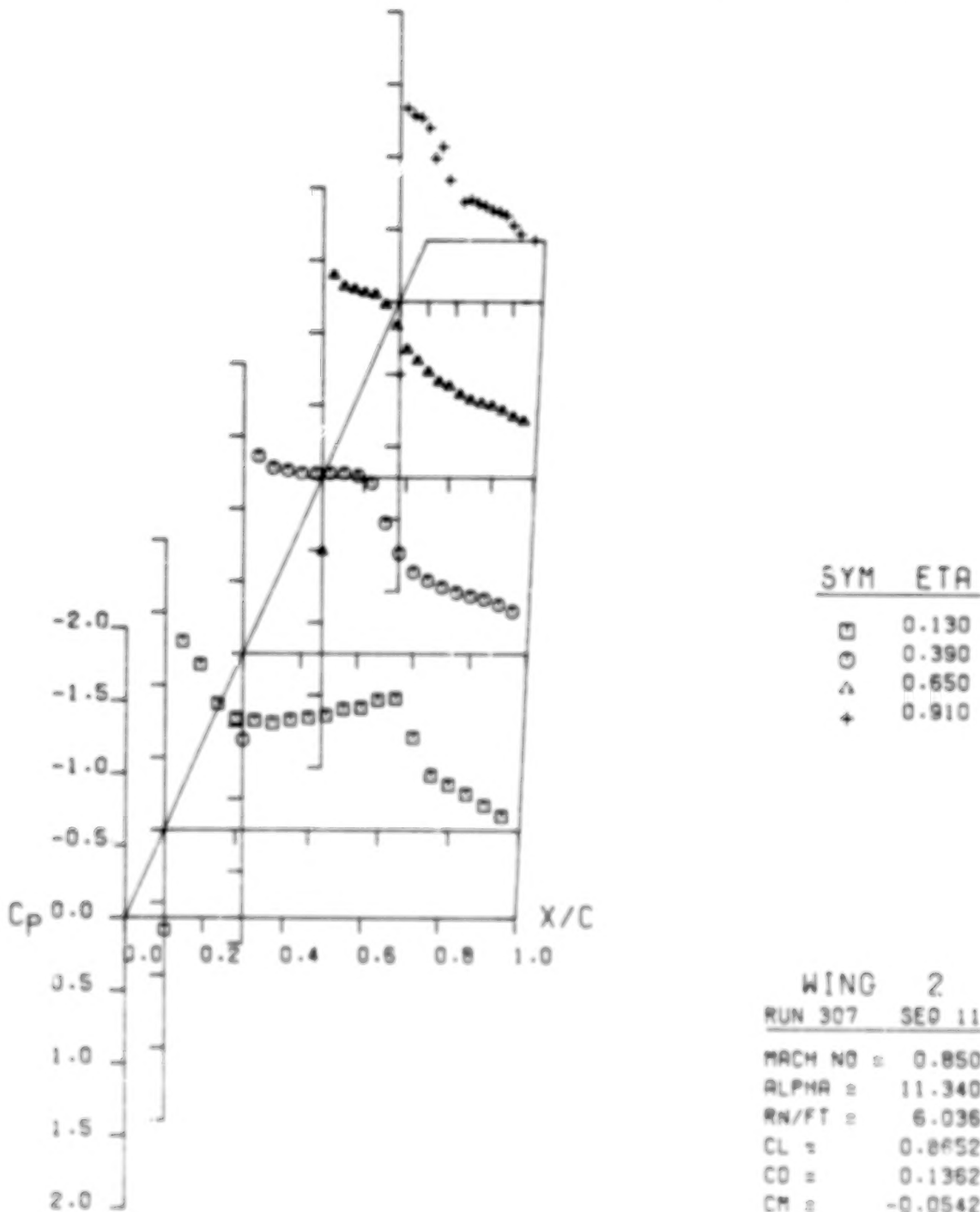


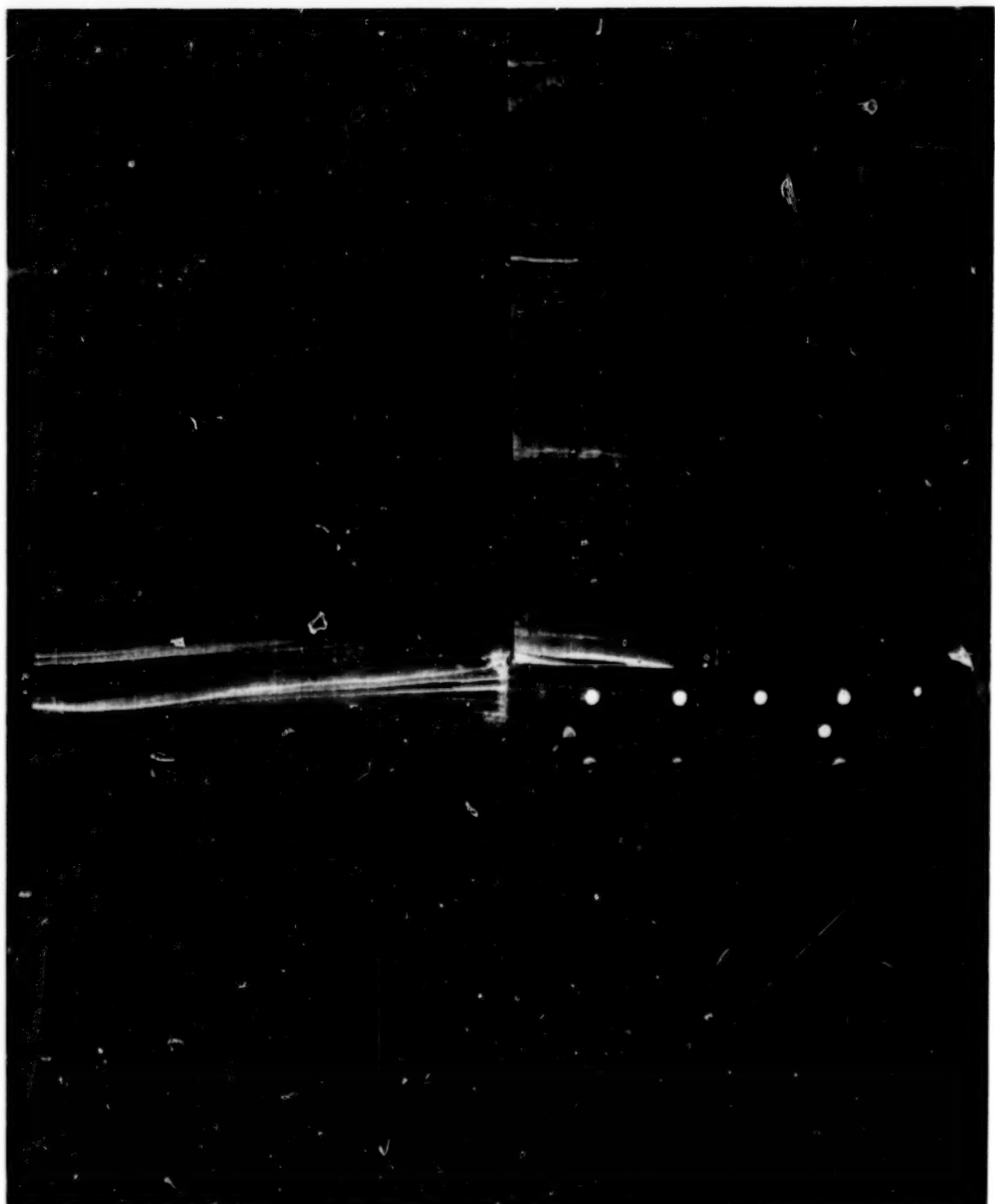
FIGURE 20.- WING NO. 2 UPPER SURFACE PRESSURES, MACH=0.85

NASA AMES TEST 231-1-11



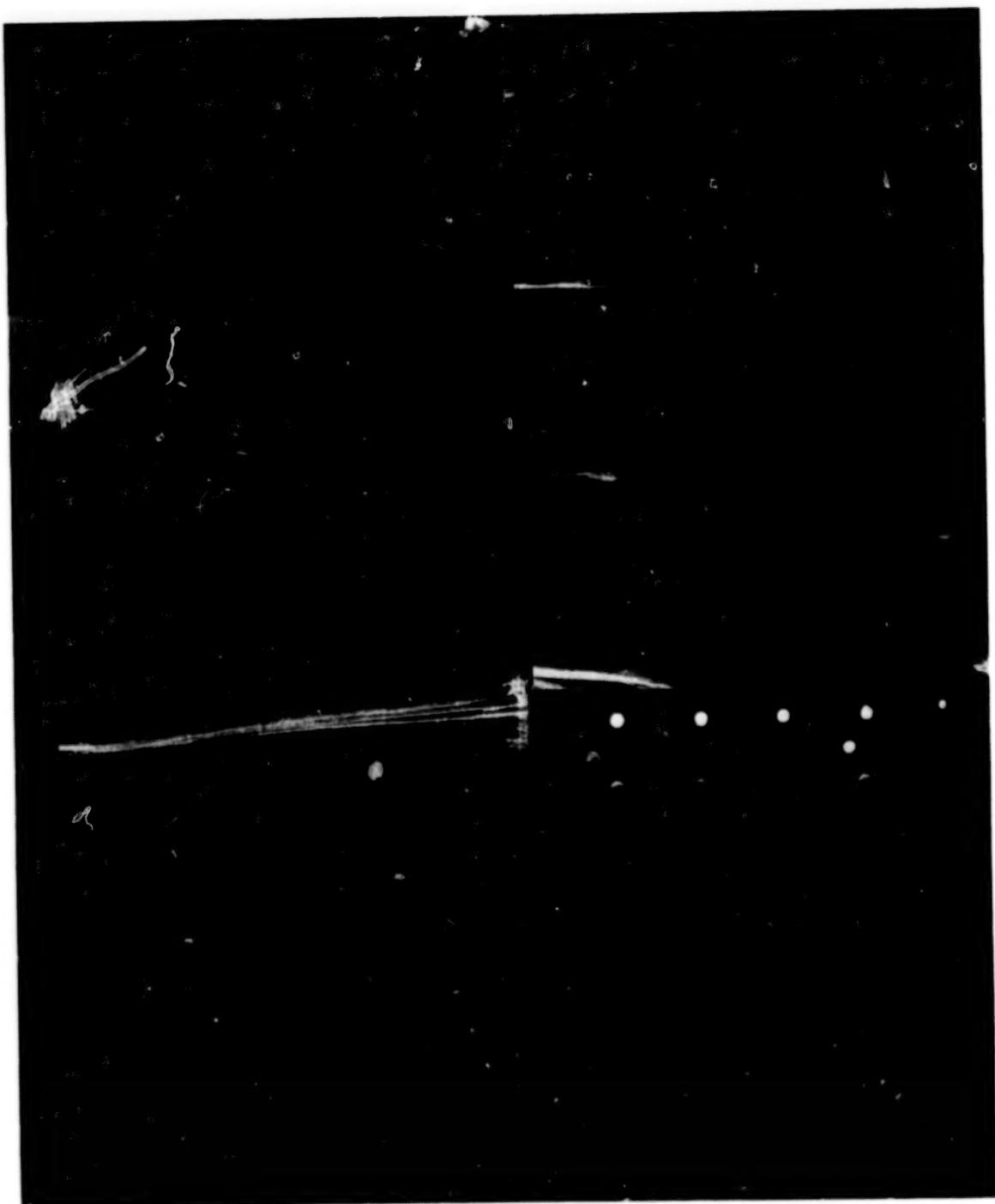
(F) ALPHA = 11.34

FIGURE 20.- WING NO. 2 UPPER SURFACE PRESSURES, MACH=0.85



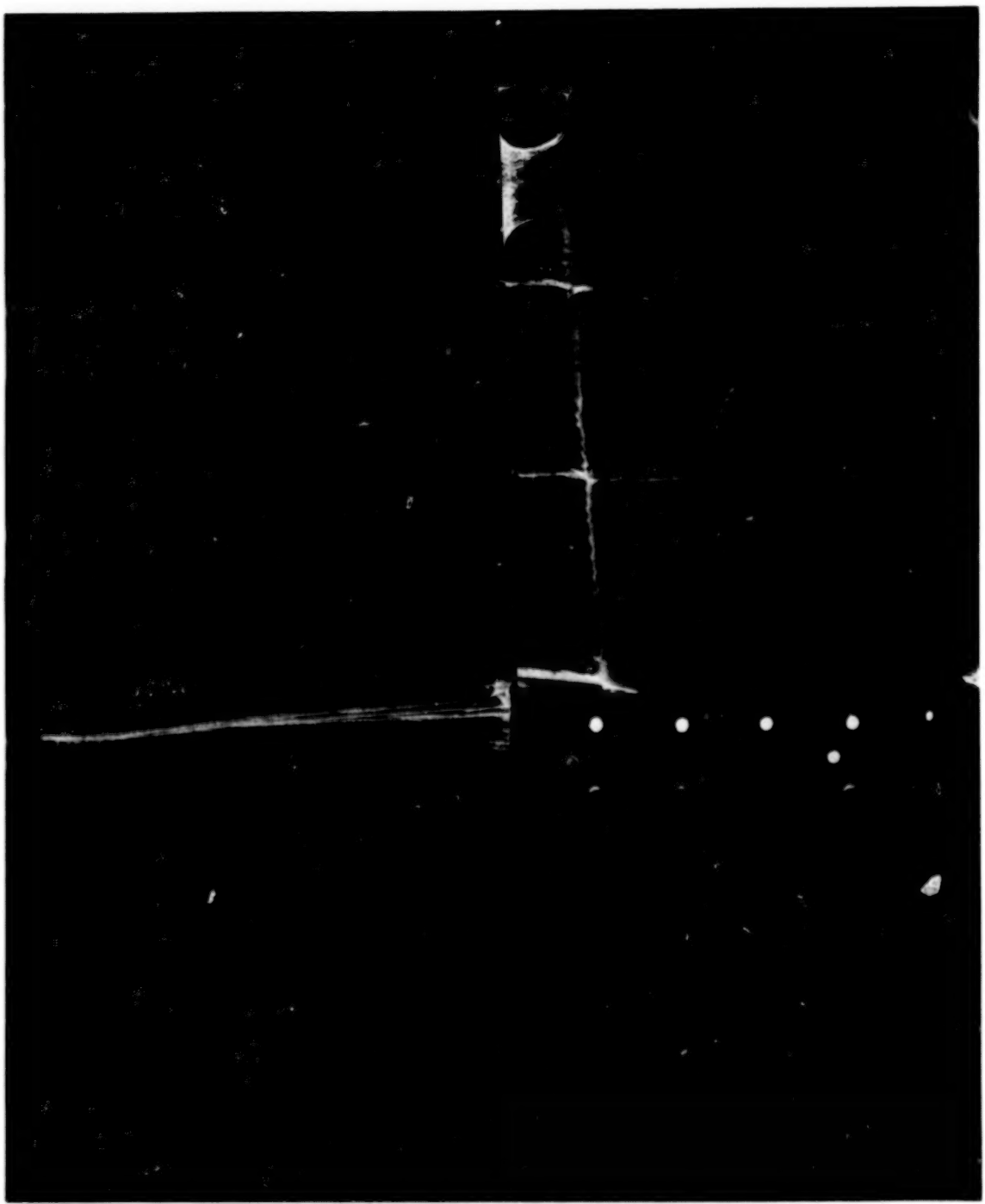
(A)  $\text{ALPHA} = 3.78$

FIGURE 21.- WING NO. 2 OIL FLOW PATTERNS, MACH = 0.85



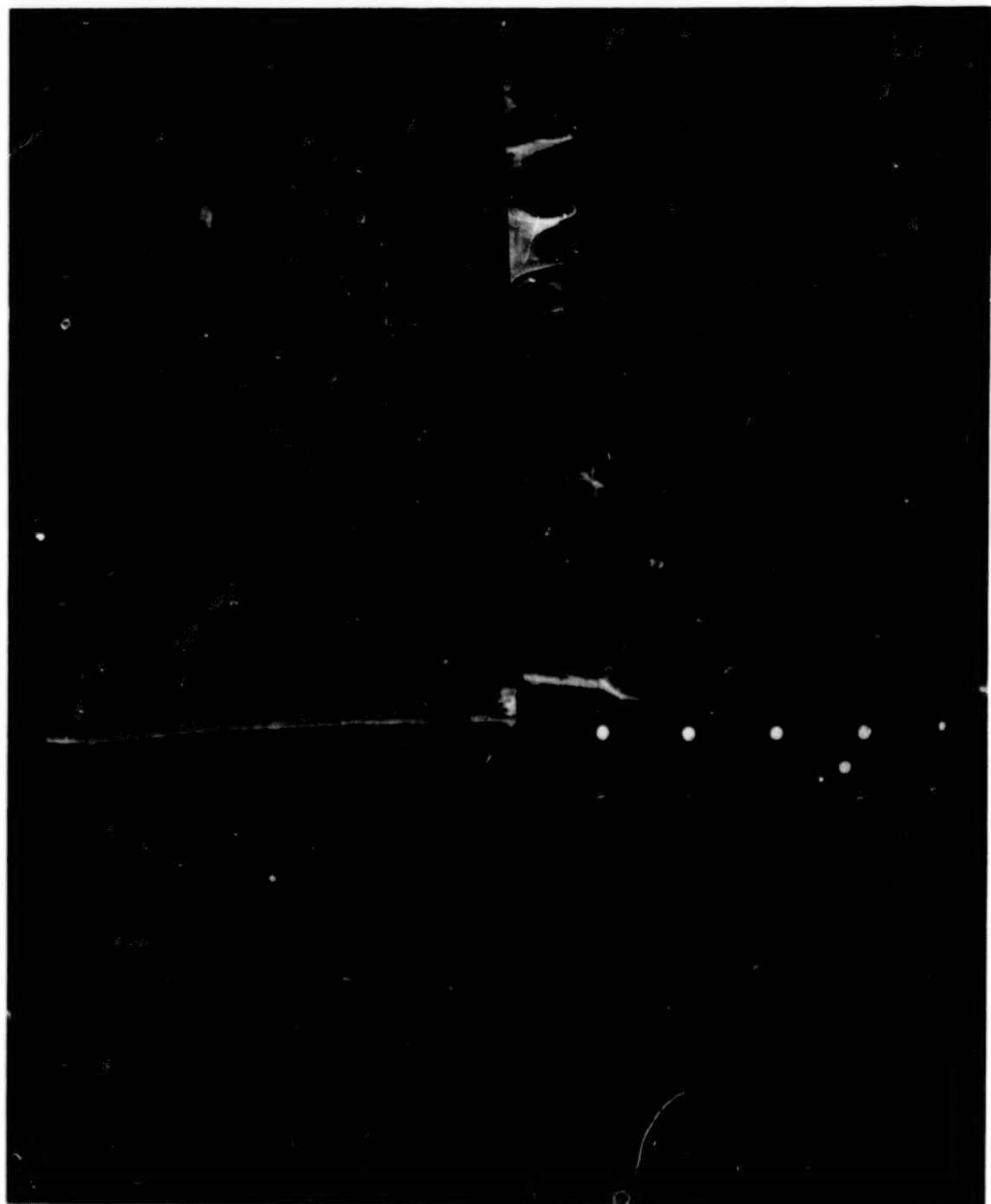
(B) ALPHA = 5.59

FIGURE 21.- WING NO. 2 OIL FLOW PATTERNS, MACH = 0.85



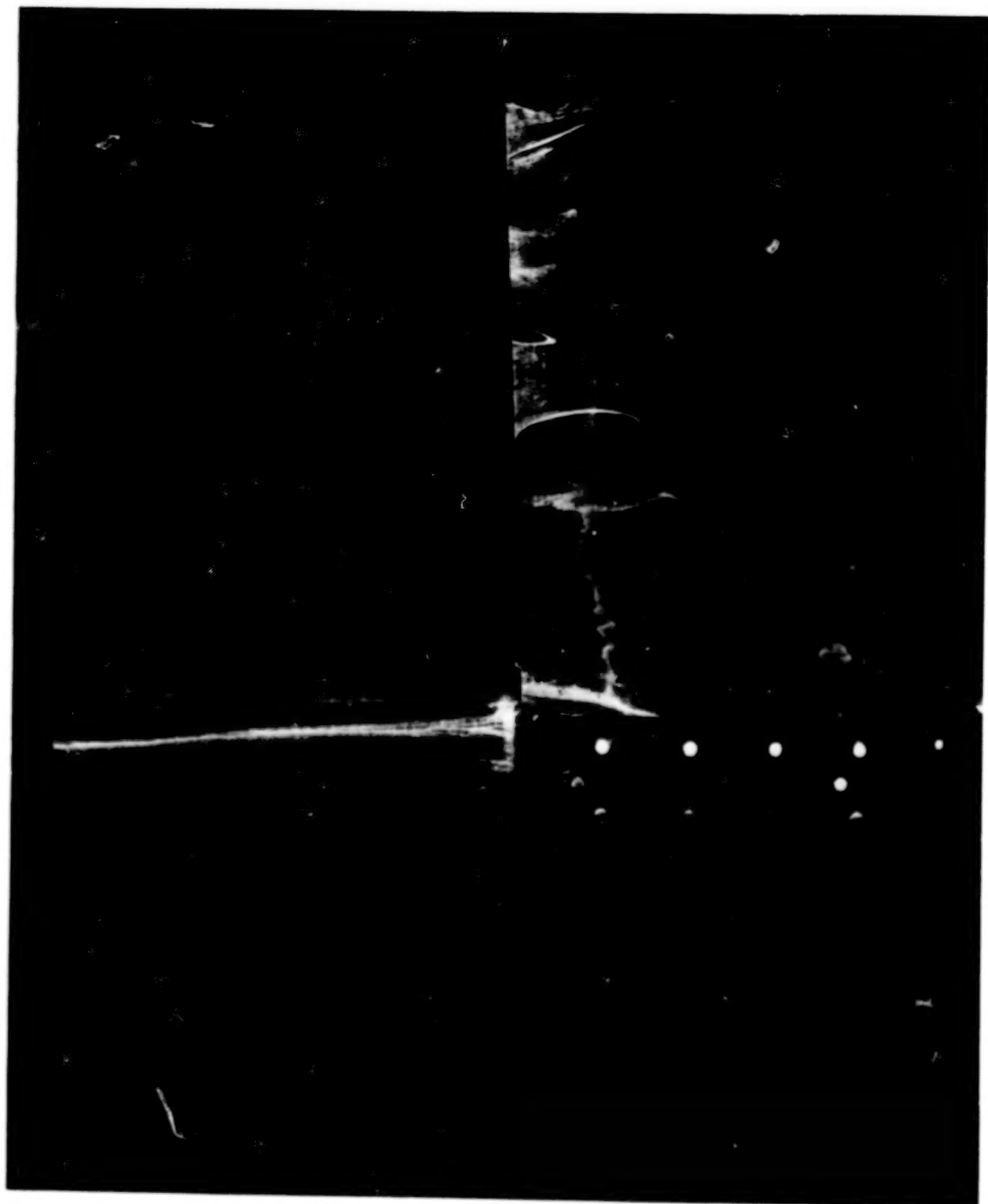
(C)  $\text{ALPHA} = 7.27$

FIGURE 21.- WING NO. 2 OIL FLOW PATTERNS, MACH = 0.85



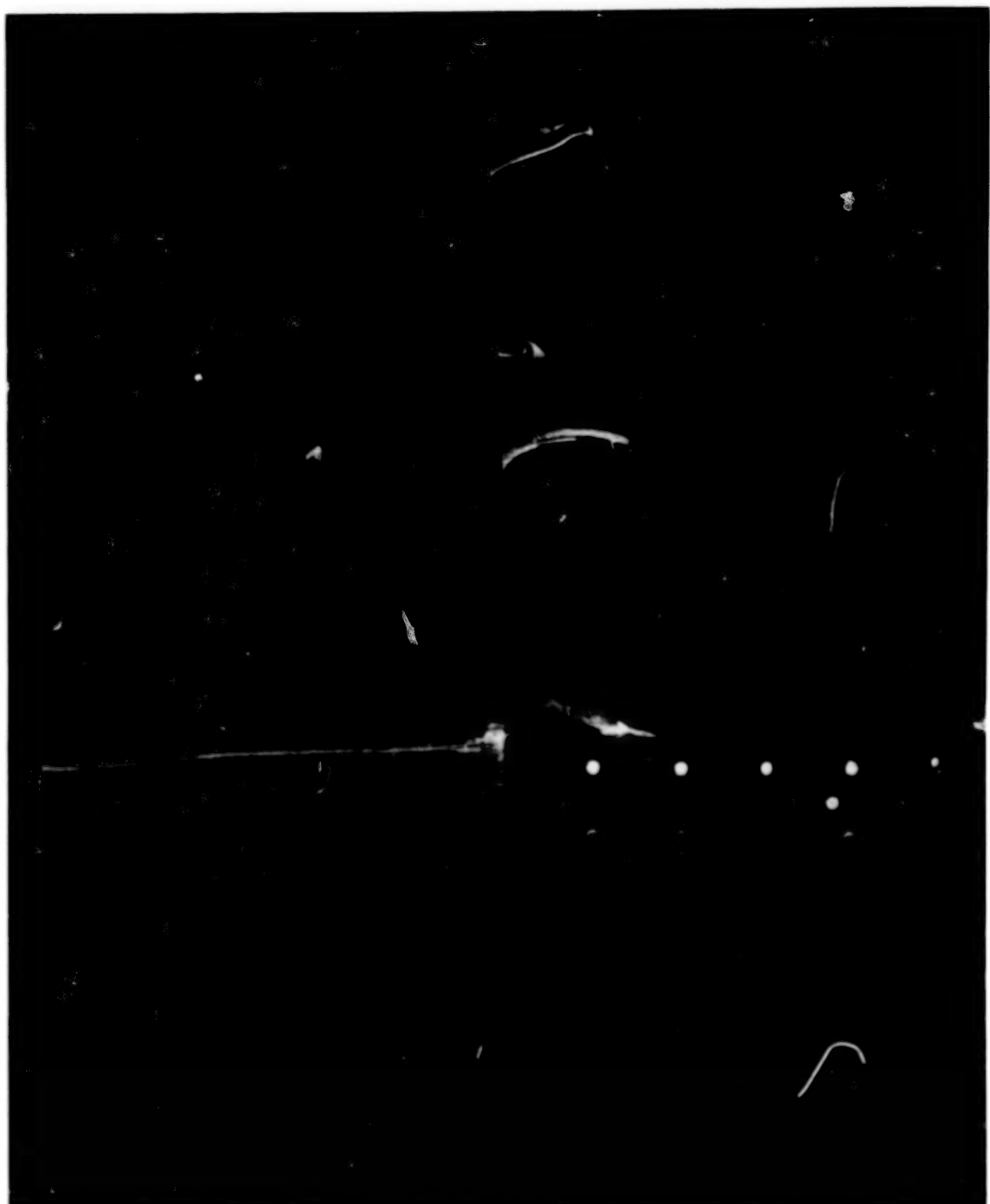
(D) ALPHA = 8.74

FIGURE 21.- WING NO. 2 OIL FLOW PATTERNS, MACH = 0.85



(E)  $\text{ALPHA} = 10.09$

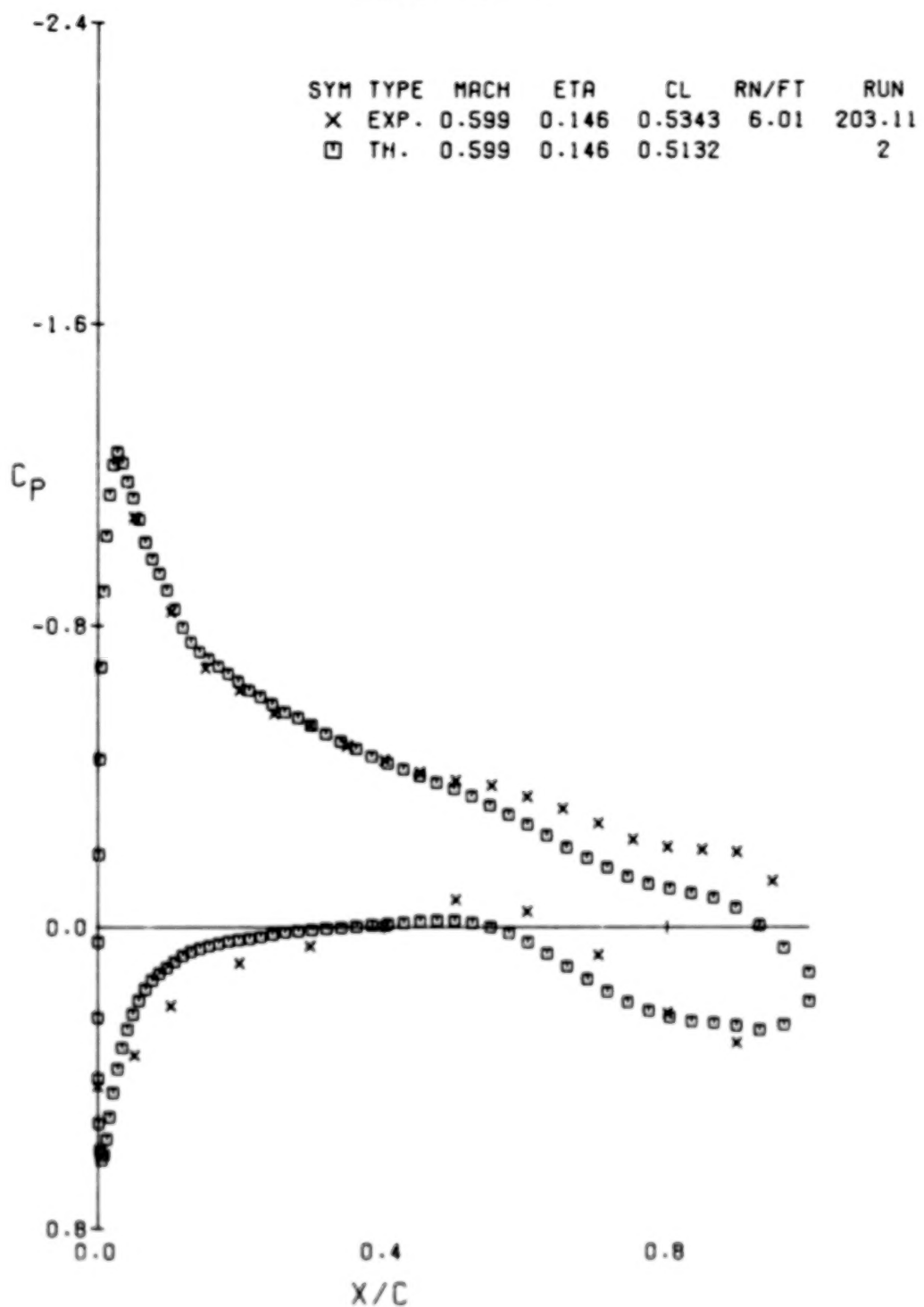
FIGURE 21.- WING NO. 2 OIL FLOW PATTERNS, MACH = 0.85



(F)  $\text{ALPHA} = 11.36$

FIGURE 21.- WING NO. 2 OIL FLOW PATTERNS, MACH = 0.85

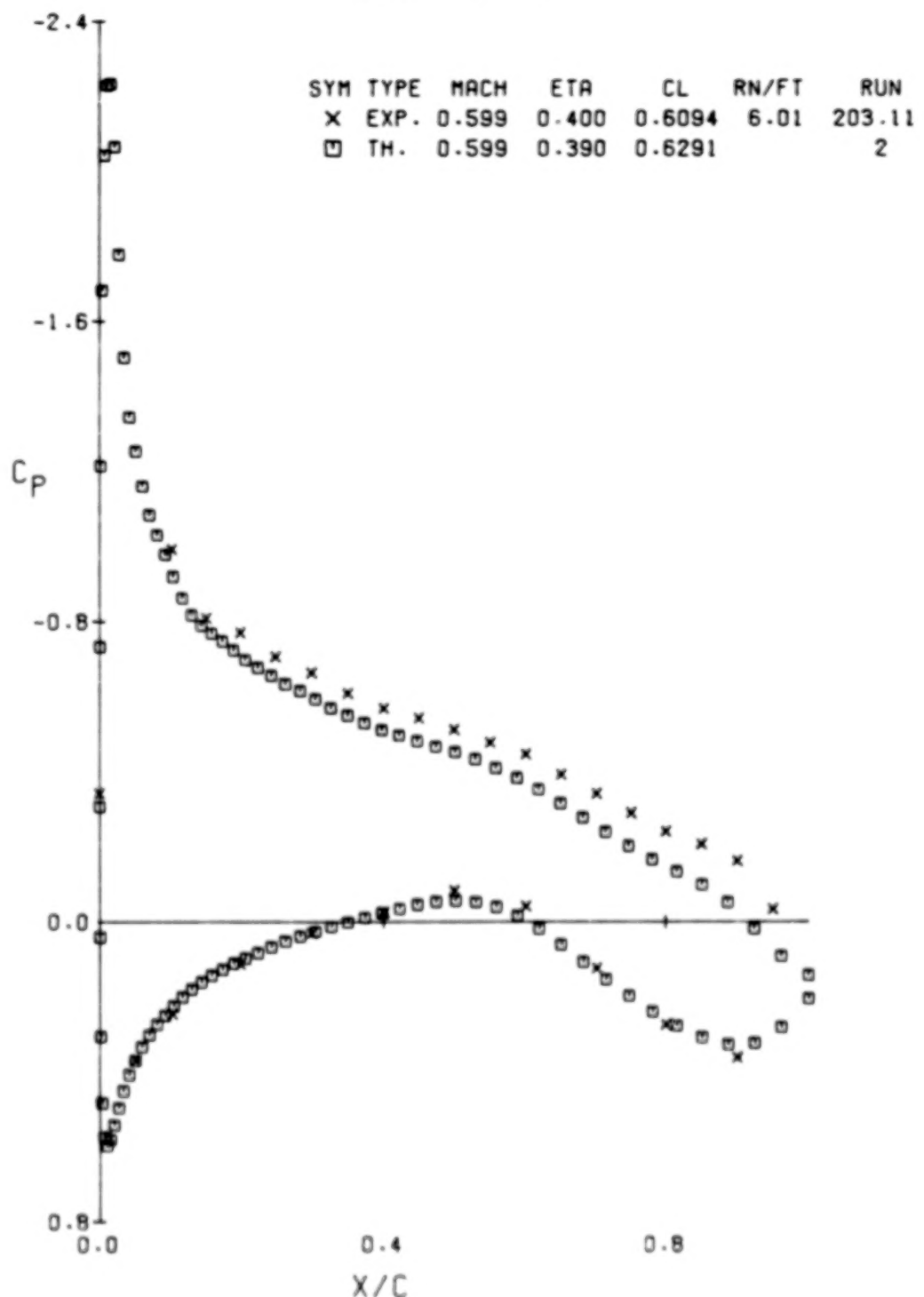
WING NO. 1



(A) ETA = .146

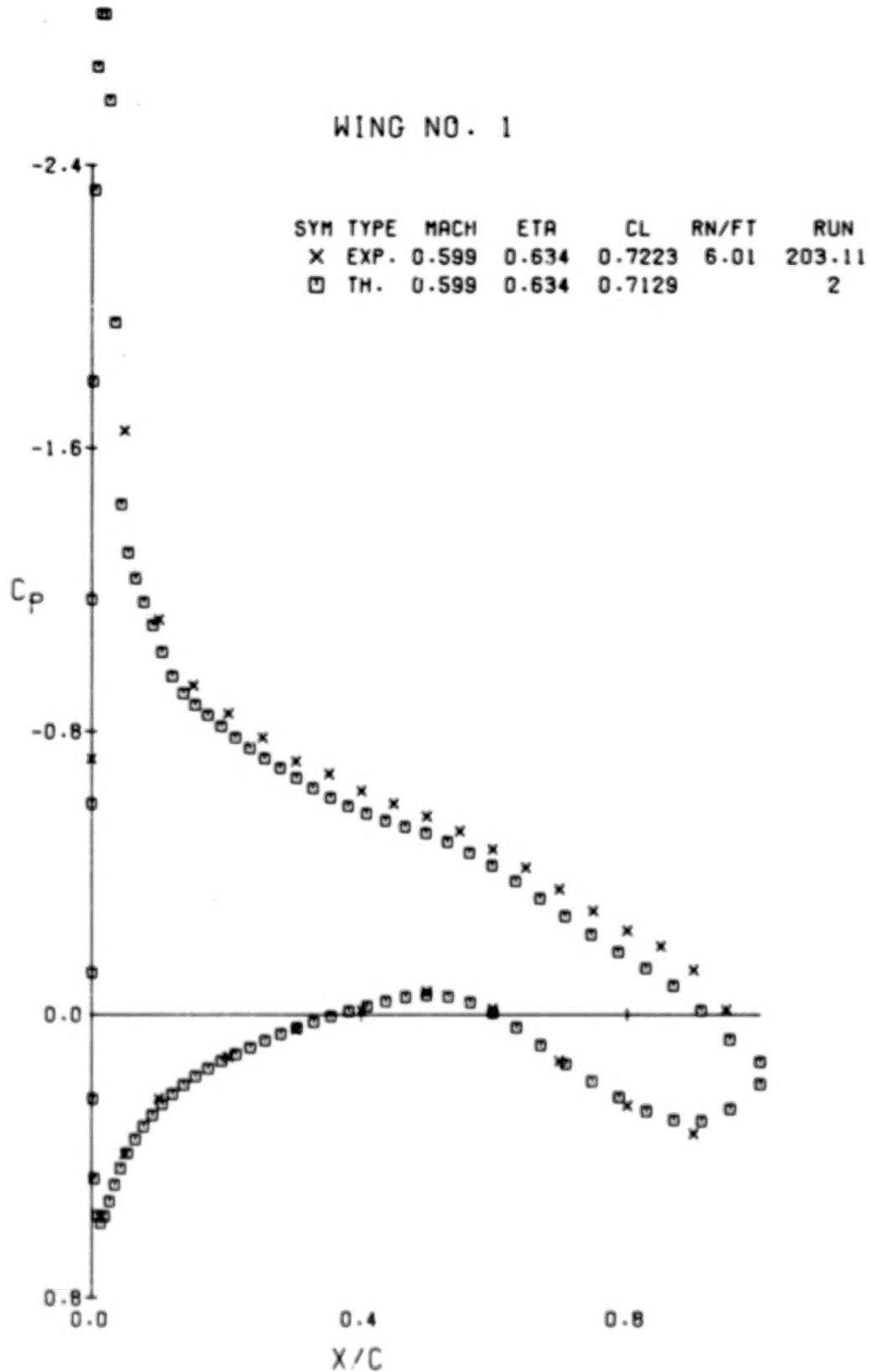
FIGURE 22.- WING NO. 1 COMPARISON OF THEORY WITH EXPERIMENT

WING NO. 1



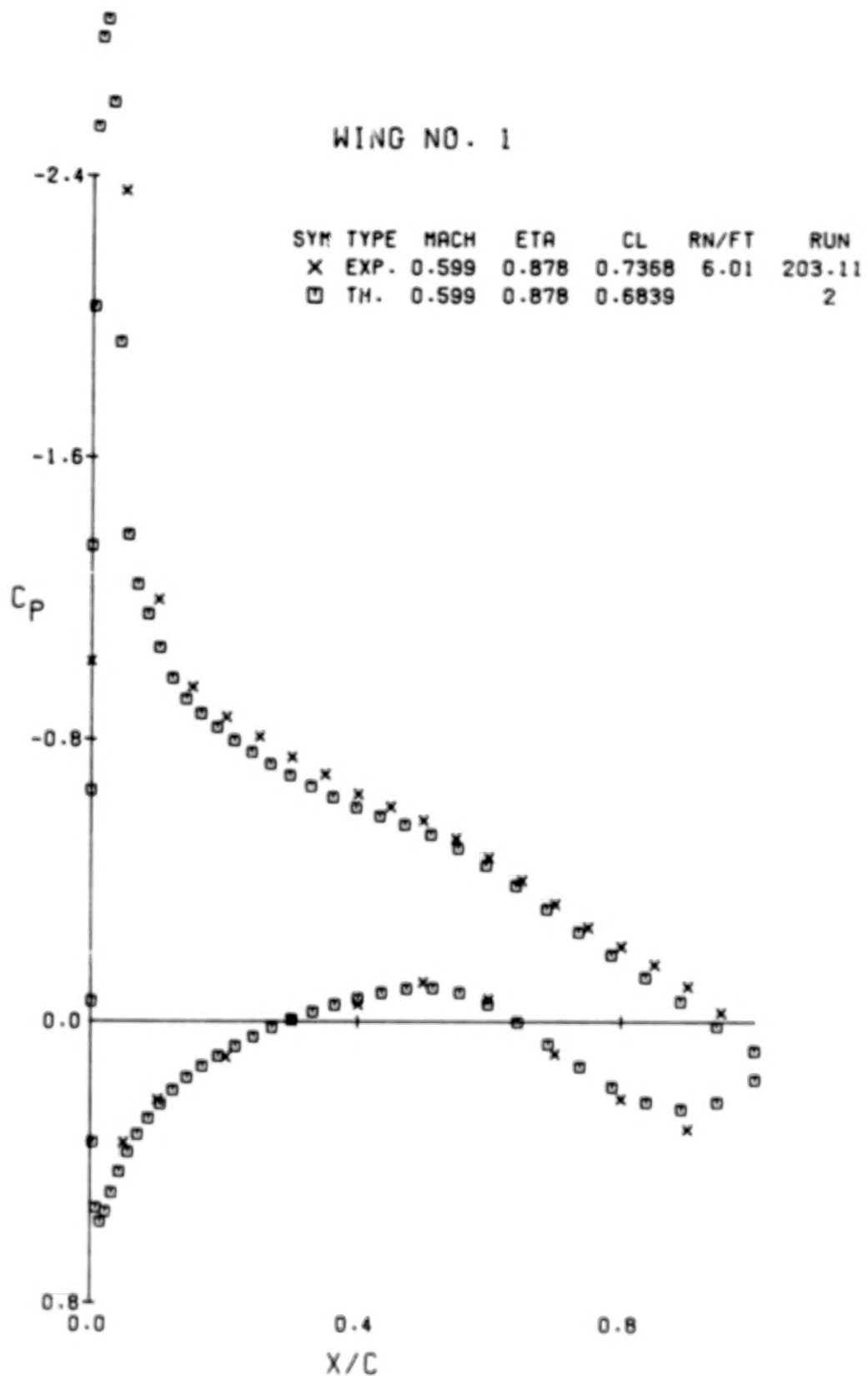
(B) ETA = .400

FIGURE 22.- WING NO. 1 COMPARISON OF THEORY WITH EXPERIMENT



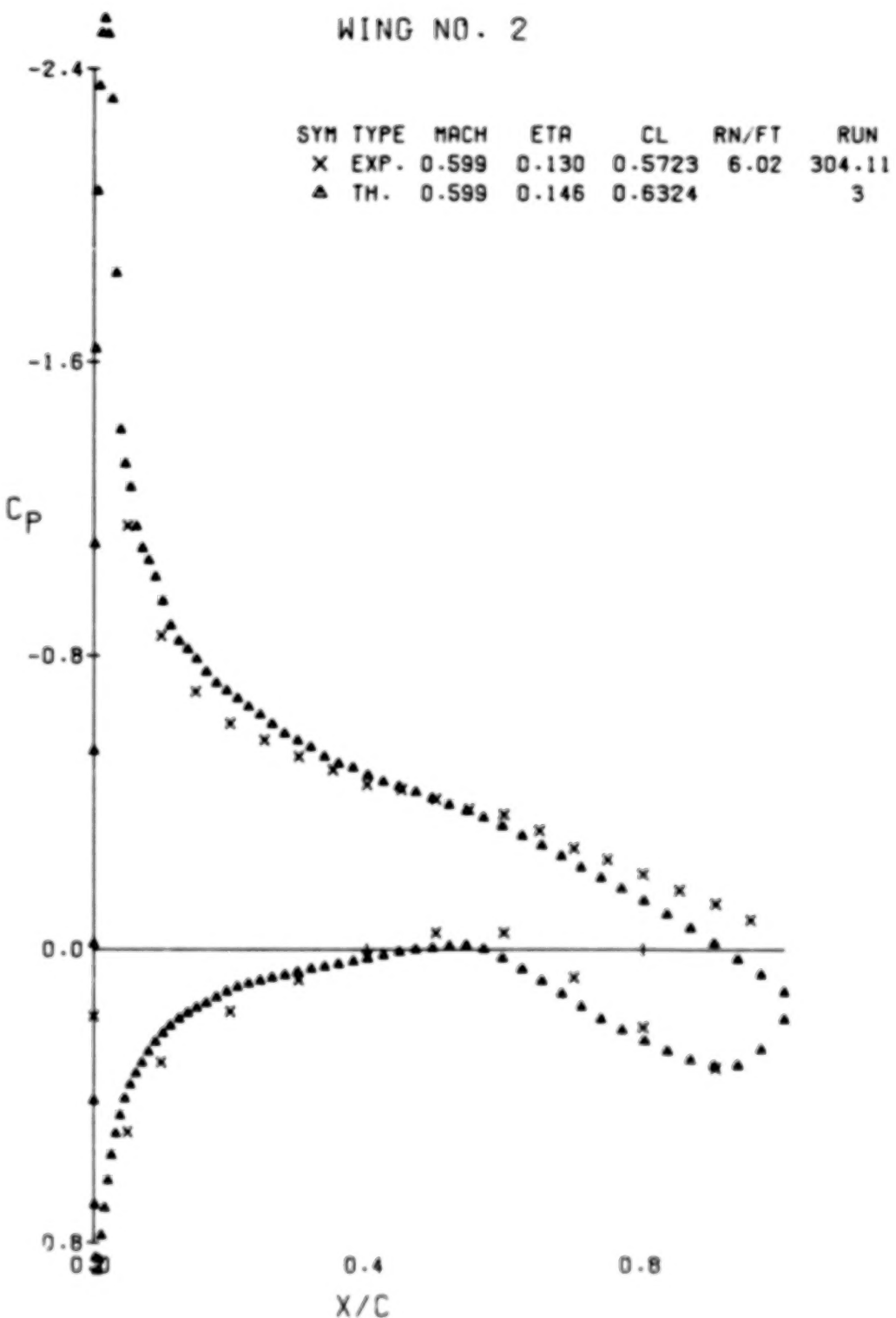
(C) ETA = .634

FIGURE 22.- WING NO. 1 COMPARISON OF THEORY WITH EXPERIMENT



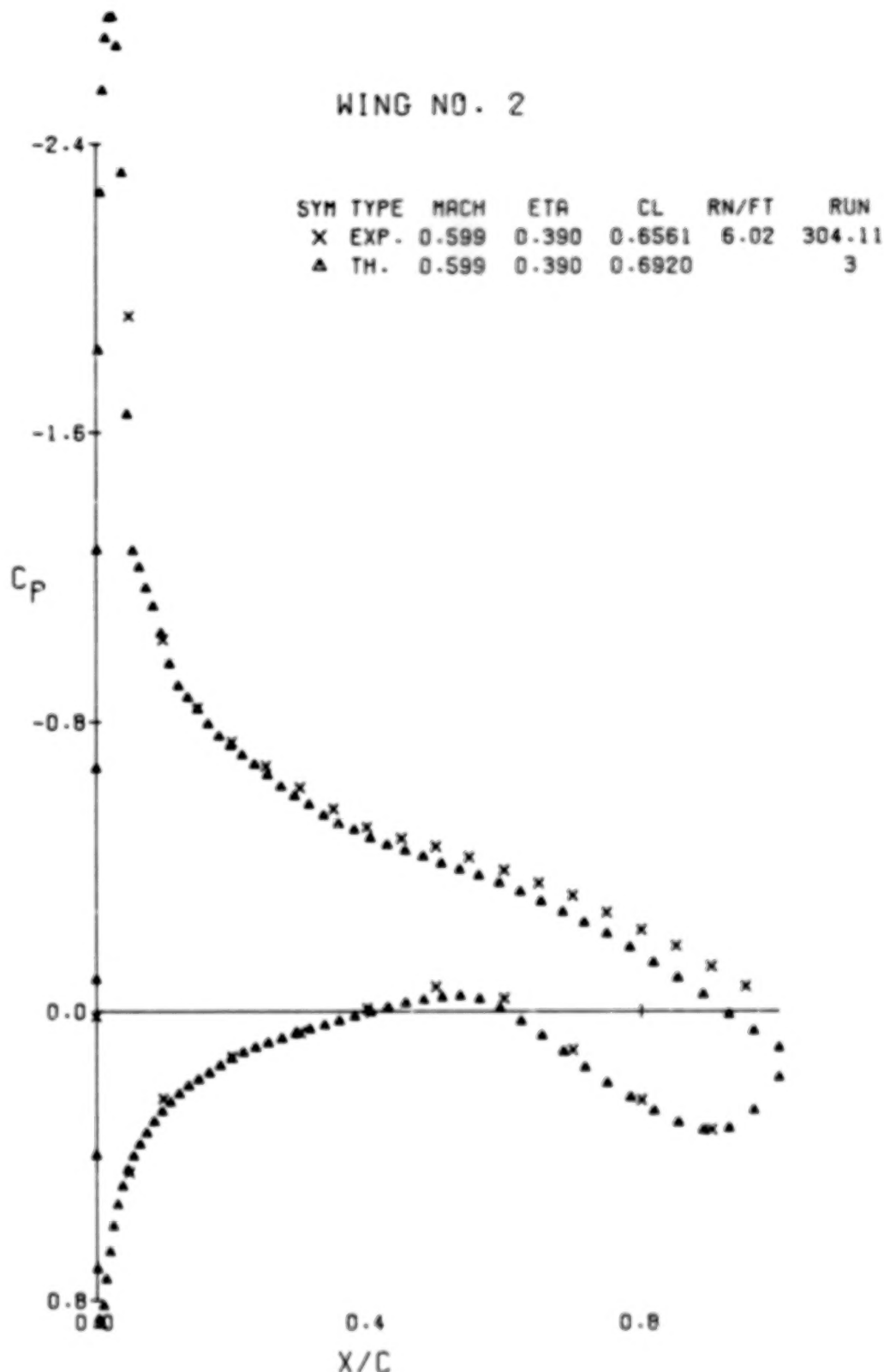
(D)  $\eta = .878$

FIGURE 22.- WING NO. 1 COMPARISON OF THEORY WITH EXPERIMENT



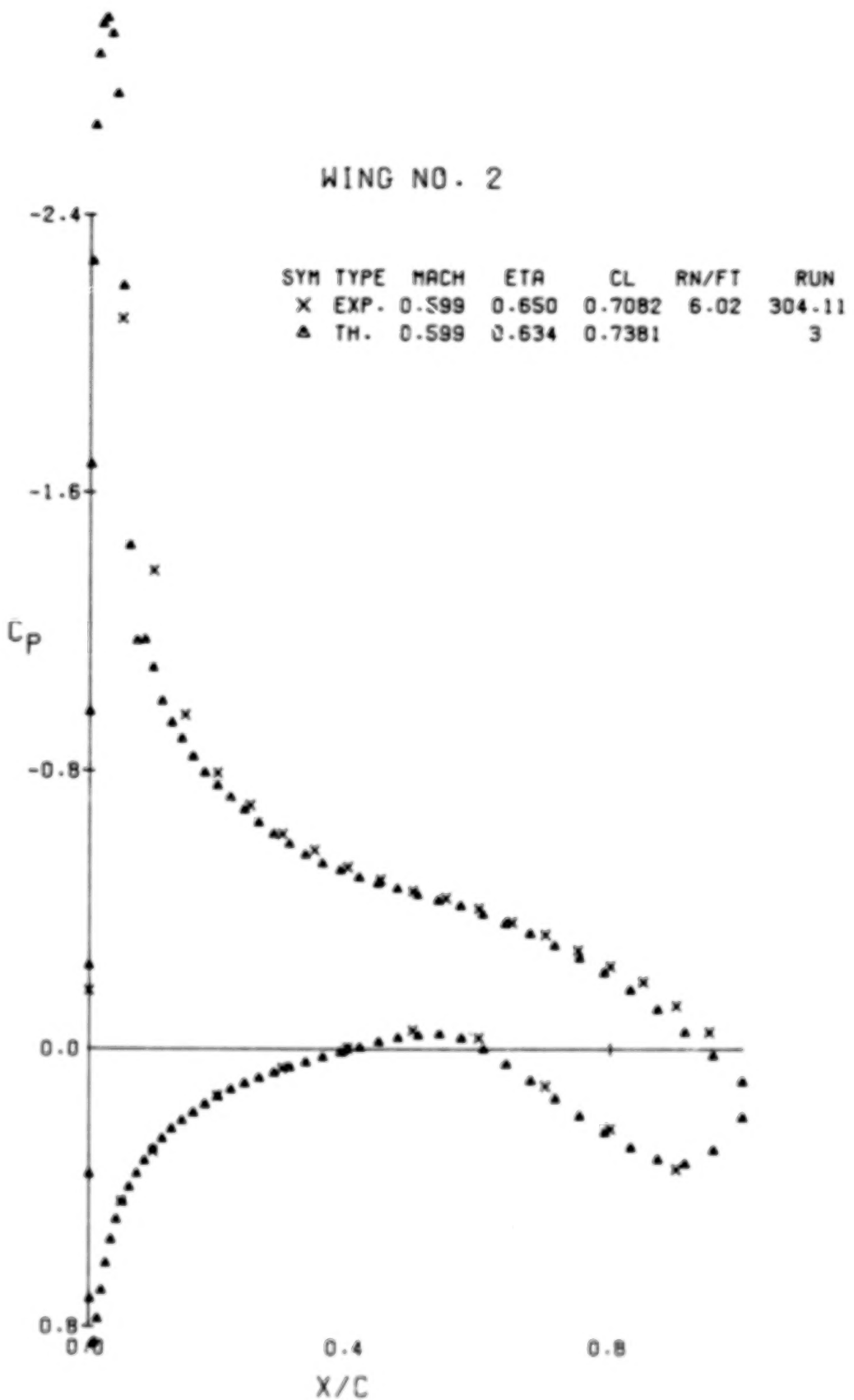
(A) ETA = .130

FIGURE 23.- WING NO. 2 COMPARISON OF THEORY WITH EXPERIMENT



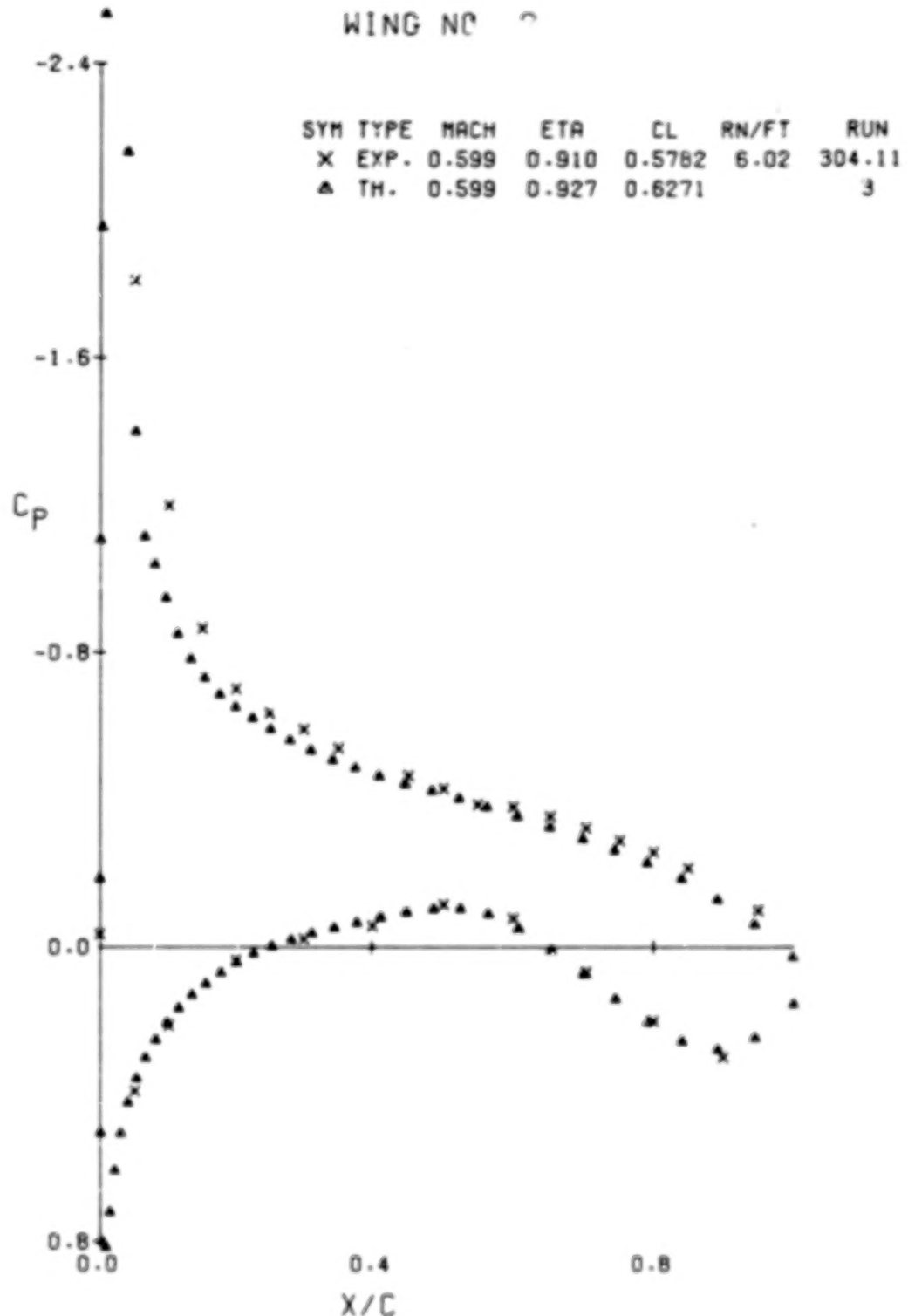
(B)  $\eta = .390$

FIGURE 23.- WING NO. 2 COMPARISON OF THEORY WITH EXPERIMENT



(C)  $\text{ETA} \approx .650$

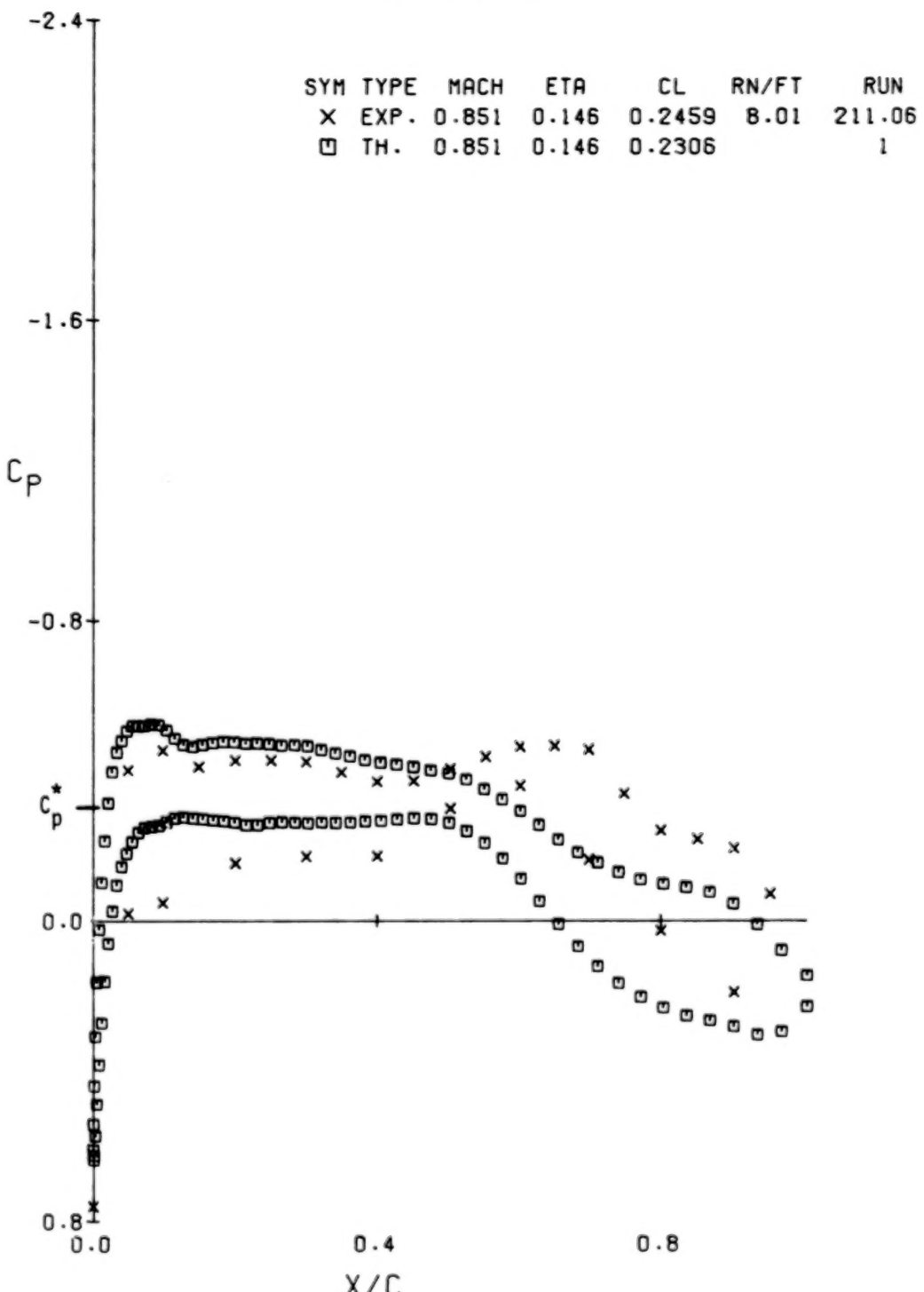
FIGURE 23.- WING NO. 2 COMPARISON OF THEORY WITH EXPERIMENT



(D) ETA = .910

FIGURE 23.- WING NO. 2 COMPARISON OF THEORY WITH EXPERIMENT

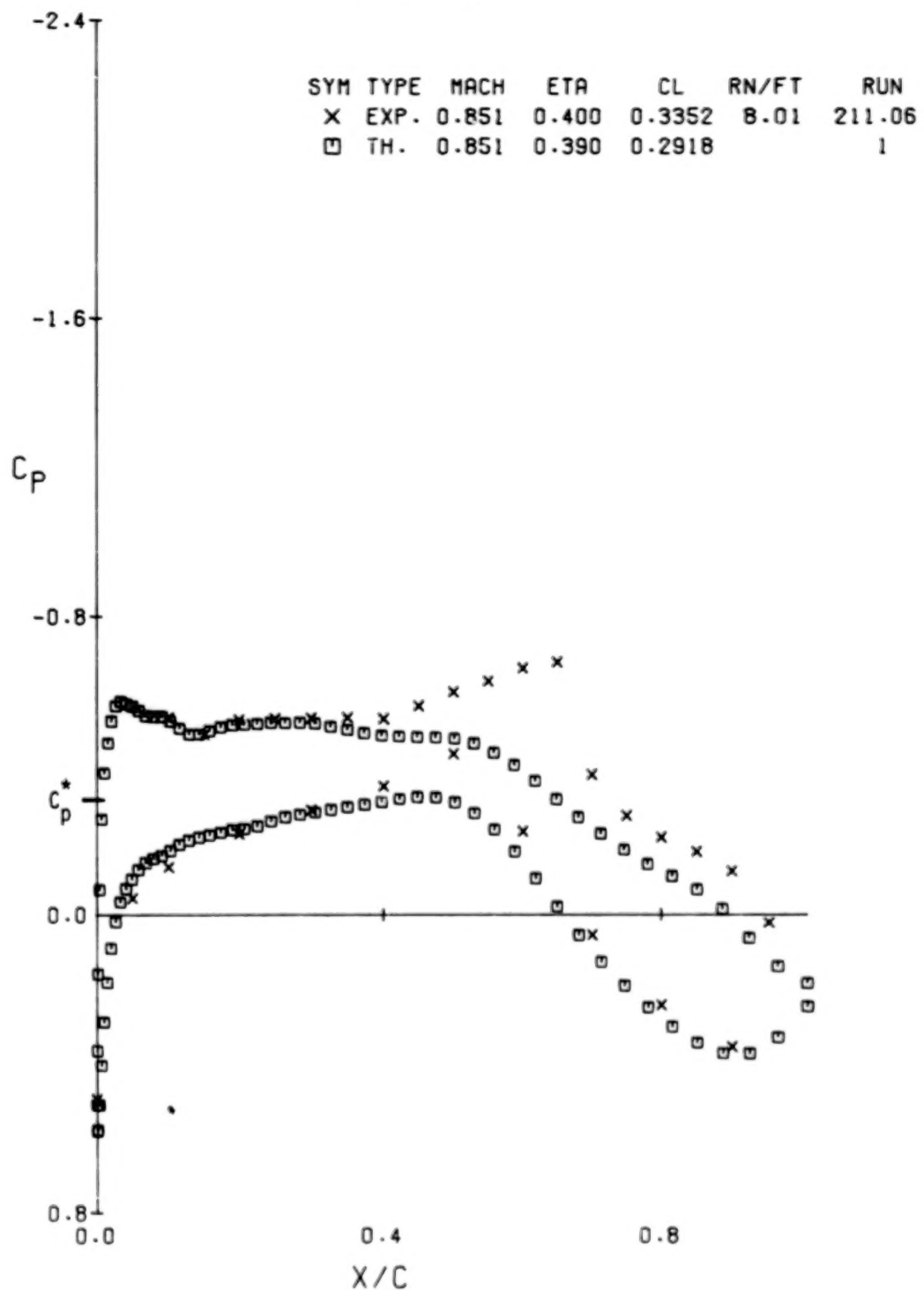
WING NO. 1



(A) ETA = .146

FIGURE 24.- WING NO. 1 COMPARISON OF THEORY WITH EXPERIMENT

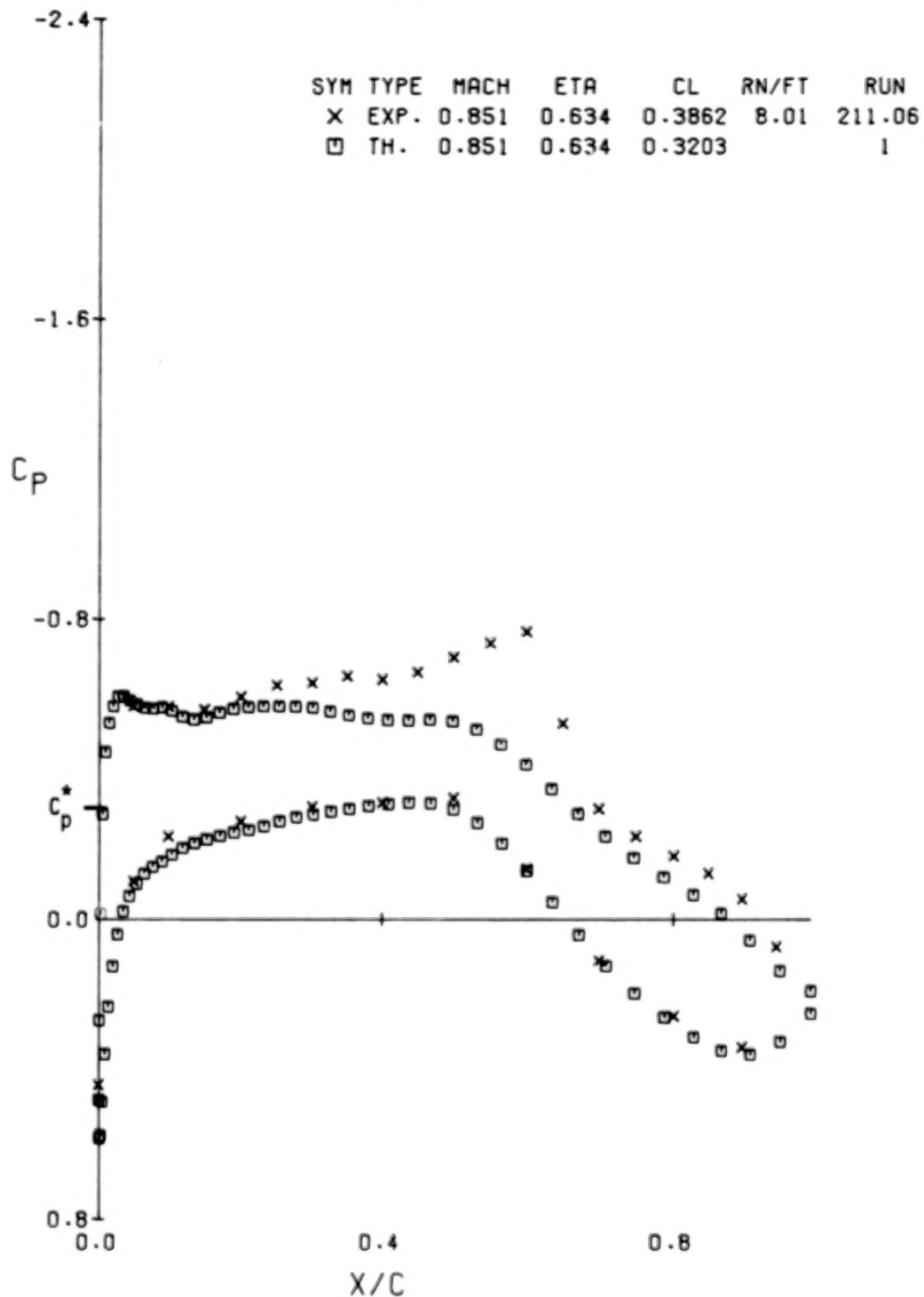
WING NO. 1



(B) ETA = .400

FIGURE 24.- WING NO. 1 COMPARISON OF THEORY WITH EXPERIMENT

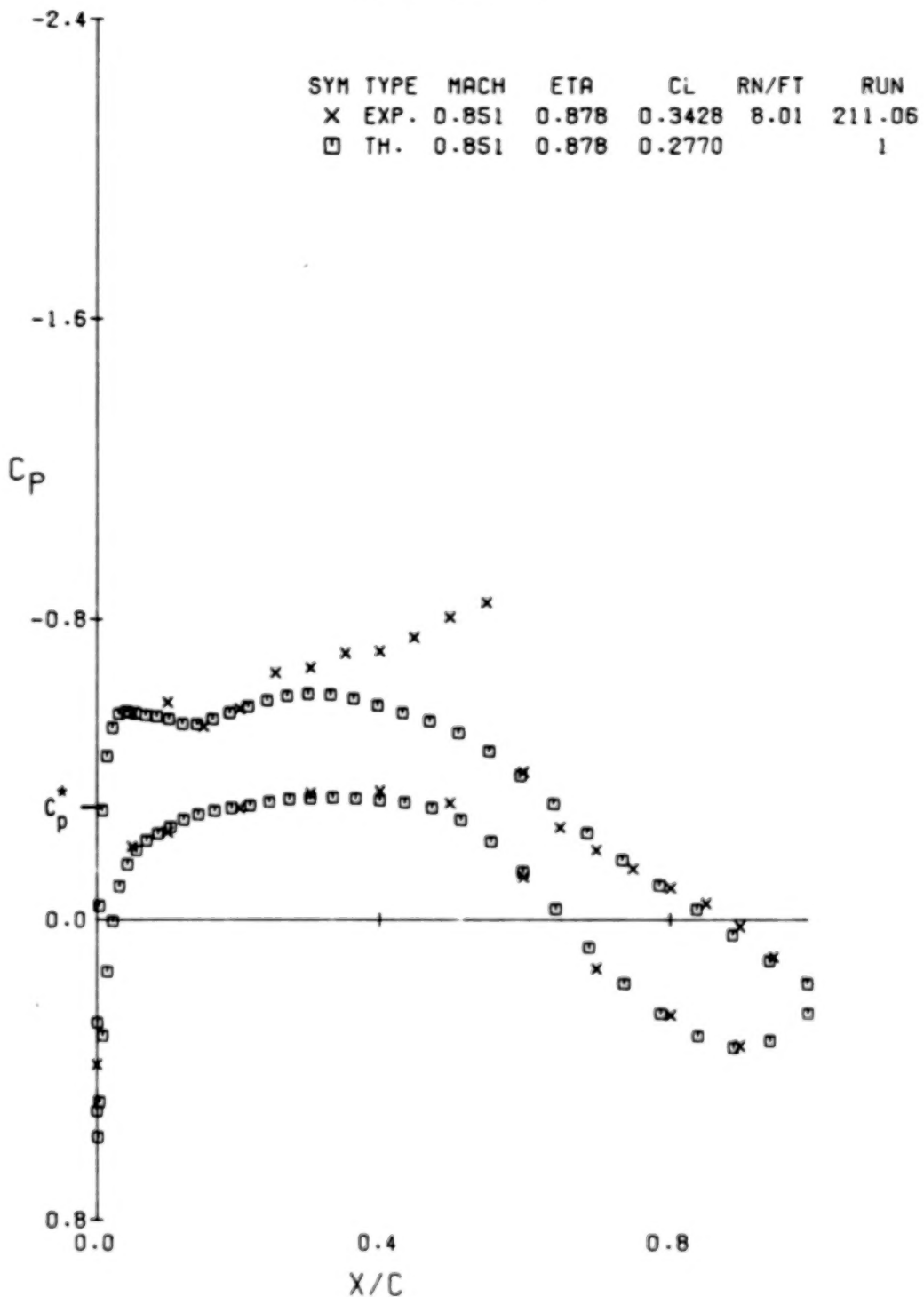
WING NO. 1



(C) ETA = .634

FIGURE 24.- WING NO. 1 COMPARISON OF THEORY WITH EXPERIMENT

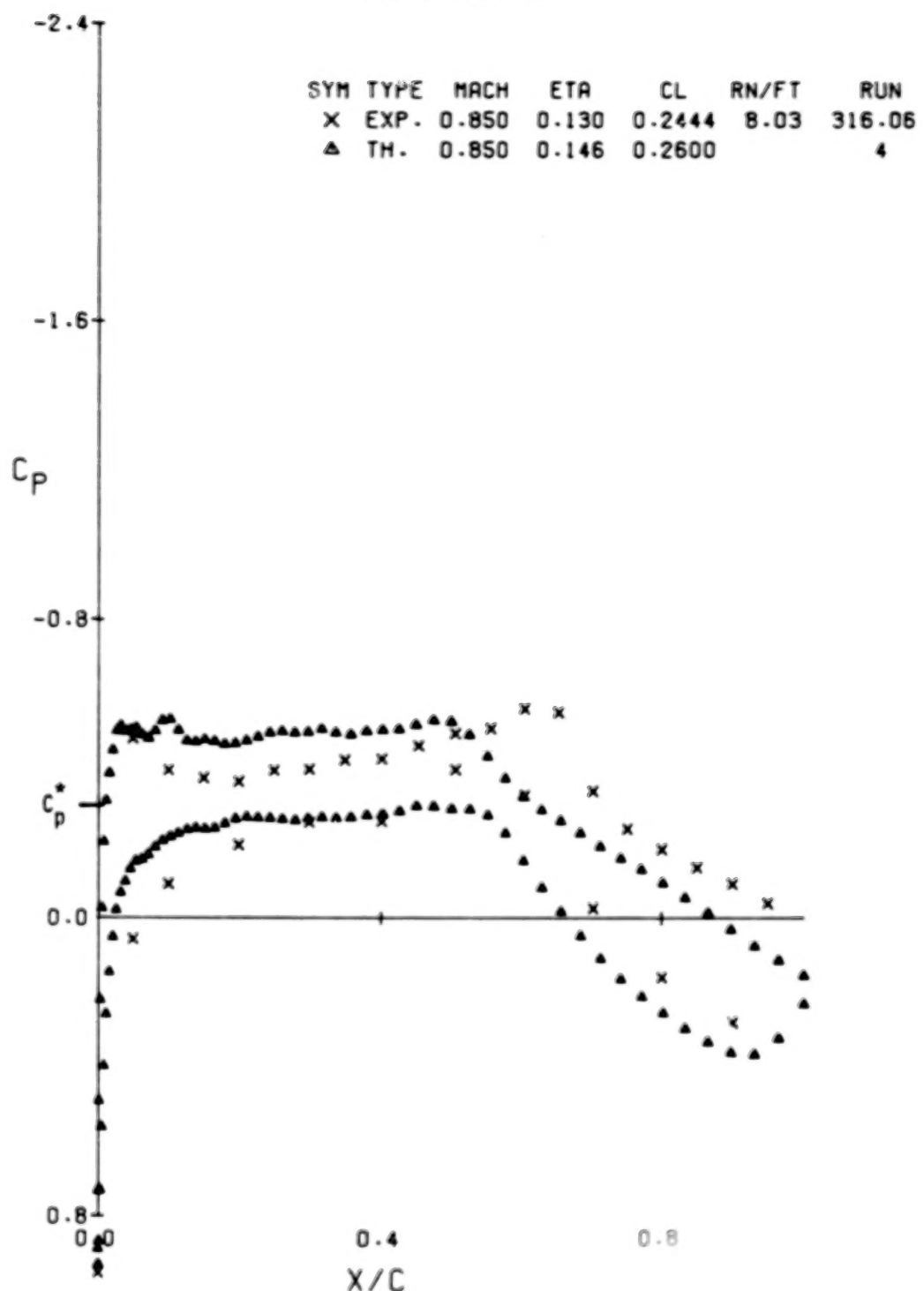
WING NO. 1



(D) ETA = .878

FIGURE 24.- WING NO. 1 COMPARISON OF THEORY WITH EXPERIMENT

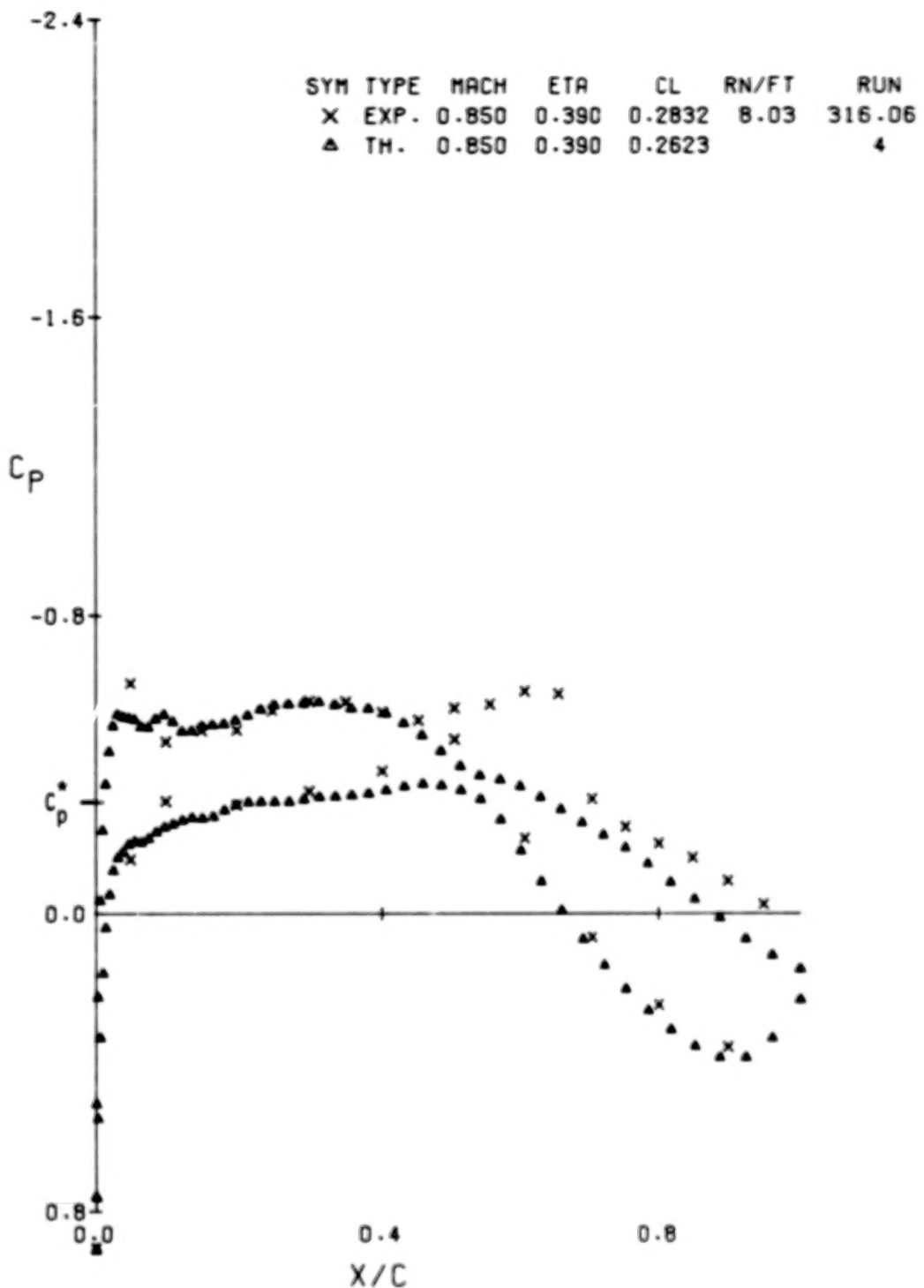
WING NO. 2



(A) ETA = .130

FIGURE 25.- WING NO. 2 COMPARISON OF THEORY WITH EXPERIMENT

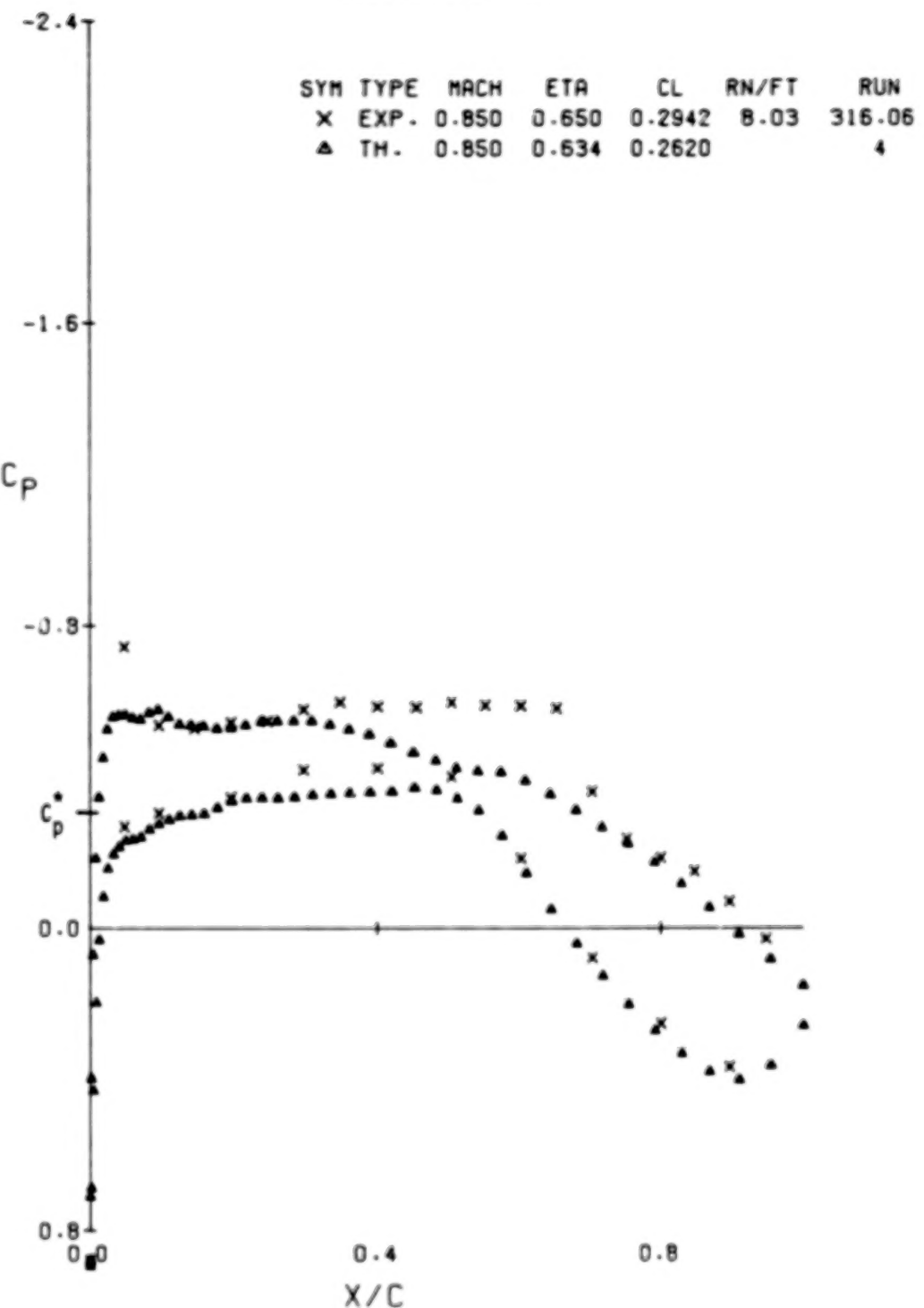
WING NO. 2



(B) ETA = .390

FIGURE 25.- WING NO. 2 COMPARISON OF THEORY WITH EXPERIMENT

WING NO. 2

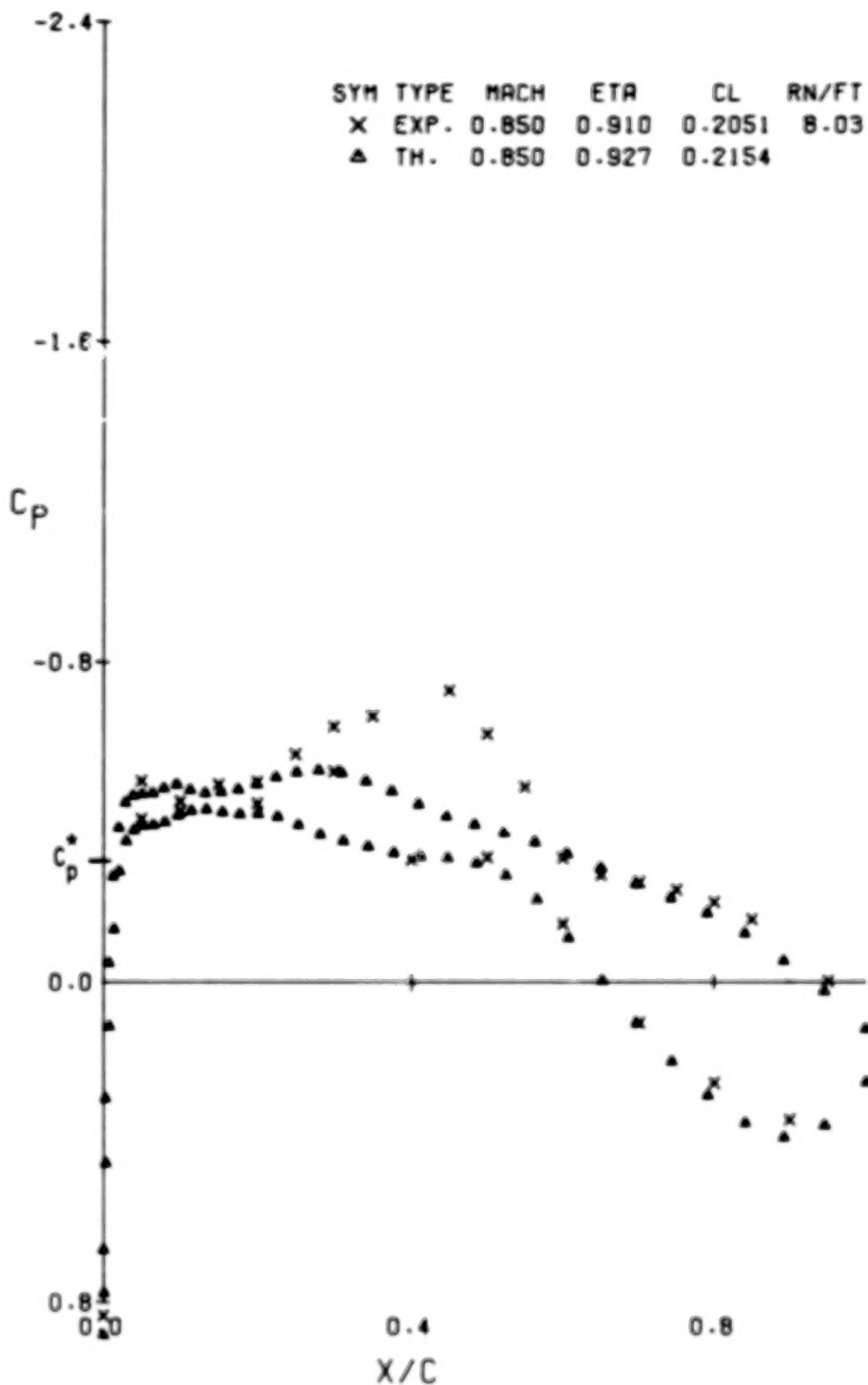


(C)  $\text{ETA} = .650$

FIGURE 25.- WING NO. 2 COMPARISON OF THEORY WITH EXPERIMENT

WING NO. 2

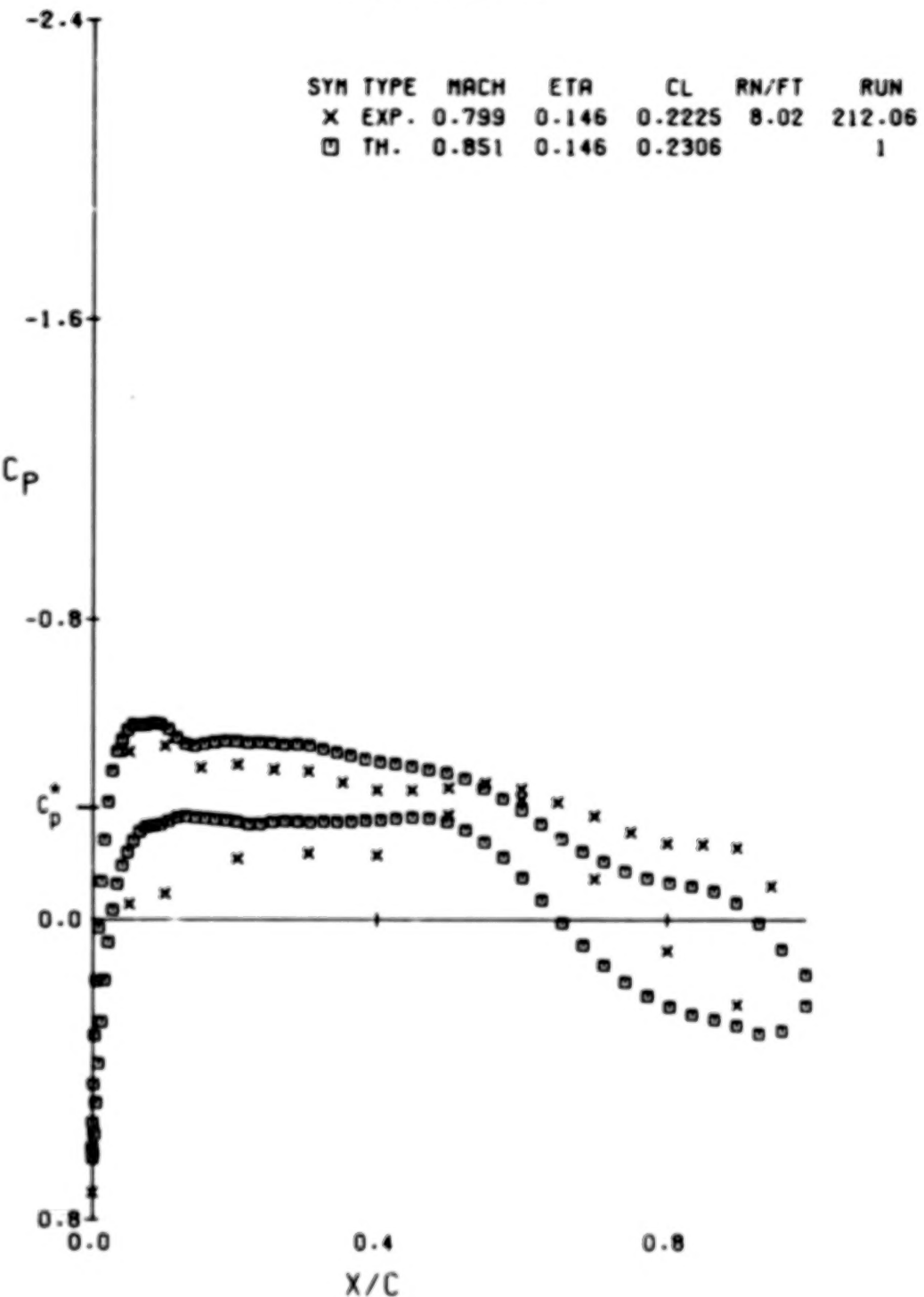
SYM	TYPE	MACH	ETA	CL	RN/FT	RUN
X	EXP.	0.850	0.910	0.2051	8.03	316.06
▲	TH.	0.850	0.927	0.2154		4



(D) ETA = .910

FIGURE 25.- WING NO. 2 COMPARISON OF THEORY WITH EXPERIMENT

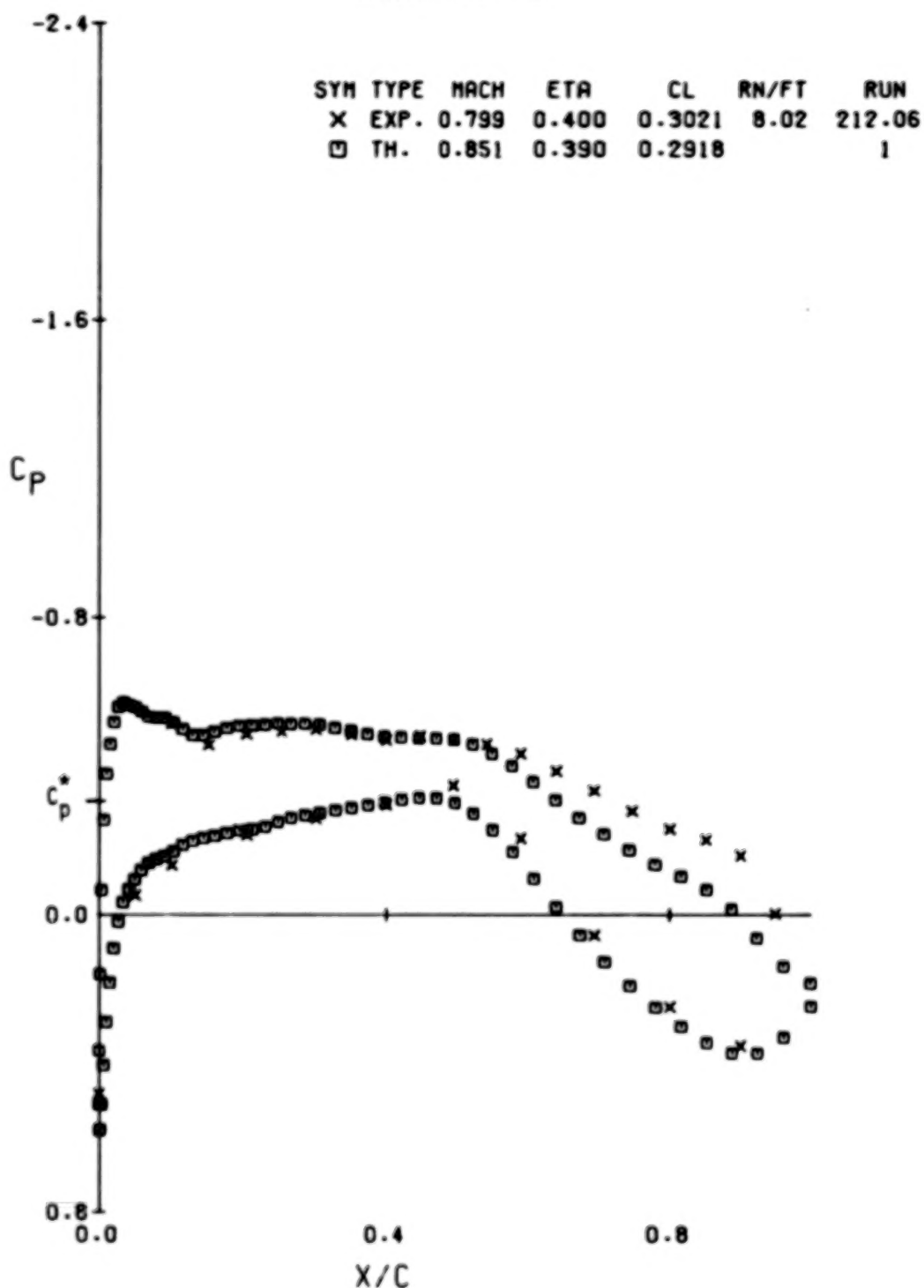
WING NO. 1



(A) ETA = .146

FIGURE 26.- WING NO. 1 COMPARISON OF THEORY WITH EXPERIMENT

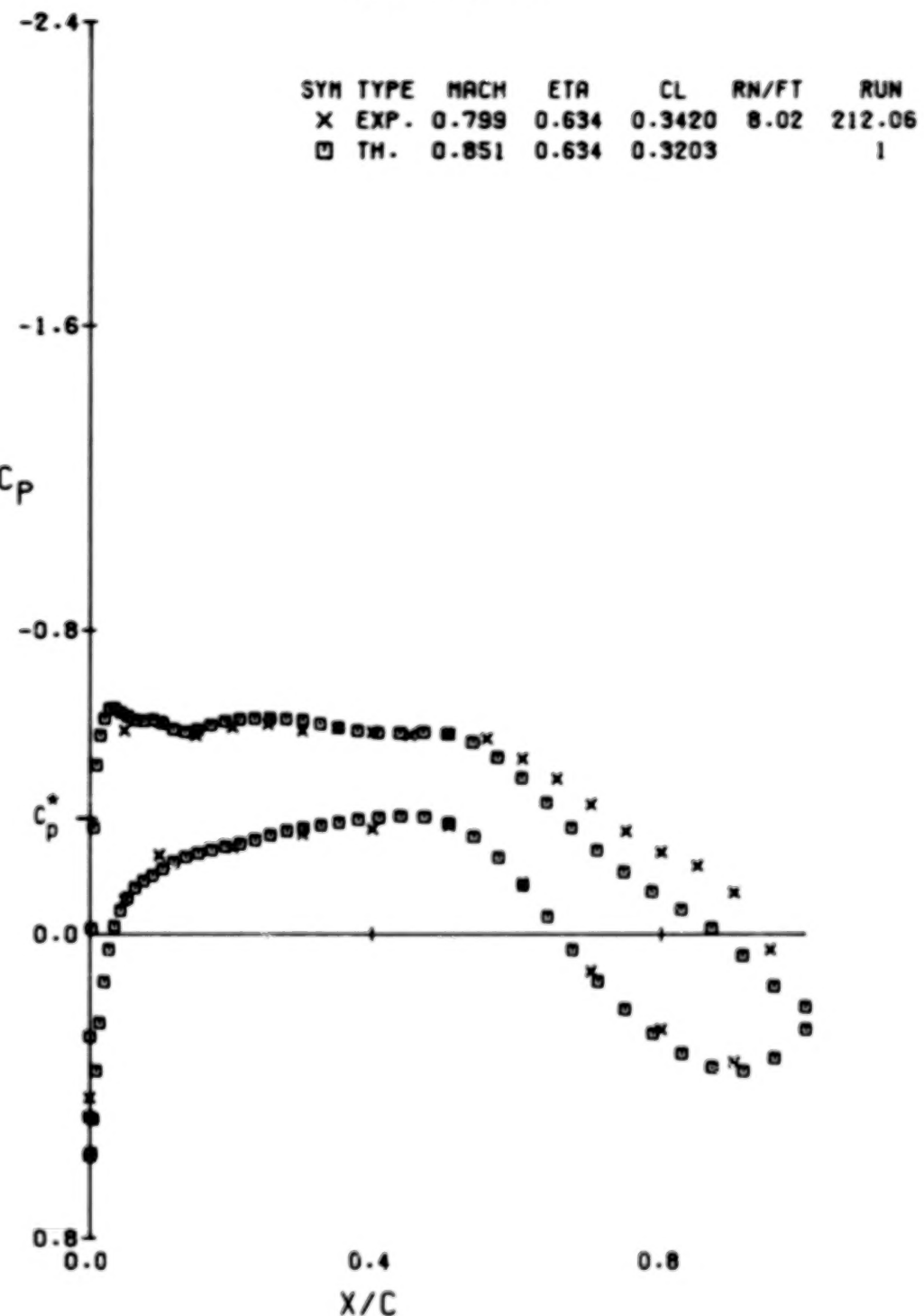
WING NO. 1



(B) ETA = .400

FIGURE 26.- WING NO. 1 COMPARISON OF THEORY WITH EXPERIMENT

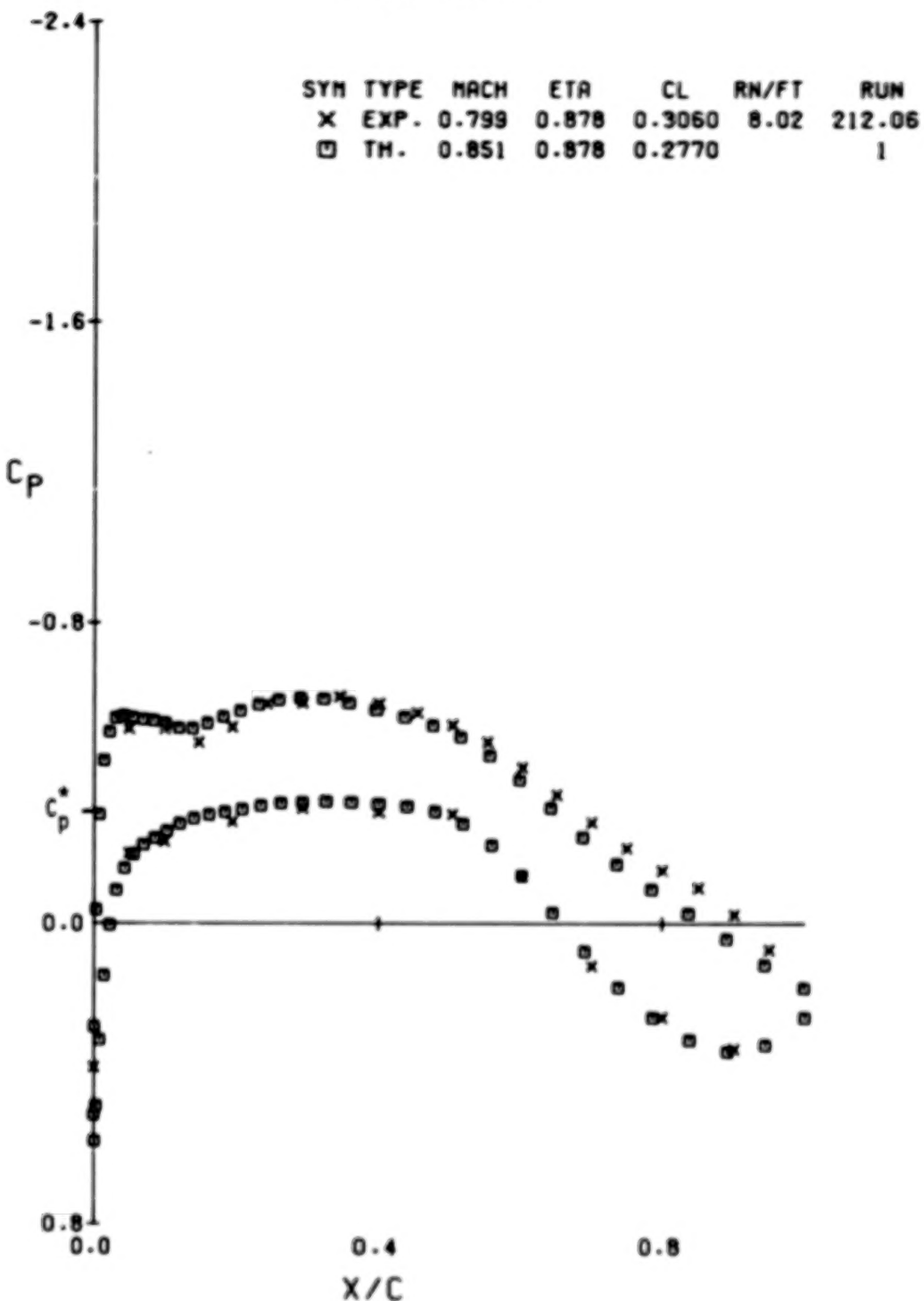
WING NO. 1



(C) ETA = .634

FIGURE 26.- WING NO. 1 COMPARISON OF THEORY WITH EXPERIMENT

WING NO. 1



(D) ETA = .878

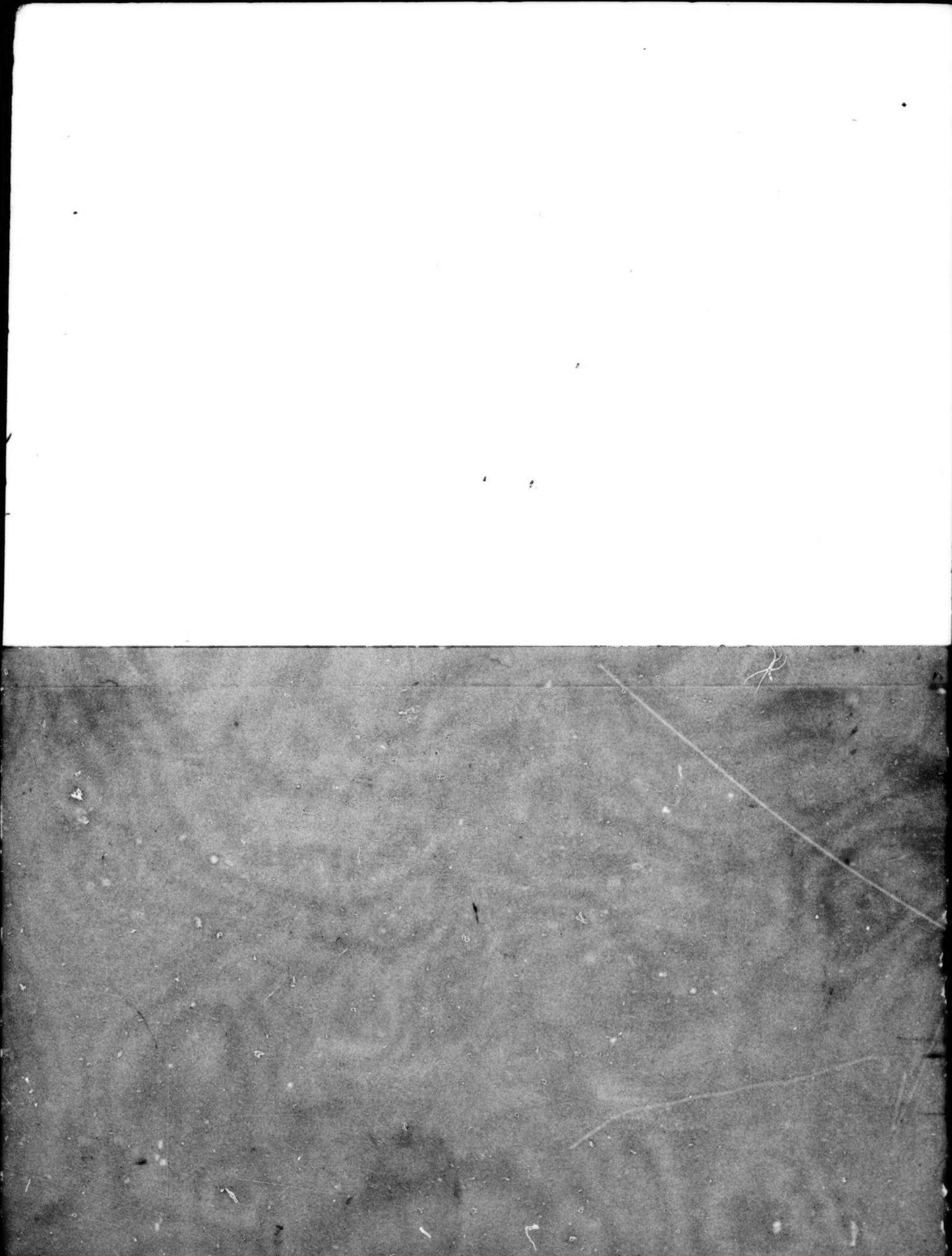
FIGURE 26.- WING NO. 1 COMPARISON OF THEORY WITH EXPERIMENT

1. Report No. NASA CR-3238	2. Government Accession No.	3. Recipient's Catalog No.	
4. Title and Subtitle <b>Application of Numerical Optimization to the Design of Wings with Specified Pressure Distributions</b>		5. Report Date <b>February 1980</b>	
7. Author(s) <b>H. P. Haney and R. R. Johnson</b>		6. Performing Organization Code	
9. Performing Organization Name and Address <b>Vought Corporation Dallas, Texas</b>		8. Performing Organization Report No.	
12. Sponsoring Agency Name and Address <b>National Aeronautics and Space Administration Washington, D. C. 20546</b>		10. Work Unit No.	
15. Supplementary Notes <b>Raymond M. Hicks NASA-Ames Research Center</b>		11. Contract or Grant No. <b>NAS2-9653</b>	
16. Abstract		13. Type of Report and Period Covered <b>Contractor Report</b>	
		14. Sponsoring Agency Code	
17. Key Words (Suggested by Author(s)) <b>Wing design Optimization Airfoil design</b>		18. Distribution Statement <b>Unlimited</b>  <b>Star Category - 02</b>	
19. Security Classif. (of this report) <b>Unclassified</b>	20. Security Classif. (of this page) <b>Unclassified</b>	21. No. of Pages <b>105</b>	22. Price* <b>6.50</b>

\*For sale by the National Technical Information Service, Springfield, Virginia 22161

NASA-Langley, 1980

106



**END**

**JUNE 23, 1981**